

# Transport of Galactic Cosmic Rays in Different Heliospheric Magnetic Field Configurations

Dissertation  
zur Erlangung des Doktorgrades  
der Mathematisch-Naturwissenschaftlichen Fakultät  
der Christian-Albrechts-Universität  
zu Kiel

vorgelegt von  
Oliver Sternal

Kiel  
2010

Referent: Prof. Dr. Bernd Heber

Korreferent: Priv.-Doz. Dr. habil. Horst Fichtner

Tag der mündlichen Prüfung: 01.07.2010

Zum Druck genehmigt: Kiel, 01.07.2010

Der Dekan

---

## Abstract

The propagation of energetic charged particles in the heliospheric magnetic field is one of the fundamental problems in heliophysics. It is described by Parker's transport equation, a differential equation to compute the temporal evolution of an isotropic particle distribution function under the influence of four basic physical processes: diffusion and drift in the heliospheric magnetic field, as well as convection and adiabatic energy changes in the solar wind. Especially the structure of the heliospheric magnetic field and its influence on the particle transport remain unsolved questions and are discussed controversially. The first successful analytic approach to the structure of the heliospheric magnetic field was the Parker field. Employing this theory, most magnetic field and particle measurements in the heliosphere could be explained. However, the measurements of the first out-of-ecliptic spacecraft Ulysses at high latitudes revealed that the existing magnetic field model as well as the diffusion theory, which was widely accepted up to that time, needed to be refined. Among other facts, this led to the development of a new and more complex heliospheric magnetic field model: the Fisk field. This new field model is highly debated and could not be confirmed with magnetic field measurements so far. A promising method to trace this magnetic field structure is the propagation of electrons in the energy range of a few MeV. The influence of a Fisk-type field on the particle transport in the heliosphere leads to characteristic variations of the electron intensities, which can be detected in Ulysses electron count rates.

This work presents 3D and time-dependent simulations of the propagation of energetic electrons for two models of the heliospheric magnetic field: the Parker field and for a Fisk-type field. In a study of the long-term modulation of 7 MeV electrons it is shown that the so-called compound approach for the diffusion in a Parker field can reproduce the electron count rates of the IMP-8, SOHO and Ulysses spacecraft for almost two solar cycles. Important parameters describing the solar cycle dependence of the diffusion coefficients are derived. The investigation of the electron transport in a Fisk-type field is devoted to variations of the computed electron intensities on the time scale of a solar rotation. It is shown that the Ulysses count rates of 2.5 – 7 MeV electrons reveal time variations caused by a Fisk-type structure of the heliospheric magnetic field. From a comparison of simulation results and the Ulysses count rates, realistic parameters for the Fisk theory are derived. Finally, the structure of the heliospheric magnetic field and its influence on the long-term modulation of energetic electrons are discussed for the newly found parameters.

---



---

## Zusammenfassung

Die Ausbreitung energiereicher geladener Teilchen im heliosphärischen Magnetfeld ist eines der fundamentalen Probleme in der Heliophysik. Ihre Beschreibung beruht auf der Parker-Transportgleichung, einer Differentialgleichung zur Berechnung der zeitlichen Entwicklung einer isotropen Verteilungsfunktion unter dem Einfluss von vier physikalischen Prozessen: Diffusion und Drift im heliosphärischen Magnetfeld, sowie Konvektion und adiabatischen Energieänderungen im Sonnenwind. Insbesondere die Struktur des heliosphärischen Magnetfeldes und dessen Einfluss auf die Ausbreitung geladener Teilchen stellen in der Heliophysik ein bisher nur unvollständig gelöstes und kontrovers diskutiertes Problem dar. Die erste erfolgreiche analytische Darstellung des heliosphärischen Magnetfeldes gelang mit dem sogenannten Parker-Feld, mit dessen Hilfe die Magnetfeld- und auch Teilchenmessungen in der Ekliptik erklärt werden konnten. Die ersten Messungen der Ulysses-Mission bei hohen heliographischen Breiten zeigten allerdings, dass sowohl das existierende Magnetfeldmodell als auch die bis dahin akzeptierte Theorie über diffusiven Teilchentransport überarbeitet werden mussten. Dies führte – zusammen mit weiteren neuen Messungen – zur Entwicklung eines neuen und komplexeren Modells für das heliosphärische Magnetfeld: das Fisk-Feld. Dieses wird in der Heliophysik allerdings kritisch diskutiert und konnte bisher mit Hilfe von Magnetfeldmessungen nicht nachgewiesen werden. Eine vielversprechende Nachweismethode ergibt sich in der Ausbreitung von Elektronen im Bereich einiger MeV. Der Einfluss einer Fisk-ähnlichen Magnetfeldstruktur auf den Teilchentransport in der Heliosphäre führt zu charakteristischen Schwankungen der Elektronenintensitäten, die in den Zählraten der Ulysses-Mission nachgewiesen werden können.

Die vorliegende Arbeit widmet sich der Modellierung der Ausbreitung energiereicher Elektronen in einer dreidimensionalen und zeitabhängigen Simulation für zwei Modelle des heliosphärischen Magnetfeldes: dem Parker-Feld und dem Fisk-Feld. In einer Studie über die Langzeit-Modulation von 7 MeV-Elektronen wird gezeigt, dass mit Hilfe des sogenannten Compound-Ansatzes für die Diffusion im Parker-Feld die Elektronenzählraten der Raumsonden IMP-8, SOHO und Ulysses über einen Zeitraum von fast zwei solaren Zyklen erklärt werden können. Dabei werden wichtige Parameter für die zeitliche Abhängigkeit der Diffusionsparameter vom solaren Zyklus abgeleitet. Die Untersuchung der Elektronenausbreitung im Fisk-Feld beschäftigt sich mit Variationen der berechneten Elektronenintensitäten auf der Zeitskala einer Sonnenrotation. Es wird gezeigt, dass die von Ulysses gemessenen Elektronenzählraten im Bereich von 2.5 – 7 MeV Variationen beinhalten, die von einer Fisk-Struktur des heliosphärischen Magnetfeldes erzeugt werden. Aus einem Vergleich von Simulationsergebnissen und Messungen der Ulysses-Raumsonde werden realistische Parameter für die Fisk-Theorie abgeleitet. Abschließend werden die Struktur des heliosphärischen Magnetfeldes und dessen Einfluss auf die Langzeit-Modulation von energiereichen Elektronen mit den neu gewonnenen Parametern untersucht.

---

# Contents

<b>1</b>	<b>Introduction</b>	<b>1</b>
<b>2</b>	<b>The Sun and the Heliosphere</b>	<b>5</b>
	The Solar Cycle . . . . .	5
	The Solar Wind . . . . .	8
	The Heliospheric Boundary . . . . .	11
<b>3</b>	<b>The Heliospheric Magnetic Field</b>	<b>13</b>
	The Parker Model of the Heliospheric Magnetic Field . . . . .	14
	The Heliospheric Current Sheet . . . . .	17
	The Fisk Model of the Heliospheric Magnetic Field . . . . .	20
	The Fisk-Parker Hybrid Approach . . . . .	26
<b>4</b>	<b>The Propagation of Energetic Particles</b>	<b>33</b>
	The Jovian Magnetosphere as an Electron Source in the inner Heliosphere . . . . .	35
	Parker’s Transport Equation . . . . .	38
	Convection with the Solar Wind . . . . .	39
	Adiabatic Energy Changes . . . . .	41
	Particle Diffusion and Drift . . . . .	42
	A Comparison of the Diffusion Tensor in different HMF Configurations . . . . .	48
<b>5</b>	<b>Setting up a Model for Particle Propagation</b>	<b>53</b>
	The TPE in Spherical Polar Coordinates . . . . .	53
	Setting up a Propagation Model with VLUGR3 . . . . .	55
<b>6</b>	<b>Investigating the Electron Flux in a Parker HMF</b>	<b>59</b>
	Spacecraft Measurements . . . . .	59
	Model Results for the Electron Flux . . . . .	62
	Varying the Solar Cycle Parameters . . . . .	75
	Conclusions . . . . .	82

<b>7</b>	<b>A theoretical Study of the Electron Propagation in a Fisk-type HMF</b>	<b>85</b>
	The Electron Flux in a Schwadron-Parker HMF . . . . .	85
	Ulysses Electron Measurements at high Latitudes . . . . .	89
	Implications of Ulysses Electron Measurements on the Fisk Theory . . . . .	96
	Consequences for the HMF Structure and the Transport of Energetic Particles	102
	Conclusions . . . . .	109
<b>8</b>	<b>Summary and Conclusions</b>	<b>111</b>
	The Electron Flux in a Parker HMF . . . . .	111
	7 MeV Electron Intensities in a Fisk-type HMF . . . . .	112
<b>9</b>	<b>Future Prospects</b>	<b>115</b>
	Long-term Modulation of Energetic Electrons in a Parker Field . . . . .	115
	The 7 MeV Electron Flux in a Fisk-type HMF . . . . .	116

# Chapter 1

## Introduction

The Sun is the host star of our planetary system. It is of central interest in many domains of human life, e.g. religion, art or economy. The Sun is also a focus of scientific work; one specific issue is the understanding of its influence on the Earth and nearby space. The solar wind – a steady plasma stream flowing radially away from the Sun – originating in the solar corona creates a three-dimensional structure surrounding the Sun due to interaction with the local interstellar medium. This bubble with a diameter of 200 – 300 AU is known as the heliosphere (Zank, 1999; Borrmann and Fichtner, 2005). From a distance beyond 10 – 15 solar radii the solar magnetic field is frozen into the solar wind and a global magnetic field structure evolves: the heliospheric magnetic field. The first successful theoretical model describing the structure of the heliospheric magnetic field was proposed by Parker (1958), suggesting the field lines to be structured as Archimedean spirals.

The heliosphere and its global magnetic field act as a shield against energetic charged particles constantly entering the heliosphere from the local interstellar medium (see Fig. 1.1). These so-called cosmic rays enter the heliosphere, where their energy spectrum is highly modulated depending on the solar activity cycle, until they finally reach the Earth. Their influence on the Earth is debated controversially today (see e.g. Scherer et al., 2007; Erlykin et al., 2009, and references therein).

Not only for that reason, the transport of energetic charged particles through the heliosphere is one of the fundamental processes investigated in heliophysics. A very successful approach to this problem was suggested by Parker (1965) deriving a transport equation describing the time evolution of an isotropic particle distribution function under the influence of four basic physical mechanisms: diffusion and drift in the heliospheric magnetic field, convection with the solar wind and adiabatic energy changes in the solar wind. The diffusion of energetic charged particles is described as a stochastic motion along and perpendicular to the magnetic field lines due to scattering in the turbulent heliospheric magnetic field. This process has been addressed by many researchers (see e.g. Jokipii, 1966; Schlickeiser, 2002; Shalchi, 2009, and references therein) and is still not solved yet.

The description of the diffusive particle transport applying Parker’s transport equa-

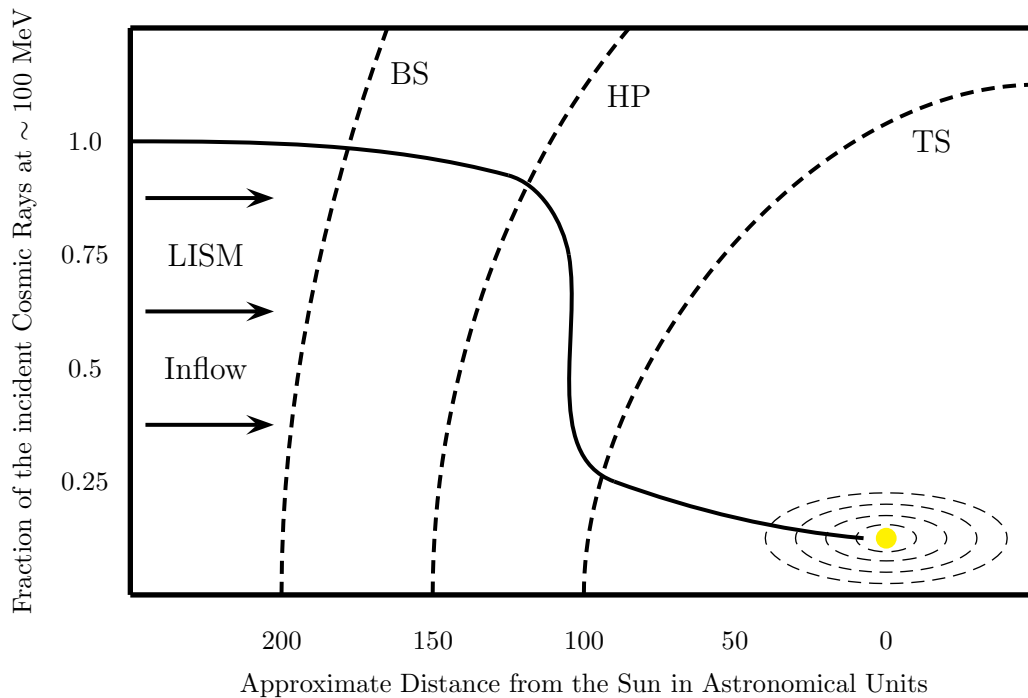


Figure 1.1: “Cosmic ray shielding”. The Sun is located in the “center” of the heliosphere. The heliospheric boundary consisting of a solar wind termination shock (TS), the bow shock (BS) and the heliopause (HP). The latter separates the solar wind plasma from the local interstellar medium (LISM). The solid black line represents the fraction of the cosmic ray flux entering the heliosphere from the LISM. Inside the heliosphere the cosmic rays are modulated and at  $\sim 100$  MeV only  $\sim 25\%$  of the incident particles can reach the Earth’s orbit. (Adopted from Adler *Planetarium, Chicago, 2010*)

tion is today accepted to be correct. The main problems in solving this differential equation are large uncertainties in the parameters: The measurements of the first out-of-ecliptic spacecraft Ulysses revealed that the particle count rates at high heliographic latitudes could not be reproduced using the standard diffusion parameters (Ferrando, 1999). It was shown that the diffusion in polar direction is considerably higher in the fast solar wind, which originates in the polar coronal holes during solar minimum conditions, than assumed so far. Among other facts, this led to the suggestion of a different and more complex model of the heliospheric magnetic field (Fisk, 1996). This new approach proposed magnetic field lines connecting the equatorial regions of the heliosphere with the polar regions, allowing energetic charged particles to travel more easily in polar direction along magnetic field lines. However, the existence of such a Fisk-type heliospheric magnetic field structure is discussed controversially (Roberts et al., 2007; Burger et al., 2008) and could not be confirmed by magnetic field measurements so far (Forsyth et al., 2002; Roberts et al., 2007). Its implementation in

---

numerical models simulating particle transport in the heliospheric magnetic field by solving Parker’s transport equation is very complex and was up to now only performed in steady state models (Burger and Hitge, 2004; Krüger, 2005; Burger et al., 2008). Another difficulty is to search for signatures in the particle flux which can be attributed to the existence of a Fisk-like heliospheric magnetic field unambiguously. A promising possibility is the investigation of electrons at energies of a few MeV, where two dominant particle sources are known: galactic electrons enter the heliosphere from the interstellar medium continuously, and the Jovian magnetosphere presents a second electron source. Jovian electrons are of special interest because of Jupiter’s non-central position with respect to the Sun and, thus, the symmetry axis of the heliospheric magnetic field leads to the unique opportunity to study the electron propagation in this field.

This work presents time-dependent numerical simulations of the electron flux in the heliosphere in two different models for the heliospheric magnetic field: the Parker field and, for the first time, also for a Fisk-type field. The computed electron intensities are compared to the corresponding count rates of three different space missions: IMP-8 (Interplanetary Monitoring Platform) and SOHO (Solar and Heliospheric Observatory) at the Earth’s orbit and Ulysses with its trajectory almost perpendicular to the ecliptic. The simulations in this investigations are performed to answer the following questions:

- What is the influence of a Fisk-type heliospheric magnetic field structure on the 7 MeV electron flux in the heliosphere on the time scale of a solar rotation?
- Can the electron intensities in the inner heliosphere be employed to trace a Fisk-type heliospheric magnetic field structure in particle measurements?
- Is there a possibility of deriving realistic parameters for the Fisk theory from a comparison of electron simulation data to corresponding Ulysses measurements?
- What is the influence of such a heliospheric magnetic field on the long-term modulation of energetic charged particles during the solar cycle?

Before applying the transport model to electron propagation in a Fisk-type field, the model setup is tested for validity with a Parker heliospheric magnetic field. Ferreira et al. (2003b) suggested a diffusion model for the modulation of energetic charged particles in a Parker field over the solar cycle and showed their theory to be applicable for high energy electrons, protons and helium in a steady state model. For the validation of the time-dependent transport model employed in this work, an additional so far unanswered question is addressed:

- Can the 7 MeV electron count rates of the three spacecraft IMP-8, SOHO and Ulysses be reproduced applying the Ferreira diffusion model to a time-dependent simulation?

The approach to achieve these goals is presented in the following. First, the theoretical background is explained. Therefore, chapter 2 is devoted to the Sun, the solar wind and the structure of the heliosphere. The most relevant models of the heliospheric magnetic field are described in chapter 3. The Parker field (Parker, 1958) as well as the Fisk field and its refinements (Fisk, 1996; Schwadron and McComas, 2003; Burger and Hitge, 2004; Hitge and Burger, 2010) are discussed with their advantages and drawbacks. Parker's transport equation (Parker, 1965) and the physical processes influencing the propagation of energetic charged particles are presented in chapter 4 with a particular focus on particle diffusion in different heliospheric magnetic field configurations. Chapter 5 presents the setup of the numerical scheme (Blom and Verwer, 1994, 1996) used to compute electron intensities in the heliosphere in a time-dependent simulation by solving the transport equation. The results of this investigation are shown in chapters 6 and 7. While chapter 6 presents a study of the long-term modulation of 7 MeV electrons, chapter 7 is devoted to modeling the 7 MeV electron flux in a Fisk-type heliospheric magnetic field. Electron intensities in the heliosphere are computed and compared to spacecraft measurements. The main results of this work are summarised in chapter 8, while chapter 9 points out the open questions arising from the achievements presented in this work.



# Chapter 2

## The Sun and the Heliosphere

The space between the stars is not empty, but it is filled with charged and neutral particles, molecules and dust – the interstellar medium (ISM). The Sun itself affects its environment by the solar wind (SW), its magnetic field and electromagnetic radiation varying with the solar activity cycle. The interstellar matter in the Sun’s vicinity is pushed away resulting in a bubble in the local interstellar medium (LISM) with a diameter of 200–300 AU (1 astronomical unit = 1 AU =  $1.49 \cdot 10^{11}$  m = the distance Sun – Earth) surrounding the Sun – the heliosphere. Its structure depends strongly on the properties of the SW varying with the solar cycle, the LISM and the relative velocity of the Sun and the LISM.

In this chapter the heliospheric structure and the fundamental phenomena involved in its establishing are summarised. The solar activity cycle, the solar wind and the heliospheric boundary are described.

### The Solar Cycle

The invention of the telescope 400 years ago encouraged the exploration of the Sun. Galileo Galilei and others started the examination of the dark spots on the solar surface in the early 17<sup>th</sup> century. Christoph Scheiner, Galileo Galilei and Johannes Fabricius independently discovered these so-called sunspots in 1611. Johannes Fabricius observed the sunspot pattern evolving on short time scales from which he derived the solar rotation. Figure 2.1 shows four of Galilei’s sunspot drawings from 1613 (Van Helden, 1995). Although the pictures are very similar, the evolution of the sunspot pattern with time is visible.

In 1851 Heinrich Schwabe discovered that the sunspot number follows a long term periodicity. The sunspot number varies with a quasi-periodicity of  $\sim 10$ –13 years. This so-called solar cycle is illustrated in Fig. 2.2, which shows the sunspot numbers from 1950 – 2008. The number of sunspots observed on the solar surface is an indicator for the solar activity. The conditions of the solar corona during periods of sunspot minima differ considerably from those during sunspot maxima, as described below.

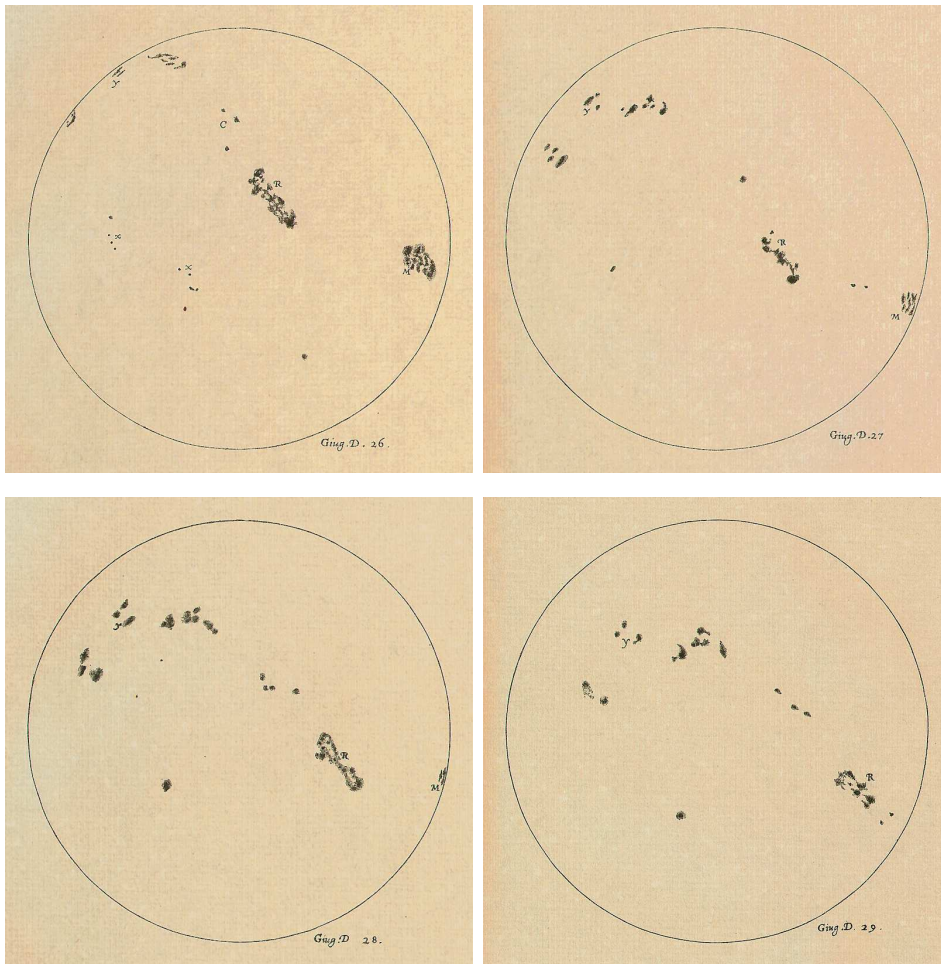


*Figure 2.1: Four of Galilei's sunspot drawings, June 26 – 29, 1613 (from upper left to lower right). Although the pictures are very similar, the evolution of the sunspot pattern with time is visible. (Taken from Van Helden, 1995)*

Hale (1908) discovered strong magnetic fields inside of sunspots with sunspot pairs having opposite polarities in opposite hemispheres of the Sun. His observations revealed that the polarity of the sunspot pairs reverses every  $\sim 11$  years, leading to the conclusion that the solar magnetic field polarity changes periodically with a period of  $\sim 22$  years – the Hale cycle.

Today it is known that the Sun is a magnetic star. This magnetic field is commonly believed to be built up by a solar dynamo being described by turbulent dynamo theory as the result of the differential rotation of the Sun and the plasma motion inside the convection zone. Reviews on the solar dynamo theory can be found in e.g. Choudhuri (2000, 2008), Charbonneau (2005), Dikpati and Gilman (2007) or Jiang et al. (2007).

The solar magnetic field reaches through the photosphere into the corona. During a solar cycle the structure of the solar and coronal magnetic fields changes drastically.

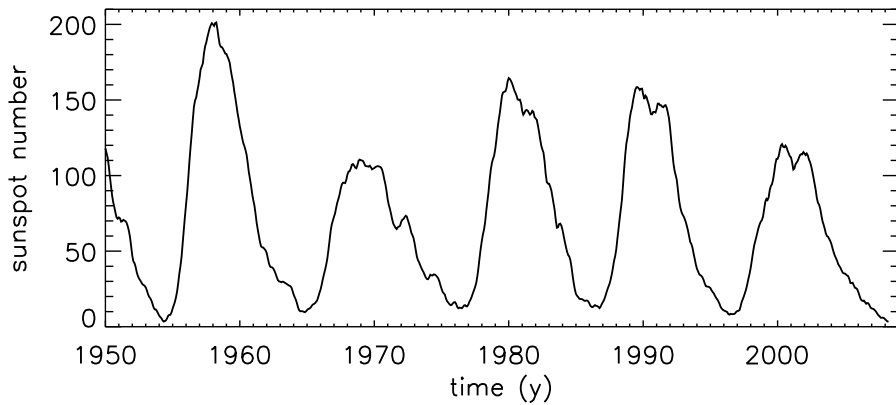


*Figure 2.2: The sunspot numbers from 1950 to 2008. The data shows an almost regular variation with a quasi-periodicity of  $\sim 10 - 13$  years. (Sunspot data taken from the National Geographic Data Center, 2008)*

This is displayed in Fig. 2.3. During the period of solar minimum there are closed field lines in the equatorial region, the so-called streamer belt, while the magnetic field over the poles is arranged in open field lines, the so-called polar coronal holes (PCH). During solar maximum the field changes its almost symmetric structure to closed loops and open field lines are both distributed around the Sun. After  $\sim 11$  years the coronal magnetic field retrieves its original configuration but with opposite polarity.

The strong variation of the magnetic field structure close to the Sun during the solar cycle implies strong modifications of the heliospherical structure. These dependences are discussed below, especially for the solar wind in this chapter and for the heliospheric magnetic field in chapter 3.

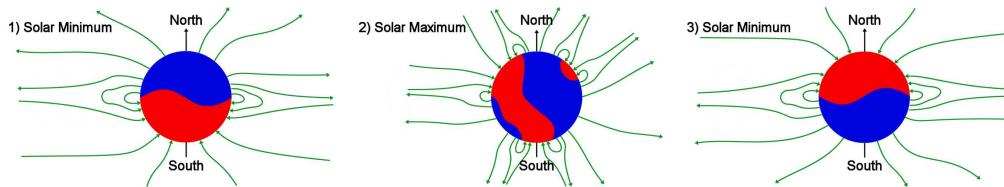


*Figure 2.3: The coronal magnetic field during a solar cycle. At solar minimum closed loop structures can be found in the equatorial region of the Sun (streamer belt). Open field lines form the so-called polar coronal holes at higher heliographic latitudes. During solar maximum the magnetic field configuration consists of loops and open field lines distributed around the Sun. After  $\sim 11$  years the structure of the coronal magnetic field retrieves its original condition but with opposite polarity. (Adopted from Forsyth, 2001)*

## The Solar Wind

Observing comets with their tails always pointing away from the Sun, Biermann (1951) concluded that there has to be a corpuscular flow streaming away from the Sun. Parker (1958) showed that the solar corona cannot be in a static equilibrium: assuming the corona to extend infinitely away from the Sun, he could demonstrate the pressure of a static coronal plasma at such distances to be higher than the pressure that is estimated today for the LISM. This result led to the concept of a constantly expanding solar corona, a phenomenon Parker later called the solar wind. Shortly after the theory had been developed, the Mariner II spacecraft revealed “a measureable flow of plasma from the direction of the Sun” (Neugebauer and Snyder, 1962) with velocities ranging from 400 – 700 km/s, see also Neugebauer and Snyder (1966).

Following the first measurements by Mariner II, several other missions were launched to explore the interplanetary space, revealing that the SW plasma basically consists of protons and electrons with a small fraction of helium. The proton density of the SW near the Earth’s orbit is  $n_p \approx 6 \text{ cm}^{-3}$  with an average flow speed of  $u_{\text{sw}} \approx 470 \text{ km/s}$  and temperatures around  $T_{\text{sw}} \approx 10^5 \text{ K}$  (Prölss, 2004). The SW speed is supersonic ( $c_{\text{sw}} = \sqrt{2k_B T_{\text{sw}}/m_p} \approx 40 \text{ km/s}$ ) and superalfvénic ( $v_A = \sqrt{B^2/(\mu_0 m_p n_p)} \approx 45 \text{ km/s}$ ). It is highly variable, covering a range from 170 km/s up to 2000 km/s which is classified as slow or fast solar wind, respectively.

In October 1990 the Ulysses mission was launched to leave the ecliptic and detect the solar wind and energetic particles over the solar poles. Figure 2.4 presents the solar wind speed measurements by the SWOOPS (Solar Wind Observations Over the Poles of the Sun) instrument aboard Ulysses in dependence on the solar activity cycle. While the lower panel displays the sunspot number, the upper two panels show the SW speed measured during these periods. During solar minimum (upper left panel) the SW velocity around the ecliptic plane has values around  $u_{\text{sw}} \approx 400 \text{ km/s}$ . These slow streams are interrupted by several fast solar wind streams. Above a heliographic latitude of  $\theta \approx 20^\circ$  the SW speed rises up to 800 km/s. The time of solar maximum is illustrated in the upper right panel and reveals different solar wind conditions. The SW flows with an average velocity of  $\sim 400 \text{ km/s}$ , disturbed by a large number of high speed streams.

Krieger et al. (1973) discovered that the fast solar wind has its origin in coronal holes, where open magnetic field lines allow the coronal plasma to flow away from the Sun more easily. This process can be deduced from the magnetic field structure in the solar corona shown in Fig. 2.3. During a solar minimum period closed magnetic field lines dominate the equatorial region of the Sun, while the field lines at higher latitudes are open. The SW plasma streaming radially away from the Sun is restrained by the magnetic field in the ecliptic, but it can leave the corona easily over the poles, where it can flow along the magnetic field lines. Therefore, the SW speed is low near the ecliptic and high at higher latitudes. The same explanation can be applied to the SW during solar maximum. Closed field lines and coronal holes are distributed around the Sun. The consequence of such a magnetic field structure is the latitudinal variability

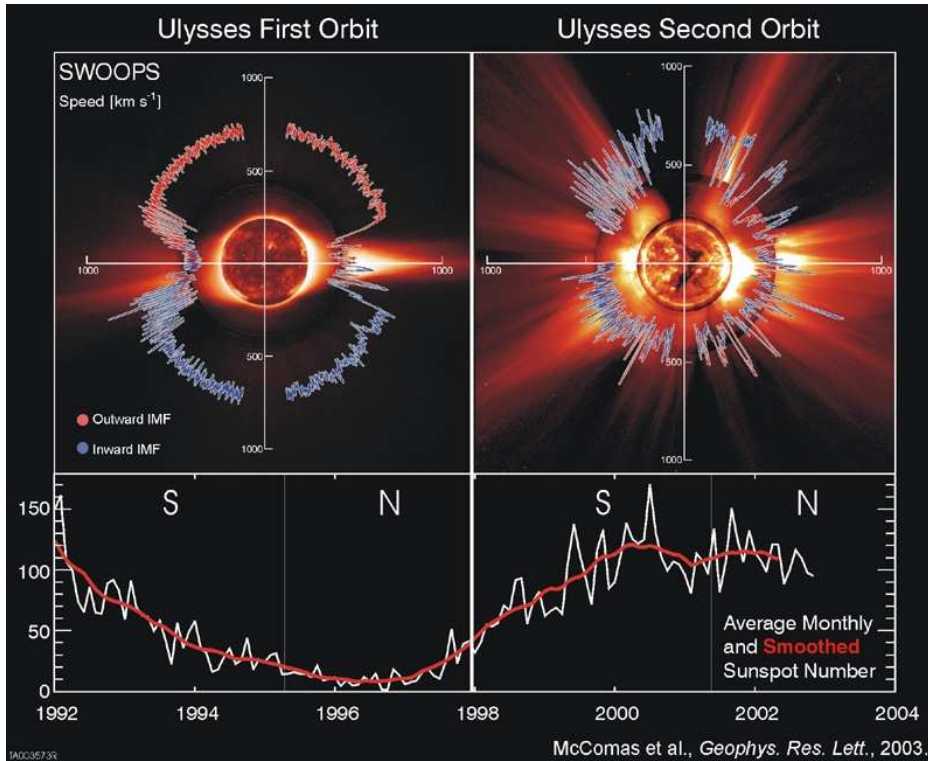


Figure 2.4: The solar wind speed measured by the SWOOPS instrument during the first two Ulysses orbits. The lower panel illustrates the sunspot number, an indicator for the solar activity. During the solar minimum period (upper left panel) near the ecliptic plane SWOOPS measured a solar wind speed of  $u_{\text{SW}} \approx 400$  km/s interrupted by several high speed streams. At higher heliographic latitudes ( $\theta > 20^\circ$ ) the SW speed rises up to 800 km/s. The time of solar maximum (upper right panel) reveals a SW speed of  $\sim 400$  km/s at all latitudes disturbed by a large number of fast SW streams. (Taken from McComas et al., 2003)

of the SW speed as measured by Ulysses.

The solar wind is the carrier of the heliospheric magnetic field (HMF). Close to the Sun the coronal magnetic field controls the plasma motion. In the higher corona the plasma and magnetic field parameters change and the plasma becomes dominant. The coronal magnetic field is frozen into the SW plasma and is carried into the heliosphere to build up the HMF. This process and the HMF structure are discussed in more detail in chapter 3.

## Corotating Interaction Regions

In the early 20<sup>th</sup> century, geomagnetic storms occurring regularly with the same period as the solar rotation were measured (Maunder, 1905). However, their origin could not

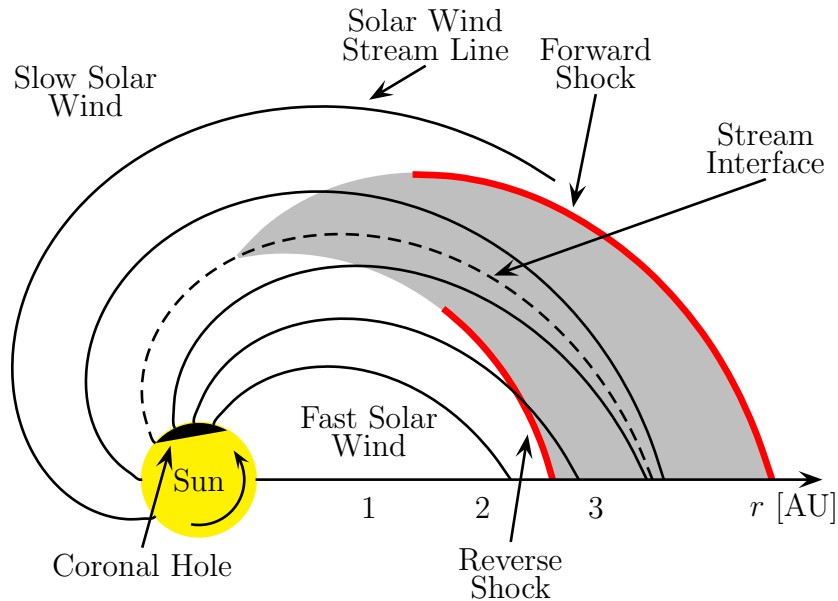


Figure 2.5: The formation of a corotating interaction region. In this figure the ecliptic is displayed from the north. The stream lines connecting the SW volumes originating from the same region at the Sun form archimedean spirals. From the coronal hole the fast SW flows into the heliosphere to interact with the slow SW. Since both plasma flows cannot penetrate each other, a stream interface evolves. At larger distances, a forward and reverse shock develop. (Adopted from Pröls, 2004)

be found at that time. When in-situ measurements in space became possible, these phenomena were associated with recurring particle events in combination with two shocks.

The source of these corotating interaction regions (CIRs) are persistent coronal holes (CHs) expanding to low latitudes during the solar minimum phase. The fast solar wind interacts with the slow solar wind, as shown in Fig. 2.5. Due to the solar rotation the SW stream lines connecting the plasma originating from the same region at the Sun take the form of archimedean spirals. Close to the Sun, the slow and fast streams move almost parallel to each other, so no interaction occurs. At larger distances, the increasing curvature of the stream lines causes the fast SW to flow behind the slow SW. Since the magnetic field is frozen in the SW, a mixing of both streams does not occur, so a stream interface separates the slow and fast flows. Therefore, the radial velocity components of the two successively moving streams are adjusted. Two shocks build up when the velocity components perpendicular to the stream interface become supersonic: a forward shock in front of and a reverse shock behind the stream interface. This usually occurs at distances larger than 2 AU from the Sun (Gosling et al., 1976). Another characteristic feature of CIRs are energetic particles accelerated at the CIR shocks, which can also be detected with a period of  $\sim 26$  days (Pröls, 2004).



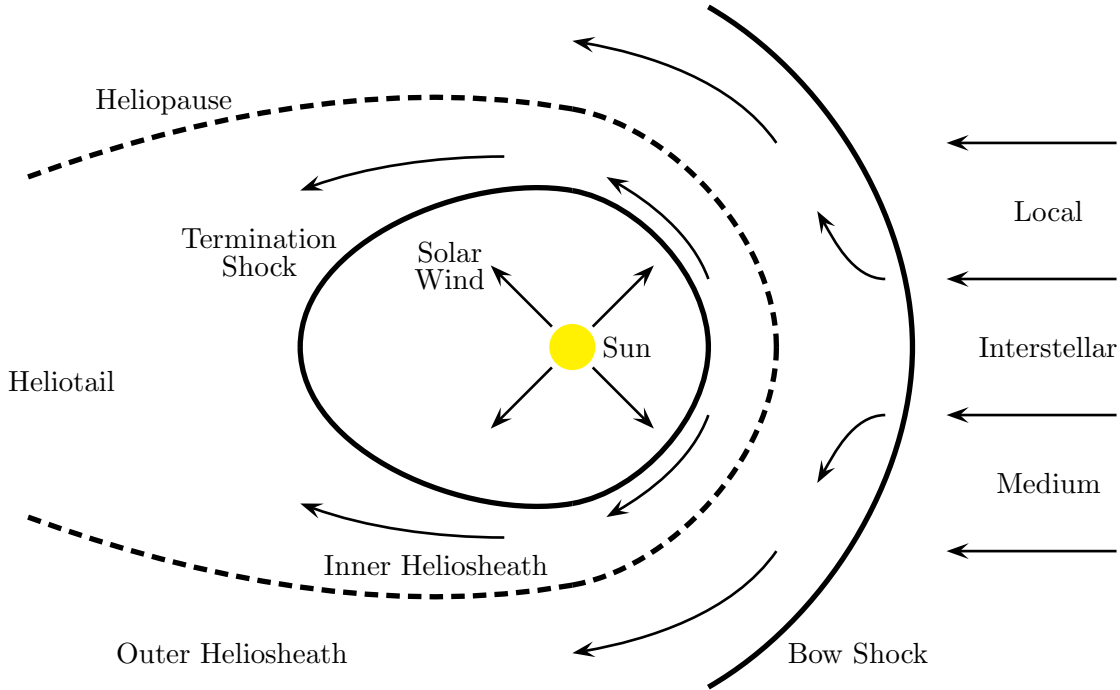


Figure 2.6: A schematic illustration of the heliosphere in the Sun’s rest frame. The solar wind flows radially away from the Sun with supersonic speed. The local interstellar medium (LISM) flows toward the Sun from the right. The structure of the heliospheric boundary with the termination shock (TS), heliopause (HP) and bow shock (BS) is displayed. (Adopted from Fichtner and Scherer, 2000)

## The Heliospheric Boundary

The solar wind pushes away the LISM plasma around the Sun, since both plasmas cannot penetrate each other. Figure 2.6 displays a schematic overview of the heliosphere and its boundaries in the Sun’s rest frame. The SW streams radially away from the Sun with a supersonic speed ranging from 400 to 800 km/s until it reaches the termination shock (TS) where it is decelerated. Kinetic energy is converted to thermal energy and the SW is heated from  $T_{\text{SW}} \approx 8 \cdot 10^4$  K up to a temperature of  $T_{\text{SW}} \approx 10^6$  K. In the heliosheath the SW plasma flows with a subsonic speed lower than 100 km/s ( $c_{\text{SW, heliosheath}} \approx 130$  km/s). In this picture, the LISM flows toward the Sun from the right side with a speed of 25 km/s. It is decelerated at the bow shock (BS). A layer separating both plasmas – the heliopause (HP) – evolves and both the SW and the LISM are deflected to stream in the same direction in the heliosheath. Similar to the interaction of the Earth’s magnetosphere with the SW, a long heliospherical tail (heliotail) is formed in the downstream direction.

The heliospheric boundary received great attention when the Voyager 1 spacecraft crossed the TS at a distance of 94 AU on 16th December 2004 (Fisk, 2005). Voyager 2

followed on 30th August 2007 at a distance of 84 AU (Jokipii, 2008). Both spacecraft provide unique and surprising data for their local positions in the heliosheath and explore the structure of the heliospheric boundary. A global view of this region was recently provided by the Interstellar Boundary Explorer (McComas et al., 2009) and improve our concepts and models of the heliosphere and its boundary region.



# Chapter 3

## The Heliospheric Magnetic Field

The interplanetary space is filled with a globally structured large scale magnetic field. This heliospheric magnetic field (HMF) is subject of numerous scientific studies and discussions since its discovery (Burger, 2005, and references therein). This chapter focuses on the description of the most common HMF models.

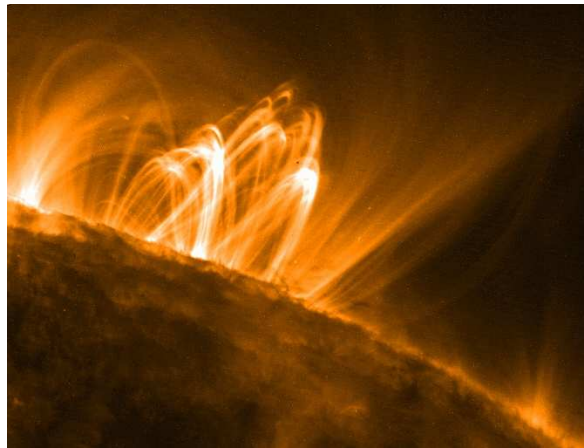


*Figure 3.1: A TRACE image of the solar corona. Close to the Sun the plasma is caught in the solar magnetic field and forced to move along its loop structure. (Taken from the Trace Web Site, 2008)*

The origin of the HMF is located close to the Sun in its corona. There the plasma and the magnetic field interact in order to develop a complex structure. In such a szenario, the ratio of the plasma pressure to the magnetic pressure  $\beta = p_{\text{plasma}}/p_B$  describes whether the plasma ( $\beta > 1$ ) or the magnetic field ( $\beta < 1$ ) plays the dominant role. Figure 3.1 shows an image of the low corona taken by the TRACE satellite. In this region, the plasma is caught in the loop structures of the magnetic field. In the higher corona, the characteristics of the plasma and the magnetic field change and the plasma becomes dominant. The sphere around the Sun, where this change occurs, is

called the source surface of the HMF. From there, the coronal magnetic field is carried into the heliosphere by the solar wind.

## The Parker Model of the Heliospheric Magnetic Field

Parker (1958) developed a model describing the global structure of the HMF. It was shown to be a reasonable approximation in the ecliptic by spacecraft observations (Ness and Burlaga, 2001). He derived an analytical formula based on simple assumptions:

1. Beyond the source surface the coronal magnetic field is frozen into the solar wind.
2. The solar wind flows radially away from the Sun beyond the source surface.
3. The Sun rotates with an angular speed  $\Omega_s$ .
4. The Sun's rotational and magnetic axes are aligned.

A source region of the solar wind at the source surface rotates with the angular speed  $\Omega_s$  of the Sun with respect to the solar rotational axis. Combining the angular motion of this plasma source

$$\begin{aligned} \frac{\phi - \phi_0}{t - t_0} &= \frac{v_{\text{rot}}(\theta_0)}{R_s} = \frac{\Omega_s R_s \sin \theta_0}{R_s} \\ \Rightarrow t - t_0 &= \frac{\phi - \phi_0}{\Omega_s \sin \theta_0} \end{aligned} \quad (3.1)$$

and the radial motion of a plasma volume flowing radially away from the source

$$r(t) = R_s + u_{\text{sw}}(t - t_0) \quad (3.2)$$

one can derive an expression for a solar wind streamline  $r(\phi)$  on which all plasma volumes emanating from the same source region can be found in dependence on their heliographic colatitude  $\theta$  and longitude  $\phi$ :

$$r(\phi) = R_s + \frac{u_{\text{sw}}}{\Omega_s \sin \theta_0} (\phi - \phi_0), \quad (3.3)$$

with the solar radius  $R_s$ , the solar wind speed  $u_{\text{sw}}$ , the rotational speed of the Sun  $v_{\text{rot}}$  and the longitudinal and colatitudinal positions  $\phi_0$  and  $\theta_0$  of the source on the Sun. The formation of these streamlines is visualised in Fig. 3.2. A line connecting all plasma volumes originating from the same source represents an archimedean spiral, the so-called Parker spiral. Since the magnetic field is frozen into the solar wind, all plasma volumes on a spiral that can be described by equation (3.3) are magnetically connected.

With these considerations one can already conclude that the  $\theta$ -component of the magnetic Field vanishes (i.e.  $B_\theta = 0$ ). A relation between the other two components

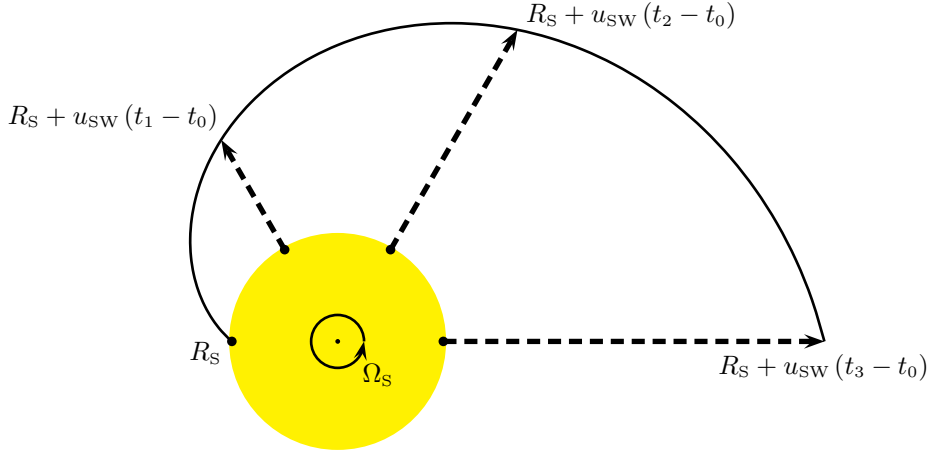


Figure 3.2: The construction of the Parker spiral. The connection of all plasma volumes emanating from the same source region on the source surface of the HMF shows that a streamline of the solar wind can be described as an Archimedean spiral, see equation (3.3).

can be found by having a closer look at the angle between the spiral and the radial direction (see Fig. 3.3):

$$\tan \psi = -\frac{B_\phi}{B_r} = \frac{rd\phi}{dr} = \frac{r \frac{v_{\text{rot}}}{R_S} dt}{u_{\text{SW}} dt} = \frac{r\Omega_S \sin \theta}{u_{\text{SW}}}, \quad (3.4)$$

To obtain a complete expression for the so-called Parker field in spherical polar coordinates one has to solve the Maxwell equation  $\vec{\nabla} \cdot \vec{B} = 0$ :

$$\frac{1}{r^2} \frac{\partial}{\partial r} (r^2 B_r) + \frac{1}{r \sin \theta} \frac{\partial}{\partial \phi} B_\phi = 0 \quad (3.5)$$

Because of the rotational symmetry of the magnetic field the second summand on the left-hand side becomes 0 and the radial component of the  $\vec{B}$ -field can be derived:

$$\frac{1}{r^2} \frac{\partial}{\partial r} (r^2 B_r) = 0 \quad (3.6)$$

$$B_r = \frac{\text{const.}}{r^2} \quad (3.7)$$

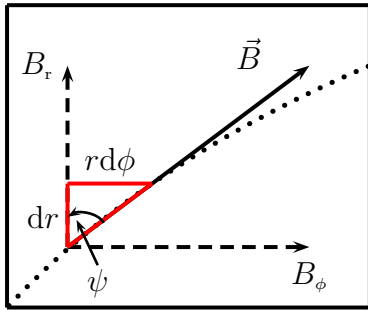
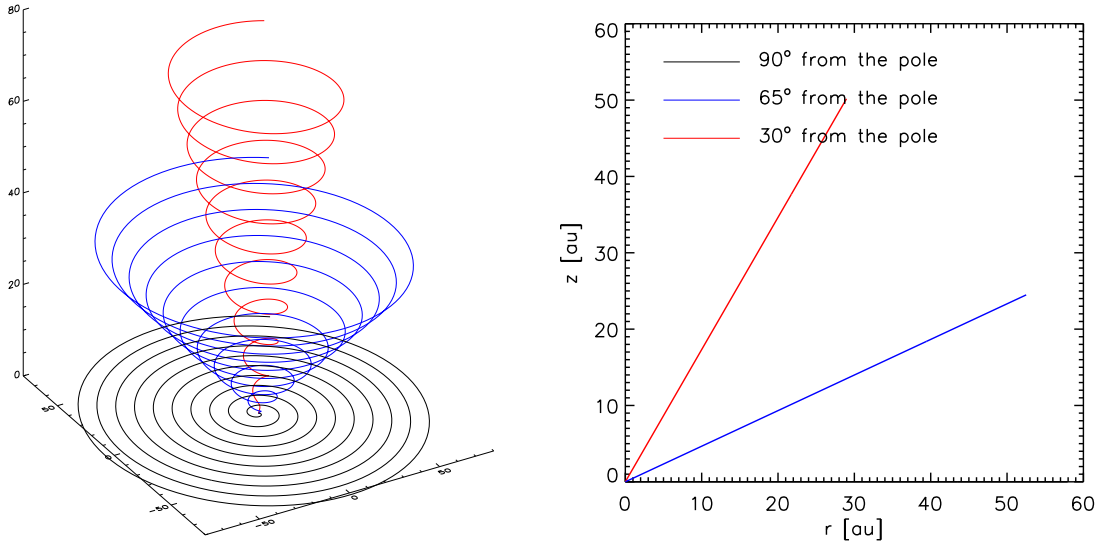


Figure 3.3: The angle  $\psi$  between Parker spiral (dotted line) and radial direction.

The missing constant can be obtained by a measured value  $B_0$  at the Earth's orbit  $r_0$ . Together with equation (3.4) this leads to a full expression for the HMF:

$$\begin{aligned}\vec{B}(r, \theta, \phi) &= B_r \vec{e}_r + B_\phi \vec{e}_\phi \\ &= B_0 \left(\frac{r_0}{r}\right)^2 \left(\vec{e}_r - \left(\frac{r\Omega_S}{u_{\text{SW}}}\right) \vec{e}_\phi\right)\end{aligned}\quad (3.8)$$

To visualise the global structure of the Parker field, three magnetic field lines with footpoints at different colatitudes but the same longitude are displayed in two different plots in Fig. 3.4. The left panel shows the corresponding three-dimensional spirals. One can realise that the field lines form cones with the fixed colatitudes  $\theta_{\text{black}} = 90^\circ$ ,  $\theta_{\text{blue}} = 65^\circ$  and  $\theta_{\text{red}} = 30^\circ$  from the solar north pole. In the right panel the same field lines are illustrated in a different kind of projection. This 2D representation shows the field line height above the ecliptic plane versus their radial distances to the Sun's rotational axis. In this unwound projection the magnetic field appears as straight lines with fixed colatitudes.



*Figure 3.4: Visualisation of the Parker field: The left panel shows three magnetic field lines of Parker's HMF in a 3D illustration. Their footpoints share the same longitude but are located at different colatitudes:  $\theta_{\text{black}} = 90^\circ$ ,  $\theta_{\text{blue}} = 65^\circ$  and  $\theta_{\text{red}} = 30^\circ$  from the solar north pole. The spirals form cones with fixed colatitudes. The right panel displays the same field lines in an unwound 2D projection with the field line height  $z$  above the ecliptic plane versus their radial distances  $r$  to the Sun's rotational axis. In this plot the magnetic field appears to be straight lines with fixed colatitudes.*

Although particle transport will be the main topic of chapter 4 some anticipations for the propagation of charged particles can already be deduced for Parker’s description of the HMF. From basic plasma physics it is known that a magnetic field forces a charged particle to gyrate around a field line. Ignoring drift effects, the center of the circular motion is able to move along the field line to form a helical orbit. For diffusion perpendicular to the magnetic field, the particle has to be scattered. From these simple considerations one expects a low particle transport in latitudinal direction since it requires a motion perpendicular to the magnetic field.

## Evidence, Advantages and Drawbacks

Parker chose a simple and easily conceivable model describing the HMF. It is still widely used in most modulation studies. Spacecraft observations suggest that the Parker model is a reasonable approximation in the ecliptic plane (Ness and Burlaga, 2001, and references therein). However, the Ulysses mission revealed strong discrepancies over the solar poles (Forsyth et al., 1996). The first modifications of the Parker field suggesting such deviations were already published by Jokipii and Kóta (1989) and Smith and Bieber (1991) before the Ulysses measurements. A discussion of these and other modifications can be found in Burger (2005).

## The Heliospheric Current Sheet

The Heliospheric Current Sheet (HCS) can be seen as a layer separating the two heliographic hemispheres with opposite magnetic polarities. It can be described as the solar magnetic equator extending into the heliosphere.

At the source surface the neutral line of the magnetic field is frozen into the solar wind and is carried away radially into the interplanetary space, where it forms a magnetically neutral layer ( $B = 0$ ). As can be seen in Fig. 3.5, the solar magnetic axis  $\vec{M}$  is tilted with respect to the rotational axis  $\vec{\Omega}_s$  by an angle  $\alpha$ . To construct the extension of the neutral line into the surrounding space, the solar rotation needs to be taken into account. This leads to a wavy structure of the HCS.

An analytical expression describing the three-dimensional structure of the HCS can be derived with the help of Fig. 3.6. This figure shows a plane through the solar magnetic equator (dashed circle) which is tilted by the angle  $\alpha$  with respect to a plane through the

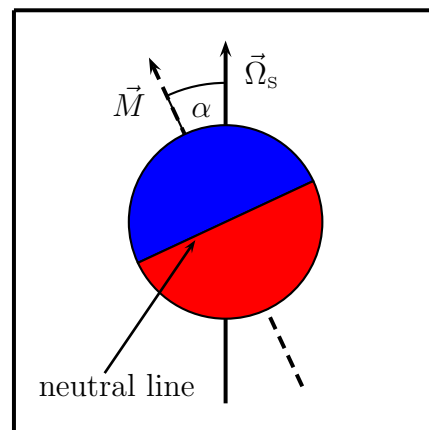


Figure 3.5: The tilt angle  $\alpha$  of the solar magnetic axis  $\vec{M}$  with respect to the rotational axis  $\vec{\Omega}_s$ .

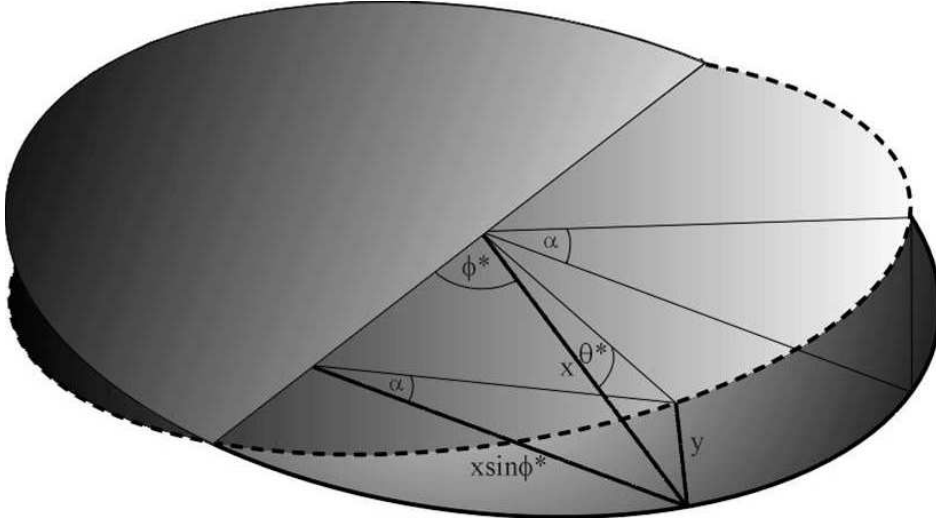


Figure 3.6: Constructing an analytical expression for the three-dimensional HCS. The sketch shows a plane through the solar magnetic equator (dashed line), which is tilted by the angle  $\alpha$  with respect to a plane through the rotational equator (solid line). A triangle with the hypotenuse connecting the center of the Sun with a point on the solar equator is constructed in the equatorial plane and projected onto the magnetic equatorial plane. Here  $\phi^*$  and  $\theta^*$  represent the heliographic longitude and latitude in a coordinate system corotating with the solar equator. From the three resulting triangles one can derive the analytical expression for the HCS given in equation (3.11). (Taken from Krüger, 2005)

rotational equator (solid circle). Now assume a rectangular triangle in the equatorial plane with the hypotenuse connecting the center of the Sun with a point on the solar equator and project it onto the magnetic equatorial plane. Here  $\phi^*$  and  $\theta^*$  represent the heliographic longitude and latitude in a coordinate system corotating with the solar equator. From the three resulting triangles with

$$\tan \alpha = \frac{y}{x \sin \phi^*} \quad \text{and} \quad \tan \theta^* = \frac{y}{x} \quad (3.9)$$

one gets

$$\tan \theta^* = \tan \alpha \sin \phi^*. \quad (3.10)$$

Transforming equation (3.10) from the corotating frame to a fixed observer's frame and introducing the polar angle  $\theta_{\text{HCS}} = \frac{\pi}{2} - \theta^*$  one obtains an expression for the polar angle of the HCS depending on the tilt angle  $\alpha$ , the radial distance to the Sun  $r$ , the radius of the source surface  $r_{\text{SS}}$  and the heliographic longitude  $\phi$ :

$$\theta_{\text{HCS}} = \frac{\pi}{2} - \arctan \left\{ \tan \alpha \sin \left( \phi + \frac{\Omega_{\text{S}} (r - r_{\text{SS}})}{u_{\text{SW}}} \right) \right\}, \quad (3.11)$$

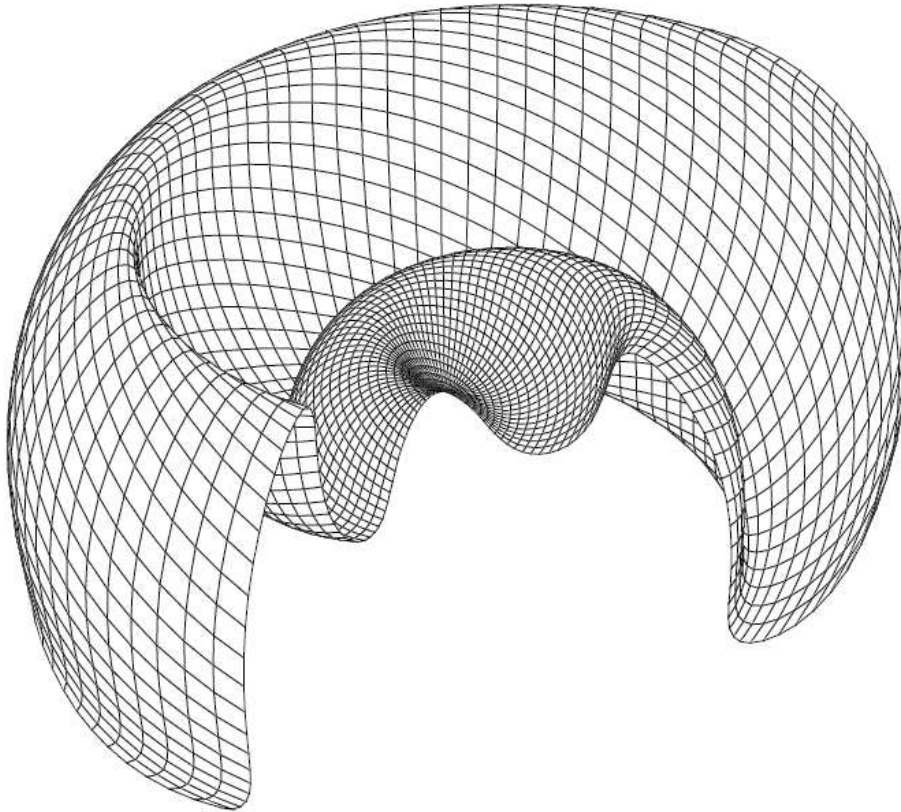


*Figure 3.7: An illustration of the Heliospheric Current Sheet known as the "Ballerina Skirt" which is described by equation (3.11) for a tilt angle of  $\alpha = 30^\circ$  up to a radial distance of 10 AU to the Sun. Its wavy structure becomes evident in this representation. (Taken from Krüger, 2005)*

similar to the expression derived by Kóta and Jokipii (1983). The three-dimensional structure of this current sheet is often referred to as the "ballerina skirt". Figure 3.7 displays the HCS for a tilt angle of  $\alpha = 30^\circ$  up to a radial distance of 10 AU to the Sun. Its wavy structure becomes evident in this representation.

Since the heliospheric current sheet is a very thin layer dividing the heliosphere into two hemispheres with opposite magnetic polarities, the expression for the magnetic field vector  $\vec{B}$  needs to be modified with a function describing a transition from positive to negative polarity at the heliographic colatitude  $\theta_{\text{HCS}}$  of the HCS. This can be achieved by introducing the Heaviside step function  $H(\theta - \theta_{\text{HCS}})$ :

$$\vec{B} = \vec{B}_{\text{HMF}} (1 - 2H(\theta - \theta_{\text{HCS}})) \quad (3.12)$$

where  $\vec{B}_{\text{HMF}}$  is the magnetic field vector for a heliospheric magnetic field model, e.g.

one of the models described in this chapter, and

$$H(\theta - \theta_{\text{HCS}}) = \begin{cases} 0, & \theta < \theta_{\text{HCS}} \\ 1, & \theta > \theta_{\text{HCS}}. \end{cases} \quad (3.13)$$

## The Fisk Model of the Heliospheric Magnetic Field

Particles accelerated at corotating interaction regions can be measured in the ecliptic plane with a period of  $\sim 26$  days (see chapter 2). In a Parker-type HMF as described above, these particles are expected to stay at low heliographic latitudes (Gosling and Pizzo, 1999). However, the Ulysses fast latitude scan (FLS) discovered 26-day variations even at the highest latitudes (Simpson et al., 1995; Dunzlaff et al., 2008) during the solar minimum period. A possible origin of this phenomenon are CIR-accelerated particles propagating polewards from the ecliptic by a process that is still under discussion. Another result of the Ulysses FLS is a latitudinal gradient of the particle measurements which is significantly lower than expected from the simple Parker HMF model (Simpson et al., 1996; McKibben et al., 1996).

Two theories were developed to explain these surprising Ulysses measurements. Kóta and Jokipii (1995a) introduced a large cross-field diffusion at higher latitudes during the solar minimum phase motivated by large turbulence in the fast solar wind (see chapter 4). Under these conditions, CIR-accelerated particles can propagate in latitudinal direction more easily and cause the 26-day variations measured by Ulysses.

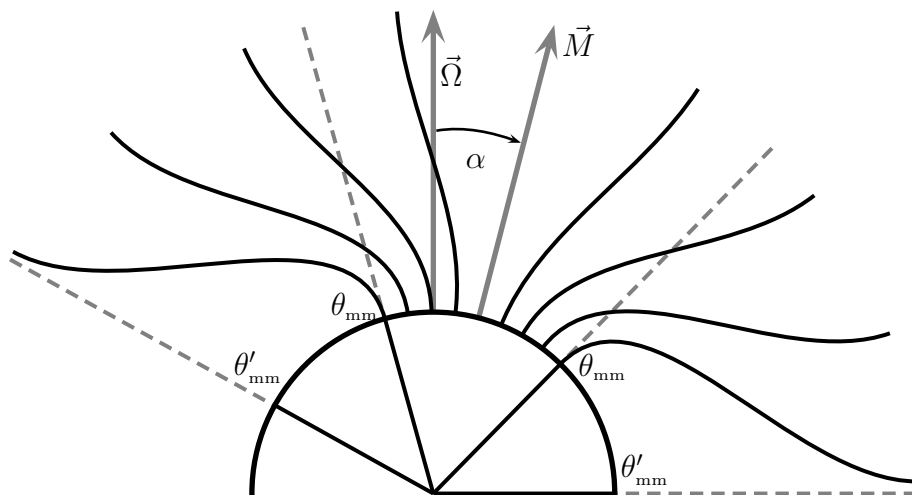


*Figure 3.8: Field line expansion inside a polar coronal hole. The sketch illustrates the expansion of the magnetic field lines inside a polar coronal hole from the photosphere to the high corona. The PCH is symmetric to the magnetic field axis  $\vec{M}$ . In a heliomagnetic coordinate system, the PCH boundary expands from the angle  $\theta_{\text{mm}}$  in the photosphere to  $\theta'_{\text{mm}}$  in the corona. (Adopted from Fisk, 1996)*



Fisk (1996) chose a different approach to describe the HMF during solar minimum conditions. He developed an HMF model with magnetic field lines spreading from the ecliptic to high latitudes. Energetic particles can diffuse easily along these field lines and reach the polar region to cause the variations mentioned above.

## The Magnetic Field Foot Points on the Source Surface

The Fisk HMF model is based on the assumption that the solar rotational axis  $\vec{\Omega}$  and the magnetic field symmetry axis  $\vec{M}$  are tilted by an angle  $\alpha$ . The magnetic footpoints rotate differentially around  $\vec{\Omega}$  in the photosphere, and the magnetic field lines expand symmetrically but non-radially around  $\vec{M}$ , see Fig. 3.8. The PCH is symmetric to  $\vec{M}$ . The PCH boundary field lines expanding from the heliographic colatitude  $\theta_{\text{mm}}$  in the photosphere to  $\theta'_{\text{mm}}$  on the source surface in heliomagnetic coordinates.

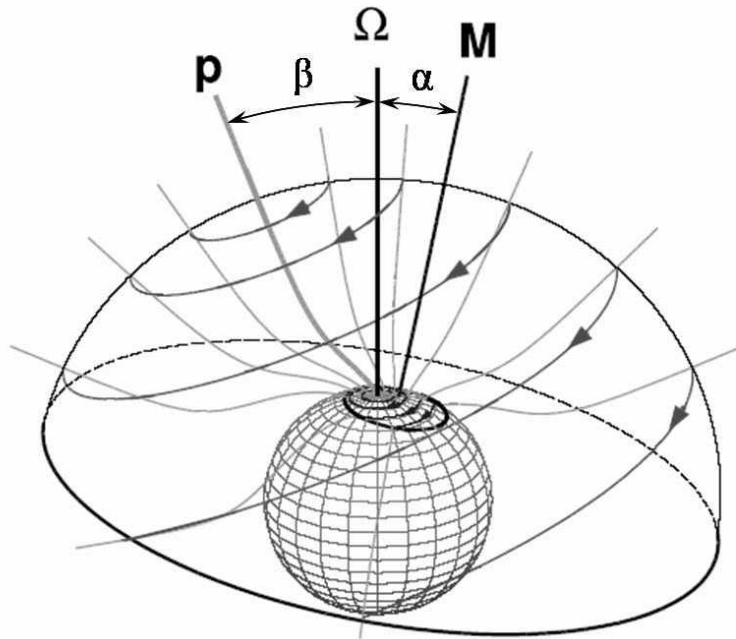


*Figure 3.9: Field line expansion and footpoint motion on the source surface. The illustration shows the field line expansion from the photosphere to the source surface inside a PCH in the northern hemisphere of the Sun in a frame corotating with the solar equator. The magnetic field footpoints in the photosphere are mapped to the source surface by the field lines. The resulting footpoint trajectories on the source surface are shown. The PCH boundary stays at constant heliomagnetic longitudes on both the photosphere and the source surface. The magnetic field symmetry axis  $\vec{M}$  is tilted by an angle  $\alpha$  with respect to the solar rotational axis  $\vec{\Omega}$ . The virtual axis  $\vec{p}$  is defined by the field line connecting the solar pole to the source surface and is tilted at an angle  $\beta$  with respect to  $\vec{\Omega}$ . (Taken from Zurbuchen et al., 1997)*

The second essential postulate is related to the rotation of the magnetic field axis. It is assumed that  $\vec{M}$  corotates rigidly with the solar equator, while the magnetic footpoints rotate differentially in the photosphere. Therefore, non-equatorial photospheric footpoints rotate slower around  $\vec{\Omega}$  than the magnetic field axis. This leads to a footpoint motion not only in heliographic, but also heliomagnetic coordinates. Since the non-radial expansion of a magnetic field line depends on the heliomagnetic coordinate of its photospheric footpoint, this footpoint is mapped to different heliographic latitudes on the source surface during one rotation period. This leads to a motion in heliolongitude and heliolatitude and, therefore, to a global structure of the HMF different from that suggested by Parker. The resulting trajectories of the HMF footpoints inside a PCH on the source surface are displayed in Fig. 3.9 in a frame corotating with the solar equator. Zurbuchen et al. (1997) derive the meridional and azimuthal components of the footpoint velocity

$$\begin{aligned} v_\theta &= r\omega \sin \beta \sin \phi \\ v_\phi &= r\omega (\sin \beta \cos \theta \cos \phi + \cos \beta \sin \theta) \end{aligned} \quad (3.14)$$

on the source surface in the same reference frame with the differential rotation rate  $\omega$ . The so-called Fisk-angle  $\beta$  is defined by the field line originating at the heliographic pole. This field line does not experience any differential rotation and therefore always maps to the same point on the source surface, defining the virtual axis p.  $\beta$  is the angle between this axis and the rotational axis  $\Omega$ .

## The Structure of the Fisk Heliospheric Magnetic Field

For a solar wind flowing radially outward with the constant SW speed  $u_{\text{SW}}$ , Zurbuchen et al. (1997) obtain a relation of the coordinates  $r_{\text{sl}}$ ,  $\theta_{\text{sl}}$  and  $\phi_{\text{sl}}$  of a solar wind streamline for the Fisk field in a corotating reference frame:

$$\begin{aligned} \frac{\partial \theta_{\text{sl}}}{\partial r_{\text{sl}}} &= \frac{\omega}{u_{\text{SW}}} \sin \beta \sin \left( \phi_{\text{sl}} + \frac{\Omega_{\text{S}} r_{\text{sl}}}{u_{\text{SW}}} - \phi_0 \right) \\ \frac{\partial \phi_{\text{sl}}}{\partial r_{\text{sl}}} &= \frac{\omega}{u_{\text{SW}}} \sin \beta \frac{\cos \theta_{\text{sl}}}{\sin \theta_{\text{sl}}} \cos \left( \phi_{\text{sl}} + \frac{\Omega_{\text{S}} r_{\text{sl}}}{u_{\text{SW}}} - \phi_0 \right) \\ &\quad + \frac{\omega}{u_{\text{SW}}} \cos \beta \sin \left( \phi_{\text{sl}} + \frac{\Omega_{\text{S}} r_{\text{sl}}}{u_{\text{SW}}} - \phi_0 \right) - \frac{\Omega_{\text{S}}}{u_{\text{SW}}} \end{aligned} \quad (3.15)$$

The assumptions of a radial and uniform magnetic field on the source surface,

$$\frac{B_\theta}{B_\phi} = \frac{\partial \theta_{\text{sl}} / \partial r_{\text{sl}}}{\sin \theta_{\text{sl}} \partial \phi_{\text{sl}} / \partial r_{\text{sl}}} \quad (3.16)$$

and  $\vec{\nabla} \cdot \vec{B} = 0$ , lead to an analytic expression for the magnetic field vector in a fixed observer's frame:

$$\begin{aligned}
 B_r &= B_0 \left( \frac{r_0}{r} \right)^2 \\
 B_\theta &= \frac{B_0 r_0^2}{u_{\text{sw}} r} \omega \sin \beta \sin \left( \phi + \frac{\Omega_s r}{u_{\text{sw}}} - \phi_0 \right) \\
 B_\phi &= \frac{B_0 r_0^2}{u_{\text{sw}} r} \left( \omega \left[ \cos \beta \sin \theta + \sin \beta \cos \theta \cos \left( \phi + \frac{\Omega_s r}{u_{\text{sw}}} - \phi_0 \right) \right] - \Omega_s \sin \theta \right)
 \end{aligned} \tag{3.17}$$

The global structure of the Fisk HMF is compared to the Parker field in Fig. 3.10. Both illustrations show magnetic field lines originating at  $70^\circ$  northern latitude and extending out to a radial distance of 20 AU to the Sun. The bottom panel clearly shows the spiral structure of the Parker field with the field lines forming cones. The top panel indicates that in a Fisk-type HMF the field lines cover a large range in latitude.

The Fisk field can only be valid inside PCHs and the inner region of persistent CHs. A different behaviour of the footpoint motion is found outside of the coronal

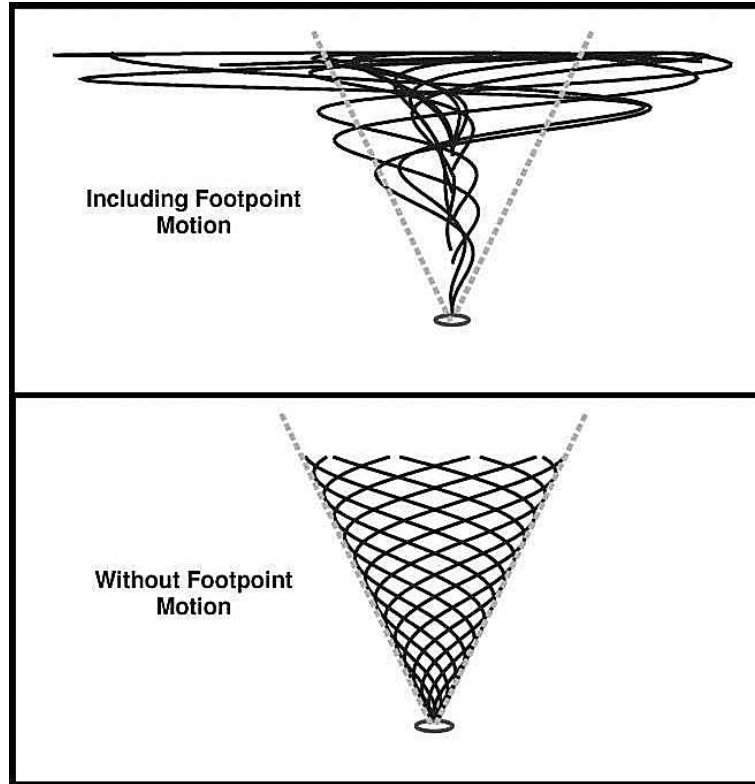


Figure 3.10: The expected magnetic field line configuration in a Fisk (top panel) and a Parker (bottom panel) HMF. The two plots show magnetic field lines originating at a latitude of  $70^\circ$  in the photosphere extending out to 20 AU. (Taken from Fisk et al., 1999b)

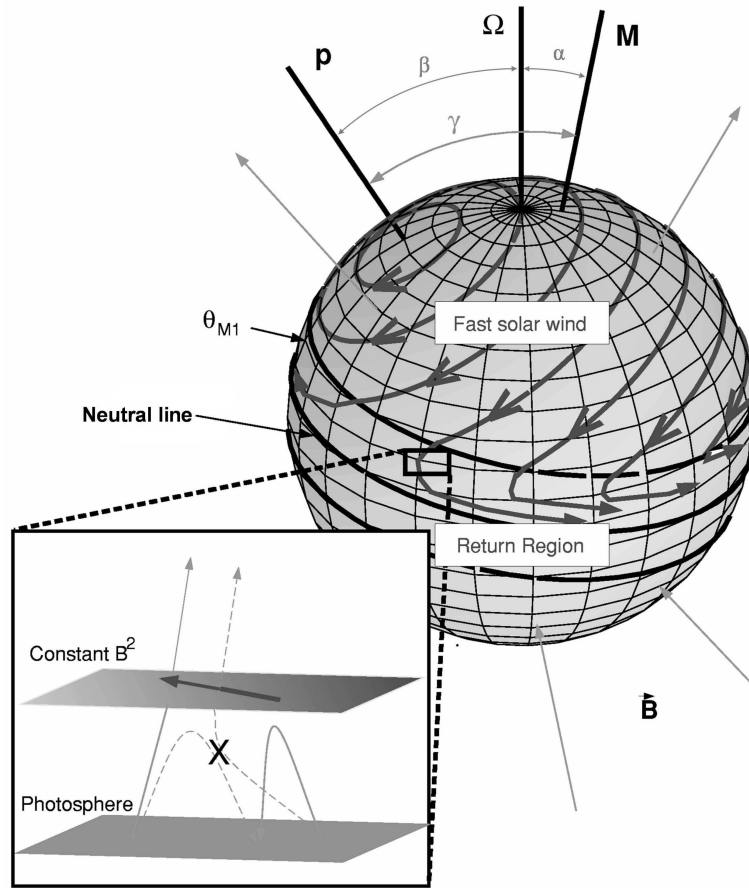


Figure 3.11: Footpoint trajectories on the source surface including the boundary conditions of the footpoint motion. The PCH boundary is located at  $\theta_{M1}$  in helio-magnetic coordinates. When a magnetic field footpoint leaves the PCH, it enters the so-called return region located between the PCH and the magnetic equator. It propagates along the magnetic equator to return into the PCH on the other side of the Sun. This transport process is the result of a diffusion process caused by reconnection of open and closed field lines. (Taken from Fisk et al., 1999b)

holes. Investigating the boundary conditions of the magnetic field footpoint motion, Fisk et al. (1999b) made the assumption of a steady magnetic field on the source surface, which is reasonable during solar minimum conditions (Balogh et al., 1995), and a uniform magnetic field strength on the source surface. The magnetic field lines do not cross the magnetic equator and, therefore, do not change polarity. The latter leads to a vanishing meridional component of the footpoint velocity close to the magnetic equator. The consequence of these assumptions is a non-zero, divergence-free velocity field of the footpoint motion, see Fig. 3.11. The illustration shows the footpoint trajectories on the source surface resulting from the boundary conditions for the footpoint motion discussed above. A magnetic field footpoint leaving the fast solar wind area of the

polar coronal hole enters the return region, where it changes its moving direction and is transported along the magnetic equator due to diffusive reconnection of open and closed field lines to re-enter the PCH on the other side of the Sun. A sketch of the diffusive reconnection motion is given in the lower left panel of Fig. 3.11.

Fisk et al. (1999a) argue that a more realistic description of the footpoint motion inside the return region due to reconnection would be a random walk process. Nevertheless, the smooth trajectories given in Fig. 3.11 represent the averaged motion of the reconnection motion and, therefore, are a reasonable approximation.

## Evidence, Advantages and Drawbacks

Signatures of the Fisk field are expected to be found in both energetic particle and magnetic field measurements. A strong indication for a Fisk-type HMF during solar minimum are the 26-day variations observed in the Ulysses measurements of energetic particles at high latitudes (Burger and Hitge, 2004). Additionally, the overwound structure of the HMF found by Ulysses in the southern hemisphere (Forsyth et al., 1995) can be explained with a Fisk-type magnetic field (Zurbuchen et al., 1997; Fisk et al., 1999b). Zurbuchen et al. (1997) report on systematic variations of the latitudinal and longitudinal components of the magnetic field vector with a period of  $\sim 20$  days found in Ulysses measurements. This effect is predicted by the Fisk field for high latitudes. However, Forsyth et al. (2002) found that it is very difficult to confirm these predicted variations in the Ulysses measurements, a result which is supported by Erdős and Balogh (2005) and Roberts et al. (2007). Nevertheless, the latter authors point out that they still feel the physics behind the Fisk model to be plausible, but Zurbuchen et al. (1997) may have overestimated some of the model parameters.

The boundary of the polar coronal holes is assumed at a fixed heliomagnetic latitude with a north-south symmetry in the Fisk HMF model. This also leads to a symmetry with respect to the magnetic field axis  $\vec{M}$ . Therefore, the PCH symmetry axis changes its inclination during the solar cycle. However, observations show that the PCH boundary is very ragged and time-dependent with no obvious north-south symmetry (Hoeksema, 1995; Roelof et al., 1997) and the PCHs stay at the heliographic poles during the solar cycle (Waldmeier, 1981; Webb et al., 1984).

Refinements of the Fisk field were suggested by Schwadron (2002) and Schwadron and McComas (2003). These authors derive a description of the global HMF structure including a solar wind speed depending on the heliographic colatitude  $\theta$  by changing the radial component of the Fisk field to

$$B_r = B_0 \left(\frac{r_0}{r}\right)^2 \left(1 + \frac{r}{u_{sw}^2} \omega \sin \beta \sin \left(\phi + \frac{\Omega_s r}{u_{sw}} - \phi_0\right) \frac{du_{sw}}{d\theta}\right), \quad (3.18)$$

while the  $\theta$ - and  $\phi$ -components remain the same. This is commonly referred to as the Schwadron field. Burger and Hitge (2004) propose a Fisk-Parker hybrid magnetic field model. They implement a transition function depending on the latitude to build up a pure Parker field in the equatorial region and a Fisk field at higher latitudes in the

PCHs. Burger et al. (2008) extend this model to describe its time-dependence during the solar activity cycle and on short time scales. A description of the field models by Schwadron (2002), Schwadron and McComas (2003) and Burger and Hitge (2004) can be found in Burger (2005). The Fisk-Parker hybrid field is described below.

## The Fisk-Parker Hybrid Approach

The original intention of developing a Fisk-Parker hybrid field was to find a theoretical description of the HMF which includes the physics postulated by Fisk (1996) and to obtain the possibility to include the field model in numerical simulations. Additionally, the Fisk-Parker hybrid approach solves some open problems of the pure Fisk field. The first stationary field model was proposed by Burger and Hitge (2004). In three refinements, Krüger (2005), Burger et al. (2008) and Hitge and Burger (2010) added the time dependence on the solar activity cycle and shorter time scales. In this work, the approaches of Burger et al. (2008) and Hitge and Burger (2010) are applied to a propagation model and, therefore, described below.

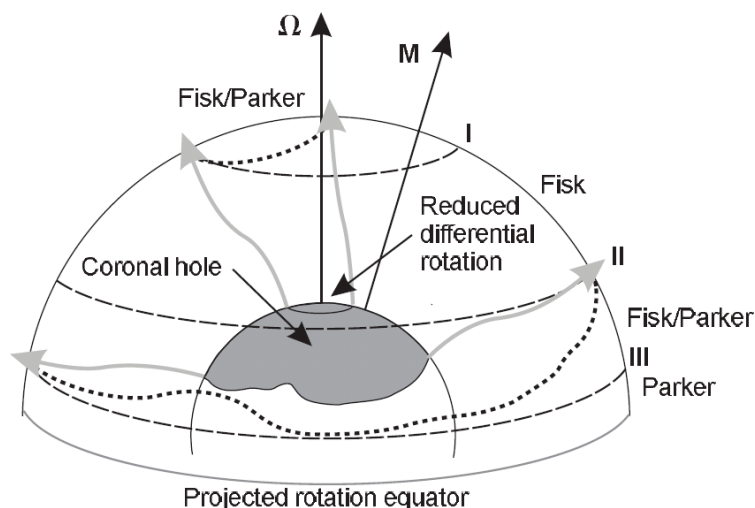


*Figure 3.12: The HMF source surface for the Fisk-Parker hybrid HMF model. Burger et al. (2008) divide the source surface into four regions where the footpoints of the HMF propagate due to different processes, indicated by the three dashed lines labeled I-III and the solar equator. (Taken from Burger et al., 2008)*

Figure 3.12 illustrates the HMF source surface for the Fisk-Parker hybrid model. Burger et al. (2008) divide the source surface into four regions (dashed lines labeled I-III and the solar equator) with different processes dominating the propagation of the HMF footpoints. Beyond III, the footpoint motion occurs only due to diffusive reconnection, leading to a pure Parker field. Between I and II, an ordered motion of

the footpoints is expected, building up a pure Fisk field at these latitudes. There are two areas with a mixture of ordered and diffusive motion of the footpoints (between I and the pole and between II and III). Additionally, the authors assume a reduced differential rotation rate near the solar poles. Therefore, a hybrid of the Fisk and Parker field models is built up in these areas.

This complex field structure is modelled by introducing a transition function  $F_s(\theta)$ :

$$F_s(\theta) = \begin{cases} \left\{ \tanh(\delta_p \theta) + \tanh(\delta_p [\theta - \pi]) - \tanh(\delta_e [\theta - \theta'_b]) \right\}^2 & \text{if } 0 \leq \theta < \theta'_b \\ 0 & \text{if } \theta'_b \leq \theta < \pi - \theta'_b \\ \left\{ \tanh(\delta_p \theta) + \tanh(\delta_p [\theta - \pi]) - \tanh(\delta_e [\theta - \pi + \theta'_b]) \right\}^2 & \text{if } \pi - \theta'_b \leq \theta < \pi \end{cases} \quad (3.19)$$

with the parameters  $\theta'_b$  representing the colatitude III in Fig. 3.12 and  $\delta_p$  and  $\delta_e$  controlling the shape of the transition function. Depending on the heliographic colatitude, it describes the HMF structure as a Fisk-type ( $F_s = 1$ ) or a Parker-type ( $F_s = 0$ ) field. Values between 0 and 1 lead to a Fisk-Parker hybrid. The transition function is shown in Fig. 3.13 for  $\theta'_b = 4/9\pi (\hat{=} 80^\circ)$ ,  $\delta_p = 5$  and  $\delta_e = 5$ .

To implement the refinements described above in the Fisk field, the velocity field of the footpoint motion on the source surface is modified with the transition function  $F_s$ .

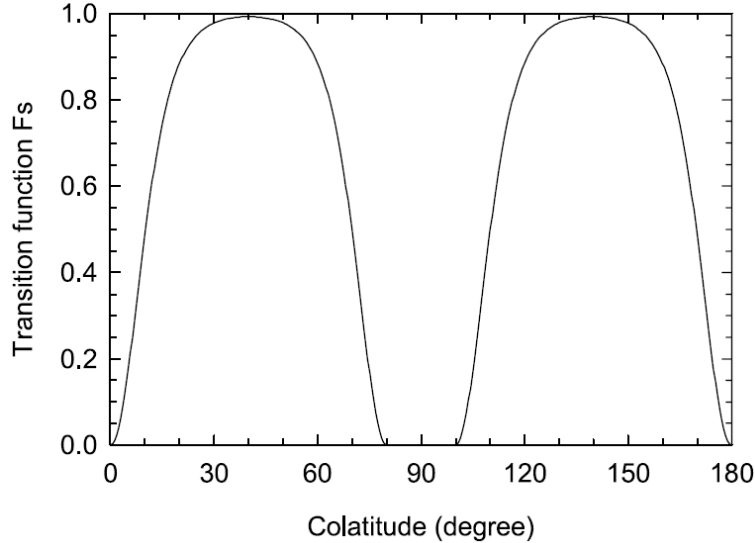


*Figure 3.13: The transition function  $F_s(\theta)$  for the Fisk-Parker hybrid HMF model. The function  $F_s$  describes the transition from a Parker-type to a Fisk-type HMF depending on the heliographic colatitude  $\theta$ . The parameters  $\theta'_b = 4/9\pi (\hat{=} 80^\circ)$ ,  $\delta_p = 5$  and  $\delta_e = 5$  were used. (Taken from Burger et al., 2008)*

Burger et al. (2008) derive the new divergence-free velocity field in a frame corotating with the solar equator

$$\begin{aligned}
 u_\theta &= r_{\text{SS}} \omega^* \sin \beta^* \sin \phi_\Omega & (3.20) \\
 u_\phi &= r_{\text{SS}} \left( \omega^* \sin \beta^* \cos \theta \cos \phi_\Omega + \omega^* \cos \beta^* \sin \theta \right. \\
 &\quad \left. + \frac{d\omega^*}{d\theta} \sin \beta^* \sin \theta \cos \phi_\Omega + \omega^* \frac{d\beta^*}{d\theta} \cos \beta^* \sin \theta \cos \phi_\Omega \right),
 \end{aligned}$$

with the radius of the source surface  $r_{\text{SS}}$ , the heliographic colatitude and longitude  $\theta$  and  $\phi_\Omega$ , respectively, and the parameters

$$\begin{aligned}
 \beta^*(\theta) &= \beta F_s(\theta) & (3.21) \\
 \omega^*(\theta) &= \omega F_s(\theta)
 \end{aligned}$$

Figure 3.14 shows the footpoint trajectories on the source surface in a frame corotating with the solar equator for the values  $\alpha = 12^\circ$ ,  $\omega = \Omega/4$ ,  $\delta_p = 5.0$  and  $\delta_e = 5.0$ . The  $p$ -axis is defined by the field line mapped to the source surface from the rotational axis in the lower photosphere. Therefore,  $p$  does not move in colatitude or longitude on the source surface.  $\beta$  is the angle between  $p$  and the rotational axis  $\Omega$ .

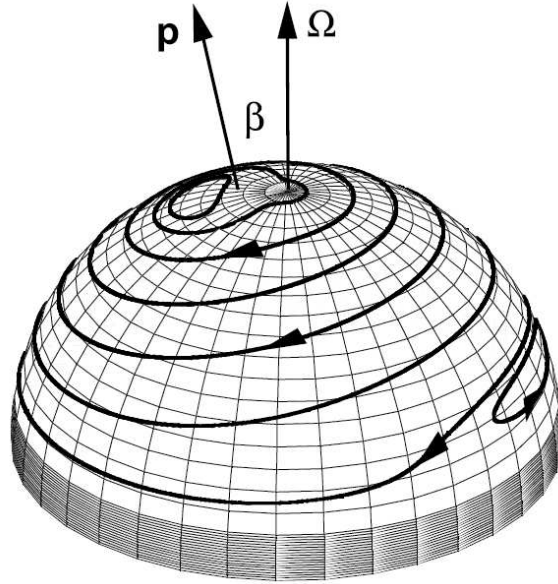


*Figure 3.14: Footpoint trajectories on the source surface for the Fisk-Parker hybrid HMF model. The direction of the footpoint motion is indicated by arrows. The  $p$ -axis is defined by the field line mapped to the source surface from the rotational axis in the lower photosphere. The parameters  $\alpha = 12^\circ$ ,  $\omega = \Omega/4$ ,  $\delta_p = 5.0$  and  $\delta_e = 5.0$  were used. (Taken from Burger et al., 2008)*



From the refined formulae for the footpoint motion, a new expression for the HMF can be derived:

$$\begin{aligned}
 B_r &= B_0 \left( \frac{r_0}{r} \right)^2 & (3.22) \\
 B_\theta &= B_r \frac{r}{u_{\text{sw}}} \omega^* \sin \beta^* \sin \phi^* \\
 B_\phi &= B_r \frac{r}{u_{\text{sw}}} \left( \sin \theta (\omega^* \cos \beta^* - \Omega) + \frac{d}{d\theta} (\omega^* \sin \beta^* \sin \theta) \cos \phi^* \right),
 \end{aligned}$$

with

$$\phi^* = \phi - \Omega t + \frac{\Omega}{u_{\text{sw}}} (r - r_{\text{ss}}) + \phi_0 \quad (3.23)$$

and a solar wind speed  $u_{\text{sw}}$ , which has to be the same for all directions away from the Sun. For  $F_s = 0$  the equations reduce to the standard Parker field, and when  $F_s = 1$  the Fisk field.

The relation between the Fisk angle  $\beta$  and the tilt angle  $\alpha$  is given by

$$\beta = \arccos \left[ 1 - (1 - \cos \theta'_{\text{mm}}) \left( \frac{\sin^2 \alpha}{\sin^2 \theta_{\text{mm}}} \right) \right] - \alpha, \quad (3.24)$$

where  $\theta_{\text{mm}}$  and  $\theta'_{\text{mm}}$  are the maximum extent of the PCH boundaries in heliomagnetic coordinates on the photosphere and the source surface, respectively (Fisk, 1996; Krüger, 2005). In contrast to Fisk (1996), Burger and Hitge (2004) and Burger et al. (2008) assume the polar coronal holes to be symmetric with respect to the solar rotational axis. During solar minimum conditions, the maximum extent of the polar coronal hole on the photosphere in heliographic coordinates is  $\theta_b \approx 30^\circ$  (Waldmeier, 1981; Harvey and Recely, 2002). On the source surface, the PCH reaches down to  $\theta'_b \approx 60^\circ - 80^\circ$  (Munro and Jackson, 1977; Suess et al., 1998). The relations between the heliomagnetic and the heliographic maximum extents of the PCH follow to  $\theta_{\text{mm}} = \theta_b + \alpha$  and  $\theta'_{\text{mm}} = \theta'_b + \alpha$ .

The model of the Fisk-Parker hybrid field during the solar cycle depends on the tilt angle  $\alpha$

$$\alpha = \alpha_{\text{min}} + \left( \frac{\pi}{4} - \frac{\alpha_{\text{min}}}{2} \right) \cdot \begin{cases} 1 - \cos \left( \frac{\pi}{4} T \right) & \text{if } 0 \leq T \leq 4 \\ 1 - \cos \left( \frac{\pi}{7} [T - 11] \right) & \text{if } 4 < T \leq 11 \end{cases} \quad (3.25)$$

with the angles expressed in radians,  $\alpha_{\text{min}} = \pi/18$  and the time  $T$  given in years after solar minimum. This leads to a tilt angle variation between  $\pi/18$  and  $\pi/2$ . The evolution of the polar coronal hole is modelled with the same time dependence

$$\theta_b = \frac{\theta_{\text{b,min}}}{2} \cdot \begin{cases} 1 + \cos \left( \frac{\pi}{4} T \right) & \text{if } 0 \leq T \leq 4 \\ 1 + \cos \left( \frac{\pi}{7} [T - 11] \right) & \text{if } 4 < T \leq 11 \end{cases} \quad (3.26)$$

$$\theta'_b = \frac{\theta'_{\text{b,min}}}{2} \cdot \begin{cases} 1 + \cos \left( \frac{\pi}{4} T \right) & \text{if } 0 \leq T \leq 4 \\ 1 + \cos \left( \frac{\pi}{7} [T - 11] \right) & \text{if } 4 < T \leq 11 \end{cases} \quad (3.27)$$

with  $\theta_{b,\min} = 30^\circ$  and  $\theta'_{b,\min} = 80^\circ$  at solar minimum. The temporal evolution of these parameters is displayed in Fig. 3.15. The Fisk angle  $\beta$  increases during the first years after solar minimum from  $12^\circ$  to  $24^\circ$  and then falls down to  $0^\circ$  at solar maximum. This means that the HMF is described by a standard Parker field during solar maximum.

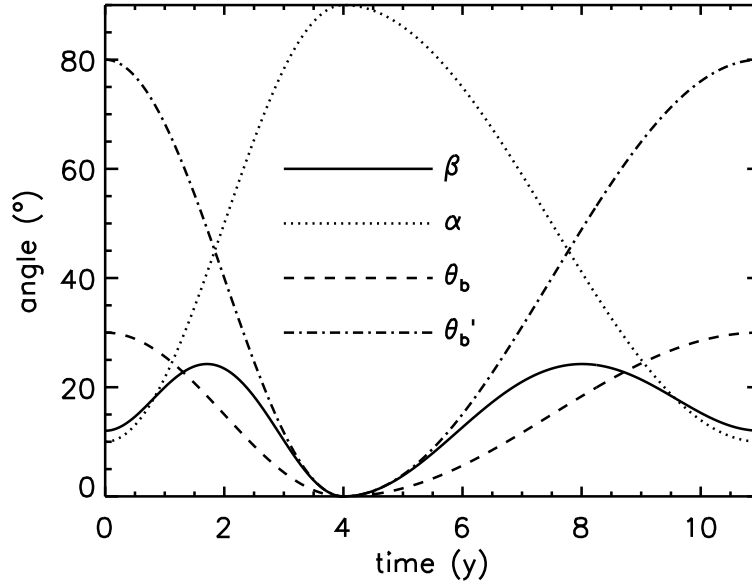


Figure 3.15: The maximum colatitudinal extent  $\theta_b$  of the polar coronal hole on the photosphere and  $\theta'_b$  on the source surface, the tilt angle  $\alpha$  and the Fisk angle  $\beta$  depending on the time after solar minimum. (Adopted from Burger et al., 2008)

Hitge and Burger (2010) (see also Hitge and Burger, 2008) extended the Fisk-Parker hybrid model by Burger and Hitge (2004) and Burger et al. (2008) to a realistic latitudinal profile of the solar wind speed  $u_{\text{sw}}$ . To achieve this, the authors changed the radial component of the HMF the same way Schwadron and McComas (2003) refined the Fisk field. The three components of the Schwadron-Parker hybrid field are then derived to be

$$\begin{aligned}
 B_r &= B_0 \left( \frac{r_0}{r} \right)^2 \left( 1 + \frac{r}{u_{\text{sw}}^2} \omega^* \sin \beta^* \sin \phi^* \frac{du_{\text{sw}}}{d\theta} \right) \\
 B_\theta &= B_r \frac{r}{u_{\text{sw}}} \omega^* \sin \beta^* \sin \phi^* \\
 B_\phi &= B_r \frac{r}{u_{\text{sw}}} \left( \sin \theta (\omega^* \cos \beta^* - \Omega) + \frac{d}{d\theta} (\omega^* \sin \beta^* \sin \theta) \cos \phi^* \right).
 \end{aligned} \tag{3.28}$$

For  $F_s = 0$  these equations reduce to a standard Parker field, if  $du_{\text{sw}}/d\theta = 0$  to the Fisk-Parker hybrid field.

The corresponding field lines of the Fisk-Parker (left panels) and the Schwadron-Parker (right panels) fields are illustrated in Fig. 3.16 to visualise the complex global

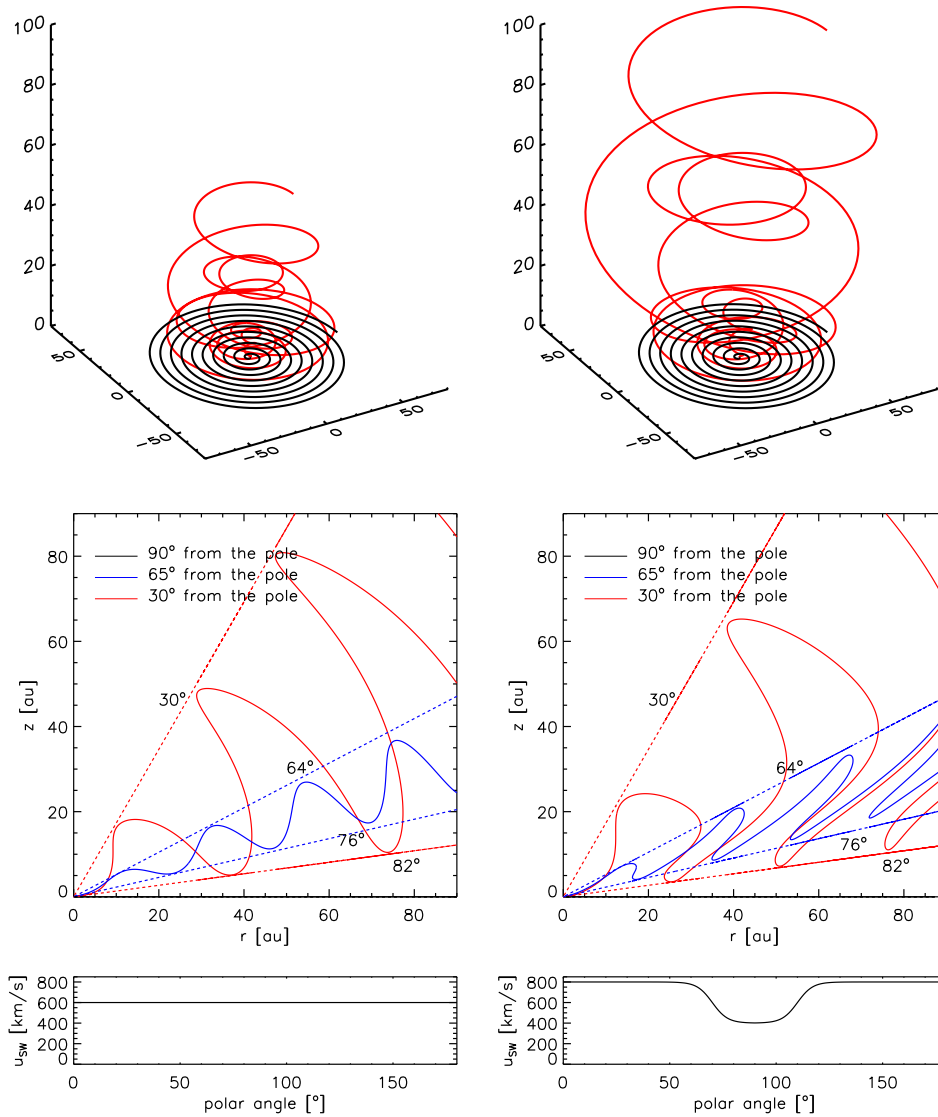


Figure 3.16: Visualisation of the HMF structure in two different projections and the corresponding solar wind speed for the Fisk-Parker hybrid field (left panels) and the Schwadron-Parker hybrid field (right panels). The upper pictures display the 3D structure of two magnetic field lines with different initial colatitudinal positions (red line:  $\theta_0 = 30^\circ$ , black line:  $\theta_0 = 90^\circ$ ). The middle panels present three magnetic field lines in an unwound projection to show the wavy structure of field lines connecting high and low latitudes. The black lines are covered by the abscissa. The dotted lines indicate the latitudinal extension of the corresponding field lines. The lower panels display the solar wind speed employed to calculate the field lines shown above. The parameters  $\theta'_{mm} = 20^\circ$ ,  $\beta = 30^\circ$ ,  $\delta_p = 5$  and  $\delta_e = 4$  were used.

structure of these HMF models. The upper panels show the 3D structure of the magnetic field for two field lines with different initial colatitudinal positions of their footpoints (red line:  $\theta_0 = 30^\circ$ , black line:  $\theta_0 = 90^\circ$  from the solar north pole). In the equatorial region, the HMF is a Parker spiral, while the field structure becomes more complicated in the polar coronal hole. Comparing the Fisk-Parker and Schwadron-Parker model, the high latitude field line reaches further out into the heliosphere in the Schwadron-Parker case due to the more realistic solar wind speed profile implemented in this model. The middle pictures display an unwound projection of three field lines with different initial latitudinal positions of the HMF footpoints. The wavy structure of the mid- and high-latitude field lines magnetically connecting a wide range in latitude becomes evident. The lower panels display the solar wind speed used to calculate the field lines shown in this figure. The field parameters  $\theta'_{\text{mm}} = 20^\circ$ ,  $\beta = 30^\circ$ ,  $\delta_p = 5$  and  $\delta_e = 4$  were chosen.

## Evidence, Advantages and Drawbacks

The Fisk-Parker and Schwadron-Parker field models (Burger and Hitge, 2004; Burger et al., 2008; Hitge and Burger, 2010) solve some open problems of the Fisk field (Fisk, 1996). In these HMF refinements, the PCHs are symmetric with respect to the rotational axis of the Sun on the photosphere. The transfer of the magnetic field footpoints from the polar coronal holes to the return region is modelled by introducing the transition function  $F_s(\theta)$ . In the Schwadron-Parker hybrid HMF, realistic latitudinal profiles of the solar wind speed still lead to a divergence-free expression of the magnetic field vector.

Even though the physics behind Fisk-type fields are widely accepted (Roberts et al., 2007; Burger et al., 2008), the influence of the effects introduced by Fisk and thus the existence of such a complex field structure is still under debate due to the fact that no observational evidence has been found so far in magnetic field measurements. Burger et al. (2008) argue that the azimuthal component of the Parker field is proportional to  $1/u_{\text{sw}}$  so that significant periodicities are expected to be found. However, the analysis of Roberts et al. (2007) suggests that these are not observed. Therefore, Burger et al. (2008) put the possibility to observe the periodicities predicted by the Fisk model in the inner heliosphere into question and explain that the periodicities could be masked by other effects.

If this is true, the only possibility to distinguish the different theories on the HMF in the inner heliosphere is an indirect method. Particle propagation is very sensitive to the HMF model, since the magnetic field influences the motion of charged particles to a large extent. For this reason, simulations of the electron propagation inside the heliosphere and their comparison with spacecraft measurements give the opportunity to contribute to the open question of the global HMF structure via a remote sensing method.

# Chapter 4

## The Propagation of Energetic Particles

Employing balloon flight experiments Hess (1912) measured the intensity of ionising radiation up to an altitude of 5000 m. Since the only known source of this radiation at that time was the Earth, a count rate decreasing with height was expected. However, above 700 m Hess found an increasing count rate with his ionisation chamber. He could exclude the Sun as a radiation source with a balloon flight during a solar eclipse with no change in the measurements. Also the assumption that he had found an electromagnetic radiation was disproven. It was shown that he measured an increasing count rate due to ionising particles: electrons, protons,  $\alpha$  particles and a small fraction of heavier nuclei, which were called cosmic rays (CRs) later. Today different types of cosmic rays are distinguished by their origin:

**Galactic cosmic rays** (GCRs) cover a huge energy range from below keV/nucleon up to above TeV/nucleon. Most probably they are accelerated to these high energies by supernova remnants (Blandford and Ostriker, 1978; Büsching et al., 2005). After entering the heliosphere, they travel through the interplanetary medium and the HMF, where the GCR spectrum is modulated by different physical processes (e.g. Prölss, 2004; Kallenrode, 2004), as explained below.

**Solar energetic particles** (SEPs) are accelerated in solar flares to energies of 1 up to several 100 MeV and show a considerable variability in their spectra, which are still roughly of the same shape. They travel through the interplanetary space and can be detected at Earth (Longair, 1992; Prölss, 2004).

**Anomalous cosmic rays** (ACRs) were found as an irregular component of the cosmic rays with charge states, chemical abundances and energy spectra differing from regular cosmic rays, covering an energy range from 50 – 300 MeV (Prölss, 2004). Until Voyager 1 entered the heliosheath it was commonly believed that secondary solar wind particles are accelerated to ACR energies at the termination shock and then re-enter the heliosphere (Fichtner, 2001). Today numerical

models lend support to the theory that the ACR acceleration process takes place in the inner heliosheath (Ferreira et al., 2007).

**Planetary particles** represent a good tool to study particle propagation inside the heliosphere, as explained below. Especially the Jovian magnetosphere accelerates and releases electrons with energies up to several 10 MeV constantly into the interplanetary space (Pyle and Simpson, 1977; Heber et al., 2007).

This work focuses on electrons of Jovian and galactic origin. For the study of galactic electron propagation, the galactic spectrum is of great importance, since it enters the heliosphere at the outer modulation boundary and is then modulated within the heliosphere. However, because of these modulation effects it is impossible to determine the GCR spectra from measurements inside the heliosphere. Different authors have derived such a spectrum, e.g. Strong et al. (1994), Strong et al. (2000), Langner et al. (2001) or Webber and Higbie (2008). Based on the work by Ferreira et al. (2001a), Ferreira et al. (2001b) and Lange et al. (2006) the galactic electron spectrum from

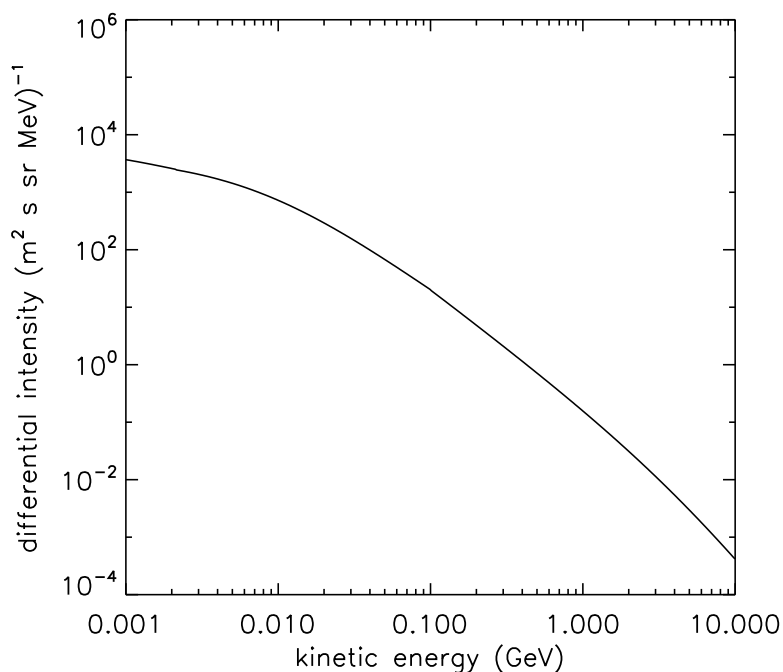


Figure 4.1: The galactic electron spectrum derived by Langner et al. (2001).

Langner et al. (2001) was chosen for the modulation studies presented in chapters 6 and 7. The spectrum is given by

$$j_{\text{LIS}} = \begin{cases} \frac{214.32+3.32 \cdot Y}{1+0.26 \cdot Y+0.02 \cdot Y^2} & \text{if } P < 0.0026 \text{ GV} \\ 1.7 \left[ \frac{52.55+23.01 \cdot X}{1+148.62 \cdot X} \right]^2 & \text{if } 0.0026 \leq P < 0.1 \text{ GV} \\ \frac{1555.89+17.36 \cdot X-3.4 \cdot 10^{-3} \cdot X^2+5.13 \cdot 10^{-7} \cdot X^3}{1.0-11.22 \cdot X+7532.93 \cdot X^2+2405.01 \cdot X^3+103.87 \cdot X^4} & \text{if } 0.1 \leq P < 10.0 \text{ GV} \\ 1.7 \exp[-0.89 - 3.22 \cdot Y] & \text{if } P \geq 10.0 \text{ GV} \end{cases} \quad (4.1)$$

with  $X = P/P_0$ ,  $Y = \ln(P/P_0)$  and  $P_0 = 1 \text{ GV}$  and illustrated in Fig. 4.1.

## The Jovian Magnetosphere as an Electron Source in the inner Heliosphere

McDonald et al. (1972) postulated a particle source of electrons in the MeV range in the vicinity of Jupiter. They based their theory on a 13-months period found in the MeV electron flux measured by spacecraft near Earth. Figure 4.2 shows the electron flux in the energy range from 2 – 12 MeV measured by the IMP-8 spacecraft at the Earth’s orbit from 1974 – 1977. The dashed lines mark the flux maxima occurring with

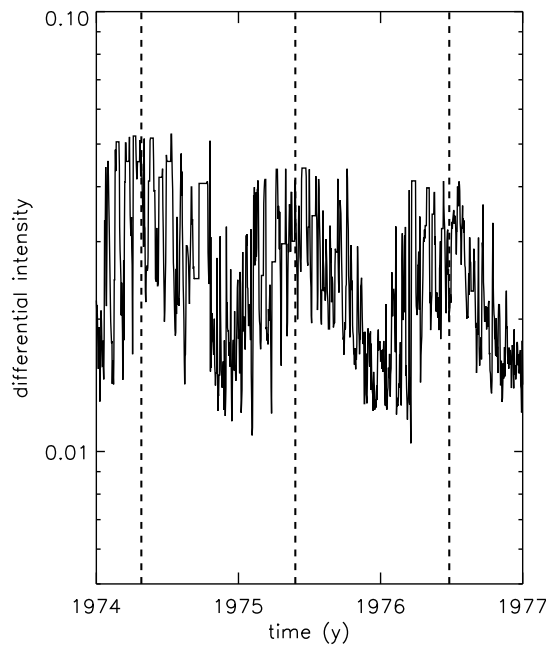


Figure 4.2: The electron flux measured by the IMP-8 spacecraft at the Earth’s orbit for an energy range of 2 – 12 MeV from 1974 – 1977. The dashed lines mark the flux maxima occurring with a period of 13 months.

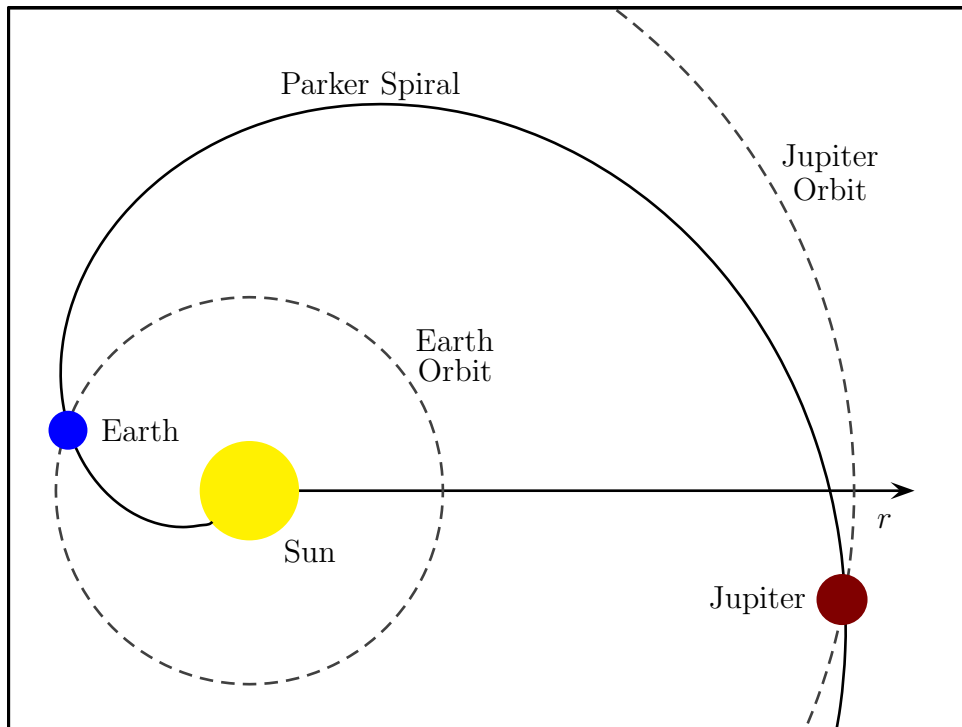


Figure 4.3: The magnetic connection Earth – Jupiter. Due to their orbital times of twelve months and twelve years, respectively, the Earth and Jupiter are magnetically connected by a Parker spiral every 13 months.

a period of 13 months. The reason for the periodic enhancement is the re-occurring magnetic connection of Jupiter and Earth. This situation is shown in Fig. 4.3. The Earth needs 12 months for its orbit around the Sun, while Jupiter's orbit takes about 12 years. Therefore, every 13 months both planets are connected by a Parker spiral, and energetic particles from Jupiter can propagate along the magnetic field line easily and be detected at Earth.

Teegarden et al. (1974) confirmed this assumption and showed that the Jovian magnetosphere is a source of MeV electrons. Figure 4.4 shows Pioneer 10 measurements of the 2 – 7 MeV electron flux (panel b) and the 7 – 17 MeV electron flux (panel c) from 1972 to 1980. The count rate increases while the spacecraft approaches Jupiter and peaks during the fly-by in 1973. After Pioneer 10 has passed the planet, the flux decreases again. These measurements were confirmed by several other spacecraft: Pioneer 11 (1974), Voyager 1 and 2 (1979) and Ulysses (1992). In 2001, a multi-spacecraft measurement of Jovian electrons became possible when both the Galilei and Cassini spacecraft were close to Jupiter (Krupp et al., 2002, 2004).

Further studies of Jovian electrons indicated that particle transport perpendicular to the mean HMF is an important issue in diffusion theories (Chenette et al., 1974; Hamilton and Simpson, 1979). Ferreira et al. (2001a) deduced the Jovian electron



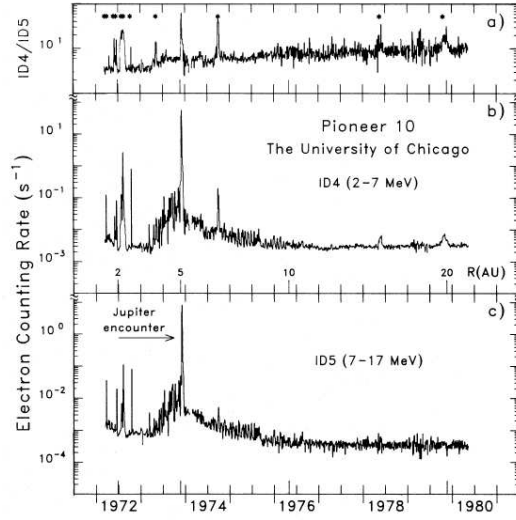


Figure 4.4: Pioneer 10 electron measurements. The graph shows the flux of 2 – 7 MeV electrons (panel b) and 7 – 17 MeV electrons (panel c) from 1972 to 1980. Panel a shows the ratio of both fluxes. Solar particle events are marked with a spot. The electron flux peaks during the Jupiter fly-by of the spacecraft. (Taken from Eraker, 1982)

spectrum to fit the data from ISEE 3 (ICE) (Moses, 1987) and Pioneer 10 (Lopate, 1991):

$$j_{\text{Jovian}} = 1.5 \left( \frac{c_k j_{1.5} d_k j_{6.0}}{c_k j_{1.5} + d_k j_{6.0}} \right) \quad (4.2)$$

with

$$\begin{aligned} j_{1.5} &= 5 \cdot 10^3 \left( \frac{E}{E_0} \right)^{-1.5} \\ j_{6.0} &= 10^9 \left( \frac{E}{E_0} \right)^{-6.0} \\ c_k &= 0.6 \\ d_k &= 5.0 \\ E_0 &= 1 \text{ MeV} \end{aligned}$$

This spectrum is shown in Fig. 4.5 and has been used e.g. by Potgieter and Ferreira (2002), Kissmann et al. (2003, 2004) and Lange et al. (2006). The strength of the source depends on varying heliospheric conditions (McDonald et al., 1972; Teegarden et al., 1974; Morioka et al., 1997).

Jovian electrons play an important role for modulation studies. They emerge almost constantly from a well-known source and are the dominant species in the inner

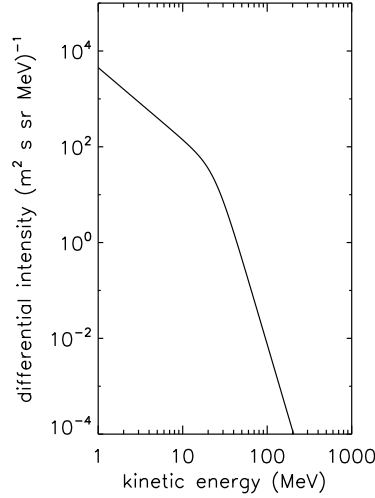


Figure 4.5: The Jovian electron spectrum as derived by Ferreira et al. (2001a).

heliosphere at energies below 10 MeV. The location of their source is known exactly and non-central with respect to the HMF, so Jovian electrons can be used to study perpendicular transport. An advantage especially for numerical models can be found in the size of the Jovian magnetosphere. It is small in comparison with the heliosphere and can therefore be treated as a point source. On the other hand, the galactic electron spectrum is not clearly identified and still under discussion. Also, the heliospheric boundary, where the galactic spectrum is expected to be found, is not defined accurately. Therefore, Jovian electrons are almost ideal particles to test diffusion theories and set limits on the diffusion tensor.

## Parker's Transport Equation

The propagation of cosmic rays within the heliosphere is described by a transport equation (TPE). It was first proposed by Parker (1965) and is discussed in detail e.g. by Potgieter (1998):

$$\frac{\partial f}{\partial t} = \underbrace{\vec{\nabla} \cdot (\hat{\kappa} \cdot \vec{\nabla} f)}_{\text{diffusion}} - \underbrace{(\vec{u}_{\text{sw}} + \vec{v}_{\text{D}}) \cdot \vec{\nabla} f}_{\text{convection \& drift}} + \underbrace{\frac{1}{3} (\vec{\nabla} \cdot \vec{u}_{\text{sw}})}_{\text{adiabatic energy changes}} \frac{\partial f}{\partial (\ln P)} + \underbrace{S}_{\text{sources}} \quad (4.3)$$

Parker's TPE describes the temporal evolution of the pitch-angle isotropic differential cosmic ray distribution function  $f(\vec{r}, P, t)$  depending on the position  $\vec{r}$  in the heliosphere, the particle rigidity  $P$  and the time  $t$ . It takes into account four basic physical processes influencing the particles' distribution function: the convection with

the solar wind speed  $\vec{u}_{\text{sw}}$ , particle drifts with the drift velocity  $\vec{v}_{\text{D}}$ , diffusion described by the diffusion tensor  $\hat{\kappa}$  and adiabatic energy changes. All these physical processes are discussed below. Particle sources and sinks are included in the TPE by the term  $S$ . The measurable differential particle intensity  $j$  can be calculated from the distribution function:

$$j = fP^2 \quad (4.4)$$

## Convection with the Solar Wind

Energetic particles moving through the heliosphere are influenced by the solar wind and convected outwards. As described in chapter 2, the solar wind properties change considerably during the solar cycle (Fig. 2.4). To describe the influence of the SW in a model, a simplified description of the solar wind speed, especially of its temporal evolution, is needed. Two possible expressions for  $u_{\text{sw}}$  are explained in the following (Lange, 2004). The solar wind speed is split into two parts:

$$u_{\text{sw}}(r, \theta, t) = u_1(r) \cdot u_2(\theta, t). \quad (4.5)$$

The radial dependence is given by the function

$$u_1(r) = 1 - \exp \left\{ \frac{40}{3} \left( \frac{R_s - r}{r_0} \right) \right\} \quad (4.6)$$

with the solar radius,  $R_s$ , and  $r_0 = 1$  AU. Here, two possible models describing the time dependence of the latitudinal profile are presented.

$$u_2(\theta, t) = \begin{cases} u_{\min} + \frac{1}{2}u_a h_1(t) \{1 - \tanh[\frac{1}{\Delta\theta}(\theta - \frac{\pi}{2} + \theta_s)]\} & \text{if } \theta \leq \frac{\pi}{2} \\ u_{\min} + \frac{1}{2}u_a h_1(t) \{1 + \tanh[\frac{1}{\Delta\theta}(\theta - \frac{\pi}{2} - \theta_s)]\} & \text{if } \theta > \frac{\pi}{2} \end{cases} \quad (4.7)$$

with  $u_a = 0.5(u_{\max} - u_{\min})$ , a constant polar coronal hole boundary latitude  $\theta_s = \pi/9$  ( $\hat{=}$   $20^\circ$ ), the width of the transition region from slow to fast SW  $\Delta\theta = 0.125$  ( $\hat{=}$   $7^\circ$ ), a maximum SW speed  $u_{\max} = 800$  km/s, a minimum SW speed  $u_{\min} = 400$  km/s and the time-dependent function

$$h_1(t) = \begin{cases} 1 - \tanh\{g(t_0 - t)\} & \text{maximum to minimum} \\ 1 - \tanh\{g(t - t_0)\} & \text{minimum to maximum.} \end{cases} \quad (4.8)$$

Here,  $g$  determines the transition time-scale and  $t_0$  is the time around which the transition is centered. This first model is displayed in the left panel of Fig. 4.6. The PCH boundary is fixed during the whole solar cycle. The SW speed rises uniformly inside the PCH from 400 km/s to 800 km/s during the transition from solar maximum to solar minimum.

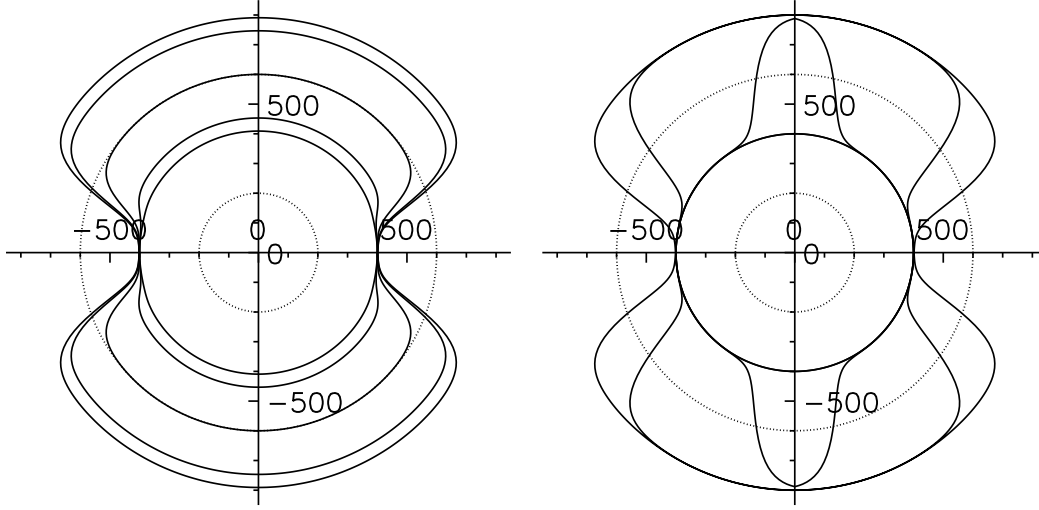


Figure 4.6: The time evolution of the latitudinal solar wind speed profile. The illustration shows five latitudinal SW speed profiles during the transition from solar maximum to solar minimum equally spaced in time in units of km/s for the first model (left panel) and the second model (right panel). The abscissa represents the equatorial plane, while the ordinate stand for the polar direction. Additionally, two dotted lines are plotted to guide the eye at 200 km/s and 600 km/s, respectively. For the second model only four lines are visible, because there is only little change from the first to the second time step. (Adopted from Lange, 2004)

The second model is given by

$$u_2(\theta, t) = \begin{cases} u_{\min} + u_a \left\{ 1 - \tanh \left[ \frac{1}{\Delta\theta} \left( \theta - \frac{\pi}{2} + \theta_s(t) \right) \right] \right\} & \text{if } \theta \leq \frac{\pi}{2} \\ u_{\min} + u_a \left\{ 1 + \tanh \left[ \frac{1}{\Delta\theta} \left( \theta - \frac{\pi}{2} - \theta_s(t) \right) \right] \right\} & \text{if } \theta > \frac{\pi}{2} \end{cases} \quad (4.9)$$

where the PCH boundary latitude is computed with the time-dependent function

$$\theta_s(t) = \begin{cases} \frac{20}{180}\pi + \frac{23}{72}\pi (1 - \tanh \{g(t - t_0)\}) & \text{maximum to minimum} \\ \frac{20}{180}\pi + \frac{23}{72}\pi (1 - \tanh \{g(t_0 - t)\}) & \text{minimum to maximum.} \end{cases} \quad (4.10)$$

Note that to achieve solar maximum conditions in this model,  $\theta_s$  has to be increased up to  $135^\circ$  to ensure that the solar wind speed reaches a value of 400 km/s at all latitudes. The time evolution of the SW speed according to the second model is shown in the right panel of Fig. 4.6. In contrast to the other model,  $\theta_s$  is not fixed but varies in time. The PCH opens at high latitudes and expands during the transition from solar maximum to solar minimum with a SW speed of 800 km/s inside the PCH.

## Adiabatic Energy Changes

The expansion of the SW and the outwardly decreasing magnetic field strength of the HMF lead to adiabatic energy changes influencing the particles' distribution function.

The effect of the expanding SW can be understood assuming a Parker spiral in the outer heliosphere, where the magnetic field lines are almost circular, as illustrated in the sketch in Fig. 4.7. A charged particle gyrates around and moves along the magnetic field line between two scattering centers where it is scattered back elastically. A resting observer between the two scattering centers sees the scattering centers moving away with  $v_{sc}$  due to the expansion of the solar wind. In the scattering center's rest frame, the particle moves along the field line with  $v_{\parallel}^{(1)}$  before the scattering process. The transformation from the scattering center's rest frame to the observer's rest frame is a simple Galilei transformation:

$$v \longrightarrow v' = v + v_{sc} \quad (4.11)$$

Therefore, the parallel speed in the observer's rest frame prior to the scattering becomes  $v_{\parallel}^{(1)'} = v_{\parallel}^{(1)} + v_{sc}$ . After the scattering, the parallel speed is given by

$$v_{\parallel}^{(1)} \longrightarrow v_{\parallel}^{(2)} = -v_{\parallel}^{(1)} \quad (4.12)$$

due to the assumption of elastic scattering. In the observer's rest frame the particle speed transforms to

$$v_{\parallel}^{(2)'} = -v_{\parallel}^{(1)} + v_{sc} = -(v_{\parallel}^{(1)} - v_{sc}). \quad (4.13)$$

In this simplified situation, each scattering process reduces the parallel particle speed in the observer's rest frame by  $\Delta v = 2 \cdot v_{sc}$  and, therefore, leads to a loss of energy.

The outwardly decreasing HMF strength leads to a focusing of the particle speed with respect to the magnetic field line. Here, we assume a particle to be convected

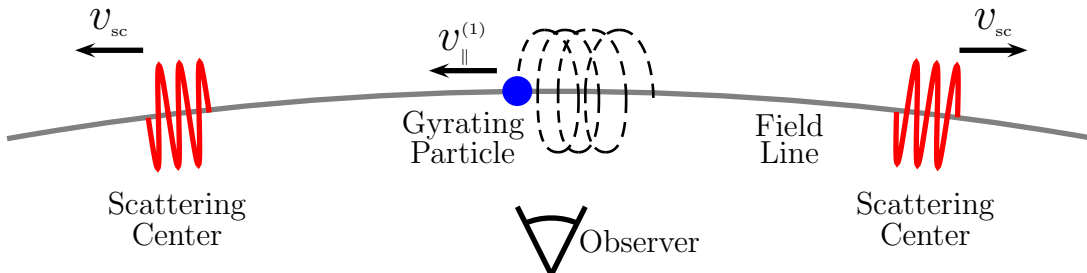


Figure 4.7: Adiabatic energy losses due to solar wind expansion. A particle moving along a magnetic field line between two scattering centers is scattered elastically. Each scattering process leads to a reduction of the parallel particle speed in the observer's rest frame and, therefore, to a loss of energy.

outwards with the solar wind. The particle velocity can be described by a part  $v_{\parallel}$  parallel and a part  $v_{\perp}$  perpendicular to the magnetic field. A particle moving outwards with the solar wind sees magnetic field strength decreasing with time in the particle's rest frame. From Maxwell's equations follows that a magnetic field varying in time induces an electric field which can change the particle's energy. If the changes of the magnetic field strength are slow compared to the gyration motion of the particle, the magnetic moment  $\mu = mv_{\perp}^2/2B$  is invariant and a decreasing magnetic field  $B$  leads to a decreasing perpendicular particle speed  $v_{\perp}$ . However, in the observer's rest frame the magnetic field does not change with time and the particle's energy has to be conserved, so a decreasing  $v_{\perp}$  leads to a higher parallel particle speed  $v_{\parallel}$ . The particle motion focuses with respect to the magnetic field line. The consequence of this effect is an energy loss in the particle's rest frame.

The assumed simplifications can be generalised and both the influence of the expanding SW and the decreasing magnetic field contribute to the adiabatic cooling or adiabatic deceleration. A more detailed study can be found in Webb and Gleeson (1979).

## Particle Diffusion and Drift

The motion of charged particles through electromagnetic fields is determined by the Lorentz force

$$\vec{F}_L = q \left( \vec{E} + \vec{v} \times \vec{B} \right). \quad (4.14)$$

Because of the high conductivity of the heliospheric plasma, electric fields are of no importance to energetic charged particles moving through the heliosphere. The motion of these particles in magnetic fields can be divided into two components: one along the magnetic field line with the velocity  $v_{\parallel}$  and a gyration around the magnetic field line with the velocity  $v_{\perp}$ . For a characterisation of a particle's trajectory through the interplanetary space it is of great importance that the HMF is only a smooth Parker spiral averaged over time. On short time scales the field has a complex structure with strong temporal and spatial variations influencing the particle transport due to particle scattering at inhomogeneities of the magnetic field. These perturbations of the magnetic field are of a statistical nature leading to statistical variations in a particle's trajectory.

Particles propagating through the heliosphere are scattered frequently. During this process the particles' pitch-angle distribution becomes isotropic, because the magnetic field inhomogeneities have no preferred angle (Jokipii, 1966). Therefore, at most points in the heliosphere particles move in all directions with the same speed. A particle density which is at one point in the heliosphere higher than at its neighbouring point leads to a particle flux balancing the density again. This results in a spatial diffusion of the particles (Jokipii, 1966). The particle scattering and pitch-angle isotropisation

occur much faster than the diffusion time scales, so the assumption of an isotropic pitch-angle distribution function is justified on a global scale (Schlickeiser, 1989).

Similar to the particle speed, it is also reasonable to distinguish between diffusive transport parallel and perpendicular to the magnetic field. It is determined by the mean free path  $\lambda$ , the distance a particle can propagate undisturbed before being scattered. For the parallel diffusion this relation is given by

$$\lambda_{\parallel} = \frac{3\kappa_{\parallel}}{v} \quad (4.15)$$

with the parallel mean free path,  $\lambda_{\parallel}$ , the parallel diffusion coefficient,  $\kappa_{\parallel}$  and the particle speed,  $v$ . The calculation of the mean free path and the diffusion coefficients is a complex field of research. The first approach was made by applying quasi-linear theory (Jokipii, 1966). However, a comparison with measured data from solar flares pointed out that this assumption was not sufficient. There is still no adequate theory available, because the HMF fluctuations are not known exactly. Other approaches include the treatment of HMF fluctuations as turbulence caused by plasma waves (Schlickeiser, 2002) or the nonlinear guiding center theory (Shalchi et al., 2004; Shalchi, 2009).

Curvature, gradients and inhomogeneities of the magnetic field lead to drift motions which can be summarised in the drift speed

$$\vec{v}_D = \vec{\nabla} \times (\kappa_A \vec{e}_B) \quad (4.16)$$

with the drift coefficients  $\kappa_A$  and  $\vec{e}_B = \vec{B}/B$  (Hattingh, 1998; Ferreira, 2002). With the help of this correlation, Parker's TPE can be re-written as

$$\frac{\partial f}{\partial t} = \underbrace{\vec{\nabla} \cdot (\hat{\kappa}' \cdot \vec{\nabla} f)}_{\text{diffusion \& drift}} - \underbrace{\vec{u}_{\text{sw}} \cdot \vec{\nabla} f}_{\text{convection}} + \underbrace{\frac{1}{3} (\vec{\nabla} \cdot \vec{u}_{\text{sw}})}_{\text{adiabatic energy changes}} \frac{\partial f}{\partial (\ln P)} + \underbrace{S}_{\text{sources}} \quad (4.17)$$

with the diffusion tensor

$$\hat{\kappa}' = \begin{pmatrix} \kappa_{\parallel} & 0 & 0 \\ 0 & \kappa_{\perp r} & \kappa_A \\ 0 & -\kappa_A & \kappa_{\perp \theta} \end{pmatrix} \quad (4.18)$$

in a coordinate system aligned to the magnetic field. The three diagonal coefficients  $\kappa_{\parallel}$ ,  $\kappa_{\perp r}$  and  $\kappa_{\perp \theta}$  represent the diffusion parallel to the magnetic field, perpendicular in radial direction and perpendicular in latitudinal direction, respectively. The diffusion and drift coefficients are explained below.

## Parallel Diffusion

This work employs a parallel diffusion coefficient similar to Ferreira et al. (2003b):

$$\kappa_{\parallel} = \kappa_0 \beta f_1(r, P) f_2(t) \quad (4.19)$$

Here,  $\beta$  denotes the ratio of the particle speed and the speed of light  $v/c$  and  $\kappa_0 = 4.5 \cdot 10^{18} \text{ m}^2\text{s}^{-1}$ . The spatial and energy dependences are taken from Ferreira et al. (2001a):

$$\begin{aligned}
 f_1(r, P) &= 0.2 g(P) c(r) h(P, r) & (4.20) \\
 g(P) &= \left(\frac{P_0}{P_s}\right)^{0.6} \\
 P_s &= \begin{cases} P & \text{if } P < 1 \text{ GV} \\ 1 \text{ GV} & \text{if } P \geq 1 \text{ GV} \end{cases} \\
 c(r) &= \begin{cases} 1 & \text{if } r > r_c \\ m(r) & \text{if } r \leq r_c \end{cases} \\
 m(r) &= \xi \frac{r_0}{r_c} \left(\frac{r}{r_0}\right)^\xi \\
 \xi &= \left(\frac{r}{r_c}\right)^x \\
 x &= \left(\frac{0.016}{P/P_0}\right)^{0.2} \\
 r_c &= \frac{r_0}{0.1 + (P_s/P_0)^{1.4}} \\
 h(P, r) &= 0.02 \left(\frac{P}{P_0}\right)^{2.0} \left(\frac{r}{r_0}\right)^{1.7} + 0.02 \left(\frac{P}{P_0}\right) \left(\frac{r}{r_0}\right)^{2.2} \\
 &\quad + 0.2 \left(\frac{P}{P_0}\right)^{\frac{1}{3}} \left(\frac{r}{r_0}\right) + 7.0e(r) \\
 e(r) &= \begin{cases} \left(\frac{10r_0}{r}\right)^k & \text{if } r > 10 \text{ AU} \\ 1 & \text{if } r \leq 10 \text{ AU} \end{cases} \\
 k &= 0.000125 \left(\frac{r}{r_0}\right)^2
 \end{aligned}$$

with  $P_0 = 1 \text{ GV}$  and  $r_0 = 1 \text{ AU}$ . The time dependence of  $\kappa_{\parallel}$  is chosen to

$$f_2(t) = \left(\frac{B_0}{B(t)}\right)^n \quad (4.21)$$

with  $B_0 = 5 \text{ nT}$  and an energy dependent exponent  $n$ . For 7 MeV electrons negative values of  $n$  are chosen (Engelbrecht, 2009; Engelbrecht and Burger, 2010). In this approach the measured magnetic field strength at Earth  $B(t)$  is used as a measure for the overall magnetic turbulence in the heliosphere (Ferreira et al., 2003b). Note that Ferreira et al. (2003b) use an additional factor  $\sigma(t)$  in  $f_2(t)$  depending on the 22-year solar magnetic cycle which is not applied in our model. The energy dependence of the parallel mean free path is illustrated in Fig. 4.8 for  $f_2(t) = 1$  at different distances to the Sun.



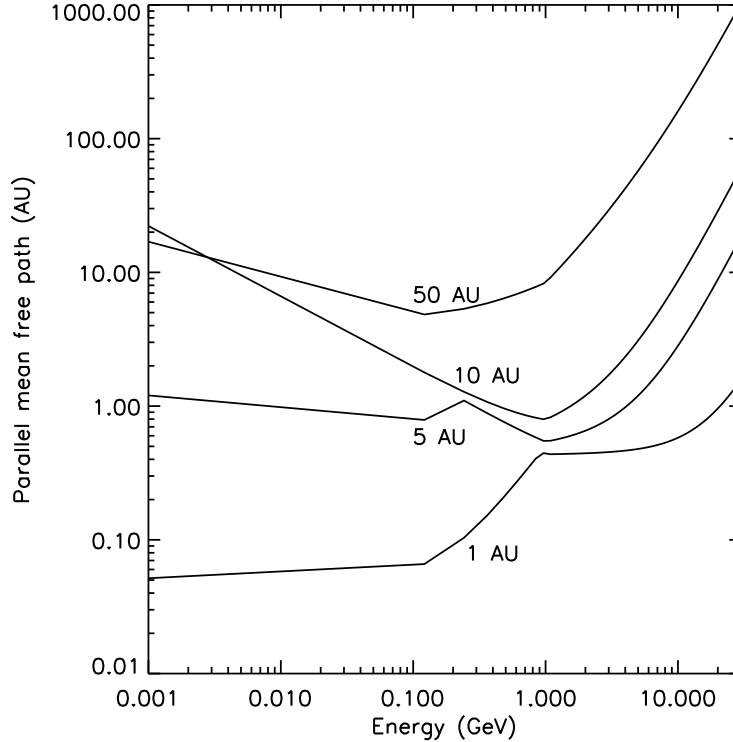


Figure 4.8: The parallel mean free path depending on the particle energy. The graph illustrates  $\lambda_{\parallel}$  at distances of 1 AU, 5 AU, 10 AU and 50 AU from the Sun as computed from equations (4.19) to (4.21) for  $f_2(t) = 1$ .

## Perpendicular Diffusion

Particle scattering perpendicular to the magnetic field occurs due to two basic factors: a displacement of the particle's gyrocenters transverse to the mean magnetic field because of scattering and a random walk of the magnetic field lines themselves. Since perpendicular diffusion is a very complex topic, theoretical work was commonly neglected for a long time (Jokipii, 2001), although it was shown that perpendicular transport is a very important issue (Chenette et al., 1974; Hamilton and Simpson, 1979; Ferreira et al., 2000). Therefore, no exact theory is available until now, but see recent advances by Matthaeus et al. (2003), Shalchi et al. (2004), Zank et al. (2004) or Shalchi (2009). In modulation models it has become standard practice to scale  $\kappa_{\perp}$  to  $\kappa_{\parallel}$  (Jokipii and Kóta, 1995; Potgieter, 1996; Ferreira et al., 2000; Burger et al., 2000; Ferreira et al., 2001a; Ferreira et al., 2001b, 2003b).

Supporting this assumption, Giacalone (1998) found  $\kappa_{\perp}/\kappa_{\parallel} = 0.02 - 0.03$  for rigidities of 40 MV to 2 GV, while Giacalone and Jokipii (1999) derived  $\kappa_{\perp}/\kappa_{\parallel} = 0.02 - 0.04$  for rigidities of 40 MV to 1.7 GV without distinguishing between  $\kappa_{\perp r}$  and  $\kappa_{\perp \theta}$ . Analysing the propagation of low-energy Jovian electrons, Ferrando (1997) found

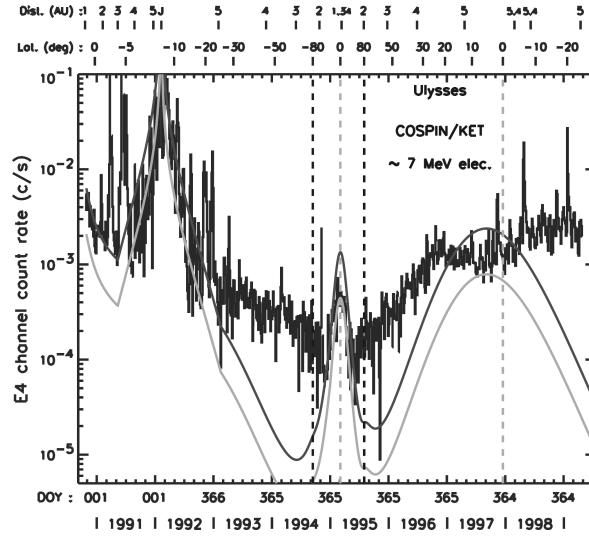


Figure 4.9: Model results for 7 MeV electrons of Jovian origin along the Ulysses trajectory. This figure shows two different model results and compares them to Ulysses observations. Both lines do not fit the measured electron data. Therefore, from these results it was concluded that classical models with  $\kappa_{\perp r} = \kappa_{\perp \theta}$  are not sufficient, so that anisotropic perpendicular diffusion is needed. (Taken from Ferrando, 1999)

$\kappa_{\perp r}/\kappa_{\parallel} = 0.005$  and  $\kappa_{\perp \theta}/\kappa_{\parallel} = 0.001$  at an energy of  $\sim 7$  MeV in the equatorial region of the heliosphere. Based on these results, the perpendicular diffusion coefficients can be given as

$$\begin{aligned}\kappa_{\perp r} &= a \cdot \kappa_{\parallel} \\ \kappa_{\perp \theta} &= b \cdot \kappa_{\parallel}\end{aligned}\tag{4.22}$$

where  $a$  and  $b$  can be constants or functions of rigidity (Ferreira, 2002).

Observations with the Ulysses spacecraft revealed that the latitudinal dependence of the CR proton flux at low energies is significantly lower than predicted with classical models (Potgieter and Haasbroek, 1993; Heber et al., 1996). Similar results were found by Ferrando (1999) comparing the 7 MeV electron flux measured by Ulysses to model results with  $\kappa_{\perp r} = \kappa_{\perp \theta}$ , as shown in Fig. 4.9.

These surprising results supported the idea of anisotropic perpendicular diffusion with  $\kappa_{\perp \theta} > \kappa_{\perp r}$  (Kóta and Jokipii, 1995b, 1997; Ferreira et al., 2001a). This new concept lead to more realistic results for latitudinal gradients in the particle flux and could explain CIR related particle events measured by Ulysses at high latitudes (Jokipii et al., 1995; Kóta and Jokipii, 1998). Ferreira et al. (2001a,b) suggest

$$\begin{aligned}\kappa_{\perp r} &= 0.02 \left( \frac{P}{P_0} \right)^{0.3} \kappa_{\parallel} \\ \kappa_{\perp \theta} &= 0.015 \kappa_{\parallel} F(\theta, t)\end{aligned}\tag{4.23}$$

for the perpendicular diffusion coefficients with  $P_0 = 1$  GV. Ferreira et al. (2001a) assume an enhancement of the latitudinal diffusion in the PCH during solar minimum conditions which can be motivated by two different effects: the Ulysses spacecraft measured an increased turbulence in the fast solar wind with an enhancement being higher in the transverse direction than in the radial direction (Jokipii et al., 1995) leading to a higher  $\kappa_{\perp\theta}$ . The other possibility is a Fisk-type HMF structure with magnetic field lines connecting a wide latitudinal range, as shown in chapter 3. This is applied to the diffusion coefficient  $\kappa_{\perp\theta}$  with the time-dependent function  $F(\theta, t)$  describing its temporal evolution during the solar cycle. Two models for  $F(\theta, t)$  can be found, similar to the time evolution of the latitudinal solar wind speed profile. The first model

$$F(\theta, t) = \begin{cases} \frac{d(t)+1}{2} + \frac{d(t)-1}{2} \tanh \left\{ \frac{1}{\Delta\theta} \left( -\theta + \frac{\pi}{2} - \theta_s \right) \right\} & \text{if } \theta \leq \frac{\pi}{2} \\ \frac{d(t)+1}{2} + \frac{d(t)-1}{2} \tanh \left\{ \frac{1}{\Delta\theta} \left( \theta - \frac{\pi}{2} - \theta_s \right) \right\} & \text{if } \theta > \frac{\pi}{2} \end{cases} \quad (4.24)$$

fixes the PCH boundary latitude  $\theta_s = \pi/9$  ( $\hat{=}$   $20^\circ$ ).  $\Delta\theta = 0.125$  ( $\hat{=}$   $7^\circ$ ) denotes the width of the transition region at the PCH boundary. The time-dependent function  $d(t)$  is given by

$$d(t) = v - h_2(t) \frac{v-1}{2} \quad (4.25)$$

with the maximum enhancement  $v \approx 6 - 10$  and

$$h_2(t) = \begin{cases} 1 - \tanh \{g(t - t_0)\} & \text{maximum to minimum} \\ 1 - \tanh \{g(t_0 - t)\} & \text{minimum to maximum} \end{cases} \quad (4.26)$$

with  $g$  determining the transition speed and the time  $t_0$  on which the transition is centered. The PCH boundary is fixed and  $\kappa_{\perp\theta}$  is increased in the whole PCH uniformly during the transition from solar maximum to solar minimum conditions. The second possibility

$$F(\theta, t) = \begin{cases} \frac{v+1}{2} + \frac{v-1}{2} \tanh \left\{ \frac{1}{\Delta\theta} \left[ -\theta + \frac{\pi}{2} - \theta_s(t) \right] \right\} & \text{if } \theta \leq \frac{\pi}{2} \\ \frac{v+1}{2} + \frac{v-1}{2} \tanh \left\{ \frac{1}{\Delta\theta} \left[ \theta - \frac{\pi}{2} - \theta_s(t) \right] \right\} & \text{if } \theta > \frac{\pi}{2} \end{cases} \quad (4.27)$$

treats the PCH boundary latitude as a time-dependent function

$$\theta_s(t) = \begin{cases} \frac{20}{180}\pi + \frac{23}{72}\pi (1 - \tanh \{g(t - t_0)\}) & \text{maximum to minimum} \\ \frac{20}{180}\pi + \frac{23}{72}\pi (1 - \tanh \{g(t_0 - t)\}) & \text{minimum to maximum} \end{cases} \quad (4.28)$$

and increases the PCH during the transition from solar maximum to solar minimum. The time development is the same as was already used for the solar wind speed. Therefore, an additional illustration is not given.

## Particle Drift

Although it is part of Parker's TPE, drifts were widely neglected until Jokipii et al. (1977) showed that drift motions play a major role for modulation studies. They are caused by curvatures and gradients of the magnetic field and neutral current sheets. Ferreira et al. (2003a,b) underline the sensitivity of drift motions to the polarity of the HMF which underlies a 22-year cycle and to the particle charge sign. Ferreira (2002) showed, however, that particle drifts are negligible for electrons with energies below 10 MeV by comparing model data from an  $A^+$  and an  $A^-$  solar cycle finding no difference in the resulting particle spectra in this energy range. Since the aim of this work is the investigation of 7 MeV electrons, drifts are neglected and  $\kappa_A = 0$  is chosen.

## A Comparison of the Diffusion Tensor in different HMF Configurations

A first insight into the influence of different HMF models on the latitudinal particle transport can be obtained with a comparison of the latitude dependence of the diffusion tensor in different HMF configurations. For the purpose of this work it is especially useful to investigate  $\hat{\kappa}$  for an energy of 7 MeV and a distance of 5 AU from the Sun, which are typical values for Jovian electrons. This study is similar to Sternal et al. (2008), but with a different transition function for the Fisk-type fields.

For further calculations, especially for numerical models with a spherical computational domain, the diffusion tensor is transformed from the magnetic field aligned coordinate system to spherical polar coordinates:

$$\hat{\kappa}' = \begin{pmatrix} \kappa_{\parallel} & 0 & 0 \\ 0 & \kappa_{\perp r} & \kappa_A \\ 0 & -\kappa_A & \kappa_{\perp \theta} \end{pmatrix} \longrightarrow \hat{\kappa}'_{\text{sphere}} = \begin{pmatrix} \kappa_{rr} & \kappa_{r\theta} & \kappa_{r\phi} \\ \kappa_{\theta r} & \kappa_{\theta\theta} & \kappa_{\theta\phi} \\ \kappa_{\phi r} & \kappa_{\phi\theta} & \kappa_{\phi\phi} \end{pmatrix} \quad (4.29)$$

The conversion is given by Burger et al. (2008):

$$\begin{aligned} \kappa_{rr} &= \kappa_{\perp\theta} \sin^2 \zeta + \cos^2 \zeta (\kappa_{\parallel} \cos^2 \psi + \kappa_{\perp r} \sin^2 \psi) \\ \kappa_{r\theta} &= -\kappa_A \sin \psi + \sin \zeta \cos \zeta (\kappa_{\parallel} \cos^2 \psi + \kappa_{\perp r} \sin^2 \psi - \kappa_{\perp\theta}) \\ \kappa_{r\phi} &= -\kappa_A \cos \psi \sin \zeta - (\kappa_{\parallel} - \kappa_{\perp r}) \sin \psi \cos \psi \cos \zeta \\ \kappa_{\theta r} &= \kappa_A \sin \psi + \sin \zeta \cos \zeta (\kappa_{\parallel} \cos^2 \psi + \kappa_{\perp r} \sin^2 \psi - \kappa_{\perp\theta}) \\ \kappa_{\theta\theta} &= \kappa_{\perp\theta} \cos^2 \zeta + \sin^2 \zeta (\kappa_{\parallel} \cos^2 \psi + \kappa_{\perp r} \sin^2 \psi) \\ \kappa_{\theta\phi} &= \kappa_A \cos \psi \cos \zeta - (\kappa_{\parallel} - \kappa_{\perp r}) \sin \psi \cos \psi \sin \zeta \\ \kappa_{\phi r} &= \kappa_A \cos \psi \sin \zeta - (\kappa_{\parallel} - \kappa_{\perp r}) \sin \psi \cos \psi \cos \zeta \\ \kappa_{\phi\theta} &= -\kappa_A \cos \psi \cos \zeta - (\kappa_{\parallel} - \kappa_{\perp r}) \sin \psi \cos \psi \sin \zeta \\ \kappa_{\phi\phi} &= \kappa_{\parallel} \sin^2 \psi + \kappa_{\perp r} \cos^2 \psi \end{aligned} \quad (4.30)$$

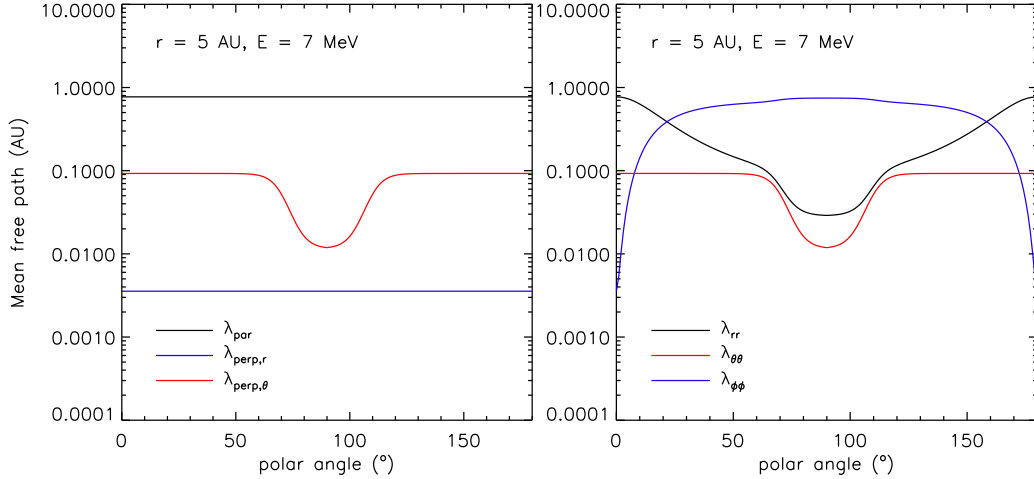


Figure 4.10: The latitudinal dependence of the particle mean free path in a Parker HMF for 7 MeV electrons at 5 AU.

with

$$\tan \psi = -\frac{B_\phi}{\sqrt{B_r^2 + B_\theta^2}} \quad \text{and} \quad \tan \zeta = \frac{B_\theta}{B_r} \quad (4.31)$$

Note that Kobylinski (2001) derived the same formulae but with  $\tan \psi = -B_\phi/B_r$ , and that  $\kappa_A = 0$ , since no drift effects are applied in this work.

Figure 4.10 illustrates the mean free path as a function of heliographic latitude with the solar north- and south pole located at  $0^\circ$  and  $180^\circ$ , respectively. The HMF configuration is a Parker field during solar minimum conditions with a SW speed of 400 km/s in the equatorial region and 800 km/s at latitudes  $> 20^\circ$  north and south of the solar equator. The left panel shows the mean free path in magnetic field aligned coordinates. The graph shows that  $\lambda_{\parallel}$  (black line) and  $\lambda_{\perp r}$  (blue line) do not depend on latitude, while  $\lambda_{\perp \theta}$  (red line) reflects the enhancement of the latitudinal diffusion by the function  $F(\theta)$  with a factor of 8 inside the PCH. The right panel displays the mean free path after the transformation to spherical polar coordinates. The coefficients for the radial and longitudinal mean free path  $\lambda_{rr}$  (black line) and  $\lambda_{\phi\phi}$  (blue line), respectively, show the influence of the magnetic field structure, while there is no additional change in the latitudinal mean free path  $\lambda_{\theta\theta}$  (red line) by the HMF configuration.

For the hybrid field study, the same parallel diffusion coefficient is applied, but with isotropic perpendicular diffusion, i.e.  $\kappa_{\perp r} = \kappa_{\perp \theta}$ , being aware of the fact that the ratio of  $\kappa_{\perp r}$  and  $\kappa_{\perp \theta}$  to  $\kappa_{\parallel}$  will have to be adjusted for modulation studies. At high latitudes, no enhancement of  $\kappa_{\perp \theta}$  due to turbulence is taken into account to discuss only the influence of the field structure. A frame corotating with the Sun is chosen for the illustrations. The HMF parameters  $\theta'_b = 80^\circ$  and  $\delta_p = \delta_e = 5$  are used in this study (Burger et al., 2008).

In Fig. 4.11 the particle mean free path is given for the Fisk-Parker hybrid HMF. The colour coding and the parameters are the same as in Fig. 4.10. Since the Fisk-Parker hybrid field is computed with an isotropic SW speed, the mean free path is presented for three different values of  $u_{\text{SW}}$ : 400 km/s (solid line), 600 km/s (dashed line) and 800 km/s (dash-dotted line). The upper left panel shows the particle mean free path in magnetic field aligned coordinates, while the other ten panels illustrate the longitudinal dependence of the mean free path in spherical polar coordinates for different longitudes from  $\phi = 0^\circ$  to  $\phi = 180^\circ$ . In magnetic field aligned coordinates there is no latitudinal dependence in either of the components and because  $\lambda_{\perp r} = \lambda_{\perp \theta}$  the red line covers the blue line.

In the panels illustrating the mean free path in spherical polar coordinates a clear longitude dependence becomes evident. All three components of the mean free paths show an asymmetry in  $\theta$  due to the HMF structure, which is not symmetric in  $\theta$ . The Fisk-type HMF models show a point symmetry with respect to the origin of the spherical polar coordinate system, which is reflected in the mean free path. Compared to Fig. 4.10, the radial ( $\lambda_{rr}$ ) and longitudinal ( $\lambda_{\phi\phi}$ ) transport coefficients show almost the same behaviour as in the Parker HMF. The most obvious difference is the enhancement of  $\lambda_{\theta\theta}$  just by the HMF configuration without assuming an additional  $\theta$  dependent function in the mean free path. The strength of this effect, however, depends highly on the heliographic longitude in a rest frame corotating with the Sun.

A very similar behaviour of the coefficients can be seen in Fig. 4.12 for the Schwadron-Parker hybrid HMF. Here, the same diffusion coefficients as in the Fisk-Parker HMF are applied, but with the more realistic latitudinal SW speed profile, which was also used for the Parker field. To investigate the overall influence of the Fisk-type fields on the particle transport in the heliosphere, it is important to discuss  $\lambda_{rr}$ ,  $\lambda_{\theta\theta}$  and  $\lambda_{\phi\phi}$  not only in a coordinate system corotating with the Sun, but also in a non-rotating observer's rest frame. In such a coordinate system, these parameters will show a regular time dependence and change periodically with the solar rotation rate. Therefore, the enhancement of  $\lambda_{\theta\theta}$  by the HMF structure will show its influence at all heliographic longitudes in long-term modulation effects as an average over a solar rotation as well as on short time scales.

Comparing the results for the mean free path in the three different HMF models, one can say that Fisk-type fields like the Fisk-Parker or the Schwadron-Parker HMF model can at least partly explain the enhancement of the latitudinal diffusion. To what extent the global HMF structure (Fisk, 1996) or the magnetic field turbulence (Jokipii et al., 1995) for the high latitudinal transport is still an open question and part of the discussion in the present work.

# A Comparison of the Diffusion Tensor in different HMF Configurations

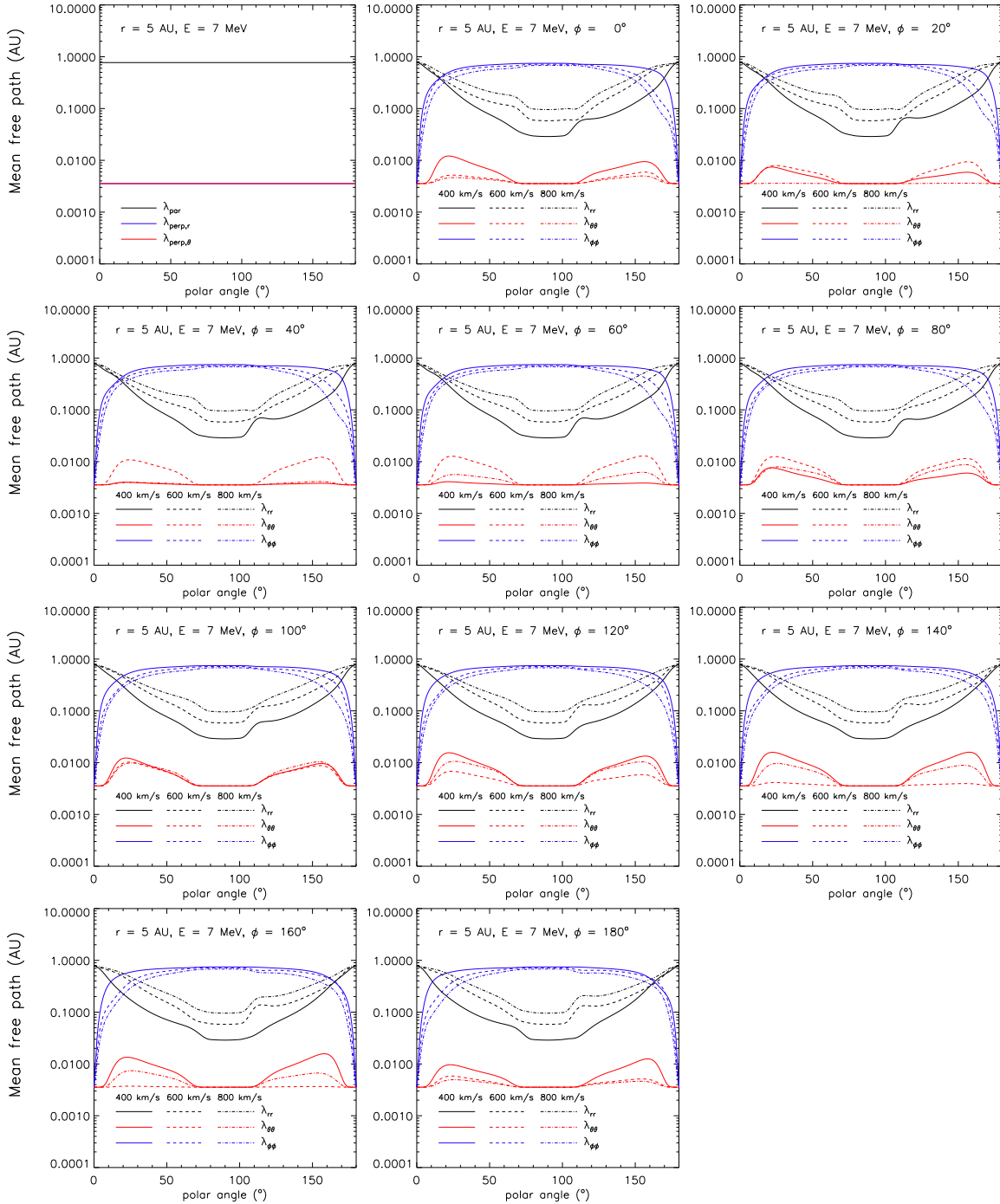


Figure 4.11: The latitudinal and longitudinal dependence of the particle mean free path in a Fisk-Parker hybrid HMF for 7 MeV electrons at 5 AU.

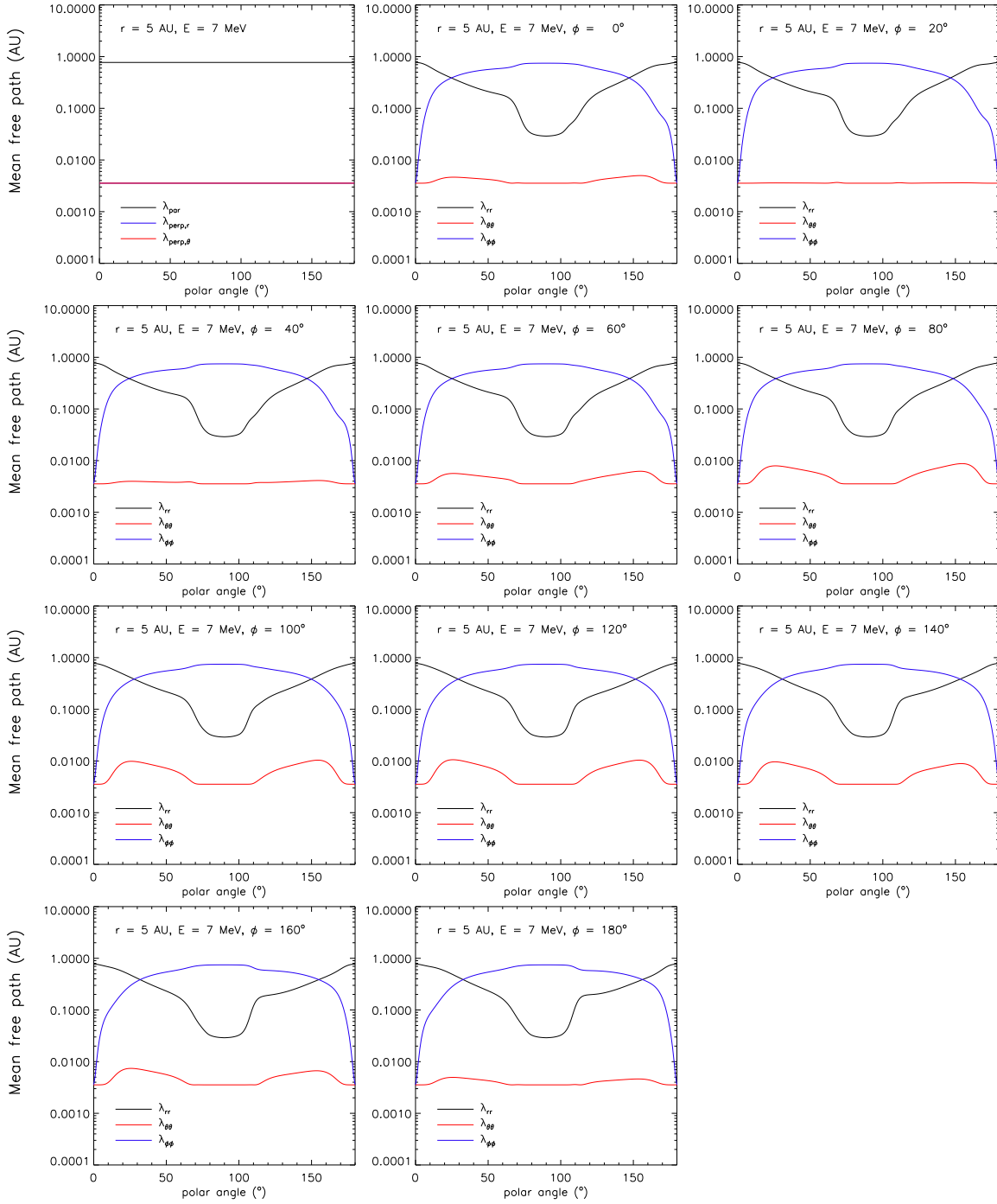


Figure 4.12: The latitudinal and longitudinal dependence of the particle mean free path in a Schwadron-Parker hybrid HMF for 7 MeV electrons at 5 AU.



# Chapter 5

## Setting up a Model for Particle Propagation

Based on Parker’s transport equation, different models were developed to investigate the modulation of cosmic rays in the heliosphere. Analytical solutions could be found for simplifications of the TPE (Gleeson and Axford, 1968; Chenette et al., 1974). For a study cases to be applied to reproduce heliospheric observations in detail, numerical models are needed. Significant progress was achieved since the first 2D model was developed by Fisk (1976). Jokipii and Kopriva (1979) were able to include gradient and curvature drifts as well as a flat current sheet into their 2D model, while Potgieter and Moraal (1985) introduced a wavy current sheet into their South African steady-state modulation model. This was later improved by Hattingh and Burger (1995) and extended to a 3D model (Hattingh, 1998), see also the reviews by Potgieter (1998) or Potgieter et al. (2001). To investigate particle transport perpendicular to the mean HMF, Ferreira et al. (2001a,b) included the Jovian magnetosphere as an electron source into their 3D steady-state model. A time-dependent model was developed by Fichtner et al. (2000) based on the VLUGR3 code (Blom and Verwer, 1994, 1996). This model was used by Kissmann et al. (2003, 2004) to simulate CIRs in the heliosphere and by Lange et al. (2006) for long-term studies of the electron propagation in a time-dependent 3D heliosphere, especially the latitudinal transport during solar minimum.

### The TPE in Spherical Polar Coordinates

The current work employs a refined version of the VLUGR3-based model developed by Fichtner et al. (2000). VLUGR3 solves partial differential equations of the form

$$F(t, x, y, z, u, u_x, u_y, u_z, u_{xx}, u_{yy}, u_{zz}, u_{xy}, u_{xz}, u_{yz}) = 0. \quad (5.1)$$

where  $u_x, u_{xx}$  etc. denote partial derivatives, and  $x, y$  and  $z$  are cartesian coordinates. Since it is not possible to solve the full 3D TPE also in energy with this code, it is

necessary to derive a simplification of the differential equation because of the rigidity dependent adiabatic term. Therefore, following an idea by Drury and Völk (1981), Fichtner et al. (2000) employed the second moment of the distribution function

$$P_e = \frac{4\pi}{3} \int_0^\infty f(\vec{r}, p, t) p v p^2 dp \quad (5.2)$$

with the particle speed  $v$  and the momentum  $p$  in the SW rest frame to calculate the cosmic ray pressure  $P_e$ . Computing the second moment of the whole Parker TPE leads to

$$\frac{\partial P_e}{\partial t} = \vec{\nabla} \cdot (\langle \hat{\kappa}'_{\text{sphere}} \rangle \cdot \vec{\nabla} P_e) - \vec{u}_{\text{sw}} \cdot (\vec{\nabla} P_e) + \frac{4}{3r^2} \frac{\partial}{\partial r} (r^2 u_{\text{sw}}) P_e + \langle S \rangle \quad (5.3)$$

Note that the term  $S$  now describes the source integrated over all rigidities. The application of this method gives rise to two major problems: 1) How accurate is the hydrodynamic (i.e. moment-based) 2) The diffusion tensor depends on the rigidity,  $P = pc/q$ , so a rigidity averaged diffusion tensor has to be used in the equation for the electron pressure, see also Drury and Völk (1981). These two arguments lead to the interpretation of equation (5.3) as to describe an energy averaged behaviour of the electron flux in the heliosphere. However, for simulating the electron flux in the heliosphere, the parameters  $\hat{\kappa}'_{\text{sphere}}$  and  $S$  are chosen at the rigidities of interest.

Kissmann (2002) tested the time-dependent simplified VLUGR3-based model against the South African steady-state code (Ferreira et al., 2001a) and found a qualitative agreement in the results. Therefore, the Fichtner-model is very useful to investigate the time-dependent behaviour of the low energy electron flux in the heliosphere. Note that the VLUGR3-based model may not be adequate for deriving quantitative conclusions in all cases.

For the purpose of solving the TPE in a computer-based simulation, an explicit form of the differential equation is required. The execution of all multiplications and derivatives leads to

$$\begin{aligned} \frac{\partial f}{\partial t} = & \left( \frac{1}{r^2} \frac{\partial}{\partial r} (r^2 \kappa_{rr}) + \frac{1}{r \sin \theta} \frac{\partial}{\partial \theta} (\kappa_{\theta r} \sin \theta) + \frac{1}{r \sin \theta} \frac{\partial \kappa_{\phi r}}{\partial \phi} - u_{\text{sw}} \right) \frac{\partial f}{\partial r} \quad (5.4) \\ & + \left( \frac{1}{r^2} \frac{\partial}{\partial r} (r \kappa_{r\theta}) + \frac{1}{r^2 \sin \theta} \frac{\partial}{\partial \theta} (\kappa_{\theta\theta} \sin \theta) + \frac{1}{r^2 \sin \theta} \frac{\partial \kappa_{\phi\theta}}{\partial \phi} \right) \frac{\partial f}{\partial \theta} \\ & + \left( \frac{1}{r^2 \sin \theta} \frac{\partial}{\partial r} (r \kappa_{r\phi}) + \frac{1}{r^2 \sin \theta} \frac{\partial \kappa_{\theta\phi}}{\partial \theta} + \frac{1}{r^2 \sin^2 \theta} \frac{\partial \kappa_{\phi\phi}}{\partial \phi} \right) \frac{\partial f}{\partial \phi} \\ & + \kappa_{rr} \frac{\partial^2 f}{\partial r^2} + \frac{\kappa_{\theta\theta}}{r^2} \frac{\partial^2 f}{\partial \theta^2} + \frac{\kappa_{\phi\phi}}{r^2 \sin^2 \theta} \frac{\partial^2 f}{\partial \phi^2} \\ & + \frac{2\kappa_{r\phi}}{r \sin \theta} \frac{\partial^2 f}{\partial r \partial \phi} + \frac{8u_{\text{sw}}}{3r} f + S \end{aligned}$$

It can also be formulated as

$$\begin{aligned} \frac{\partial f}{\partial t} = & a_{rr} \frac{\partial^2 f}{\partial r^2} + a_{\theta\theta} \frac{\partial^2 f}{\partial \theta^2} + a_{\phi\phi} \frac{\partial^2 f}{\partial \phi^2} + a_{r\phi} \frac{\partial^2 f}{\partial r \partial \phi} \\ & + a_r \frac{\partial f}{\partial r} + a_\theta \frac{\partial f}{\partial \theta} + a_\phi \frac{\partial f}{\partial \phi} + a_P f + S \end{aligned} \quad (5.5)$$

with

$$\begin{aligned} a_{rr} &= \kappa_{rr} \\ a_{\theta\theta} &= \frac{\kappa_{\theta\theta}}{r^2} \\ a_{\phi\phi} &= \frac{\kappa_{\phi\phi}}{r^2 \sin^2 \theta} \\ a_{r\phi} &= \frac{2\kappa_{r\phi}}{r \sin \theta} \\ a_r &= \frac{1}{r^2} \frac{\partial}{\partial r} (r^2 \kappa_{rr}) + \frac{1}{r \sin \theta} \frac{\partial}{\partial \theta} (\kappa_{\theta r} \sin \theta) + \frac{1}{r \sin \theta} \frac{\partial \kappa_{\phi r}}{\partial \phi} - u_{\text{SW}} \\ a_\theta &= \frac{1}{r^2} \frac{\partial}{\partial r} (r \kappa_{r\theta}) + \frac{1}{r^2 \sin \theta} \frac{\partial}{\partial \theta} (\kappa_{\theta\theta} \sin \theta) + \frac{1}{r^2 \sin \theta} \frac{\partial \kappa_{\phi\theta}}{\partial \phi} \\ a_\phi &= \frac{1}{r^2 \sin \theta} \frac{\partial}{\partial r} (r \kappa_{r\phi}) + \frac{1}{r^2 \sin \theta} \frac{\partial \kappa_{\theta\phi}}{\partial \theta} + \frac{1}{r^2 \sin^2 \theta} \frac{\partial \kappa_{\phi\phi}}{\partial \phi} \\ a_P &= \frac{8u_{\text{SW}}}{3r} \end{aligned}$$

which is the differential equation to be solved with the VLUGR3 code.

## Setting up a Propagation Model with VLUGR3

VLUGR3 is a vectorizable adaptive grid solver for partial differential equations in three spatial dimensions (Blom and Verwer, 1994, 1996). The application of this numerical code to problems in spherical geometry is, however, not intended and so it is not possible to solve equations with periodic boundary conditions directly. Hence, periodicity in the longitudinal direction has to be realised artificially.

Figure 5.1 explains the method applied to the VLUGR3-based model. The sketch shows an  $r$ - $\phi$ -plane of the computational domain with the physical area ranging from 0 to  $2\pi$ . The Jovian magnetosphere is included as an electron source at  $\phi = \pi$ . To assure periodicity in the  $\phi$ -direction, the computational domain is extended to cover latitudes from  $-\pi$  to  $3\pi$ . The source has to be included in both the left and the right additional space at  $\phi = -\pi$  and  $\phi = 3\pi$ . The orbital motion of Jupiter in  $\phi$ -direction would drive the sources over the boundaries of the computational domain out of the simulation space. For this reason, the underlying coordinate system rotates with the angular speed of Jupiter. Following each time step of the simulation, a weighted averaging process is applied to the matching regions (yellow and green) to

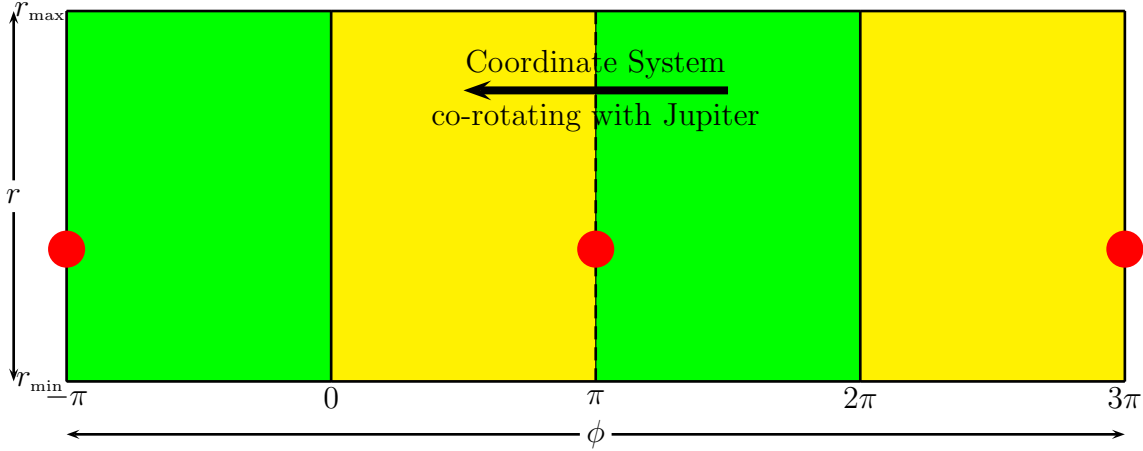


Figure 5.1: Implementation of periodic boundary conditions in VLUGR3. The picture shows an  $r$ - $\phi$ -plane of the computational domain. In the  $\phi$ -direction, the physical area ranges from 0 to  $2\pi$ . The Jovian magnetosphere is included as an electron source at  $\phi = \pi$ . To receive periodicity in the longitudinal direction, the computational domain needs to cover the region from  $-\pi$  to  $3\pi$ . The source has to be included in both the left and the right additional space at  $\phi = -\pi$  and  $\phi = 3\pi$ .

ensure consistency. Using this method, the electron flux over the periodic border of the physical domain from  $2\pi$  to 0 and back is compensated.

The simulation grid is equally spaced in the two angular directions  $\theta$  and  $\phi$ . In the radial direction a grid spacing rising proportional to  $r^2$  from inner to outer boundary was chosen to achieve a higher resolution in the inner heliosphere:

$$\begin{aligned} r &= r_{\min} + \delta r \cdot x(x + 2x_0) \\ \theta &= \theta_{\min} + \delta\theta \cdot y \\ \phi &= \phi_{\min} + \delta\phi \cdot z \end{aligned} \tag{5.6}$$

coordinate	boundaries	number of grid points
solar distance $r$	$r_{\min} = 1/215 \text{ AU}, r_{\max} = 100 \text{ AU}$	213
latitude $\theta$	$\theta_{\min} = \pi/180, \theta_{\max} = \pi - \pi/180$	61
longitude $\phi$	$\phi_{\min} = -\pi, \phi_{\max} = 3\pi$	145

Table 5.1: Parameters of the numerical grid, i.e. the boundaries and grid point numbers of the three spatial dimensions.

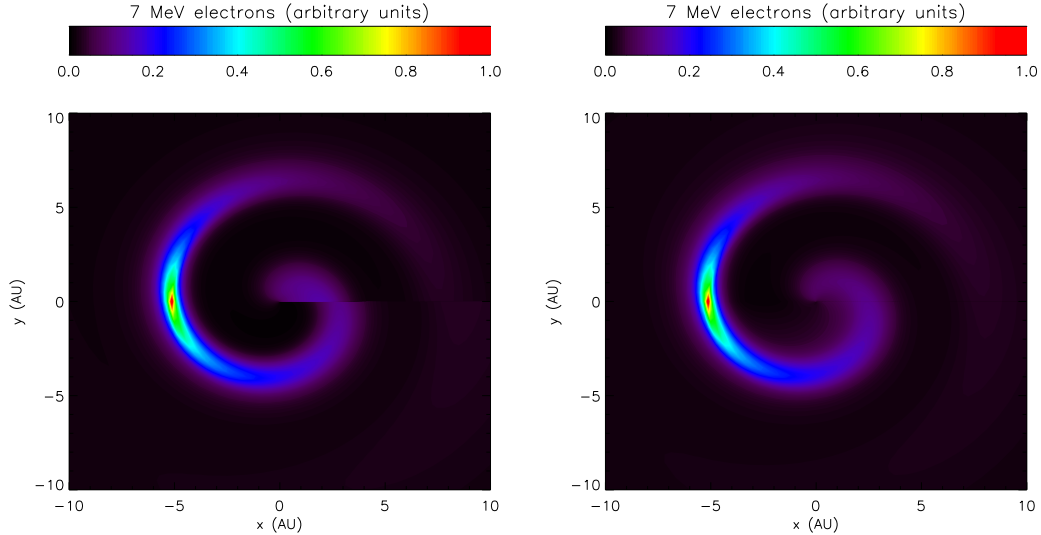


Figure 5.2: The first simulation test. The two contour plots show the calculated electron flux in arbitrary units in the equatorial plane – a test case with an electron source located at a distance of  $r \approx 5$  AU to the Sun. The left panel shows a simulation without applying the averaging process. The right panel displays simulation data with an applied averaging process and clearly demonstrates the effectiveness of the averaging.

with the parameters

$$\begin{aligned}
 \delta r &= \frac{r_{\max} - r_{\min}}{1 + 2x_0} \\
 \delta \theta &= \theta_{\max} - \theta_{\min} \\
 \delta \phi &= \phi_{\max} - \phi_{\min} \\
 x_0 &= 6.37 \cdot 10^{-3}
 \end{aligned} \tag{5.7}$$

The numerical grid coordinates  $x$ ,  $y$  and  $z$  ranging from 0 to 1 are used in the VLUGR3 code. The boundaries and grid point numbers chosen for the numerical computation are summarised in Table 5.1.

Figure 5.2 illustrates a simulation test result of the VLUGR3-based model. Two contour plots show the computed electron flux in the equatorial plane of the heliosphere. For this test case, an electron source was located at  $r \approx 5$  AU,  $\theta = \pi/2$  and  $\phi = \pi$  in spherical polar coordinates or  $x \approx -5$  AU,  $y = 0$  AU and  $z = 0$  AU, respectively. Electrons of galactic origin were not taken into account. The Sun is located in the center of the plot and the underlying magnetic field is a Parker HMF with a solar wind speed of 400 km/s at all latitudes. The flux maximum is clearly visible at the source region and the electrons diffuse parallel and perpendicular to the Parker spiral into the heliosphere. The left panel shows a simulation without the averaging process. The flux

at the periodic boundary at  $\phi = 0$  and  $\phi = 2\pi$  (the positive x-axis) is not equal, as it is expected from the method without the averaging process. The right panel displays simulation data with the applied averaging process. The data at  $\phi = 0$  and  $\phi = 2\pi$  are equal and the requirement of periodic boundary conditions is fulfilled.

Based on these results, the VLUGR3-based model adapted in this way can now be applied to compute the electron propagation inside the heliosphere for both, galactic and Jovian electrons, influenced by the different HMF models described in chapter 3. Conclusions on the diffusion tensor and the HMF configuration can be drawn from theoretical studies and from a comparison between the model data and spacecraft measurements.

# Chapter 6

## Investigating the Electron Flux in a Parker HMF

In this chapter the model results for the 7 MeV electron flux are presented and compared to count rates measured with the IMP-8 (Interplanetary Monitoring Platform), SOHO (SOlar and Heliospheric Observatory) and the Ulysses spacecraft. The solar cycle dependence of the electron flux is studied and discussed for the Parker field.

### Spacecraft Measurements

For comparison of the model results, measurements from three space missions were chosen: IMP-8, SOHO and Ulysses. These three spacecraft orbiting the Sun on different trajectories in the inner heliosphere are introduced below.

#### IMP-8

The IMP-8 mission was launched on October 26, 1973, in order to collect magnetic field, plasma and energetic particle data in an orbit around the Earth with an altitude of 35 Earth radii. For 33 years the satellite operated successfully until the contact was lost on October 7, 2006. Its measurements allowed for detailed studies of energetic particles on short time scales, e.g. CIRs, as well as solar cycle dependent phenomena. Therefore, the IMP-8 mission is still regarded as one of the most important spacecraft to investigate the time-dependent behaviour of the solar wind and energetic charged particles in the inner heliosphere.

This work employs the 2 – 12 MeV electron measurements collected by the instrument built at the University of Chicago. These data are shown in Fig. 6.1 for the time span from 1990 to 2000 together with the SOHO/EPHIN electron data (2.64 – 10.4 MeV), which cover the years 1996 to 2009. The data are cleaned of solar events. To fit the IMP-8 measurements, the SOHO data were multiplied with a factor of four. The electron count rate shows a clear periodicity of  $\sim 13$  months caused

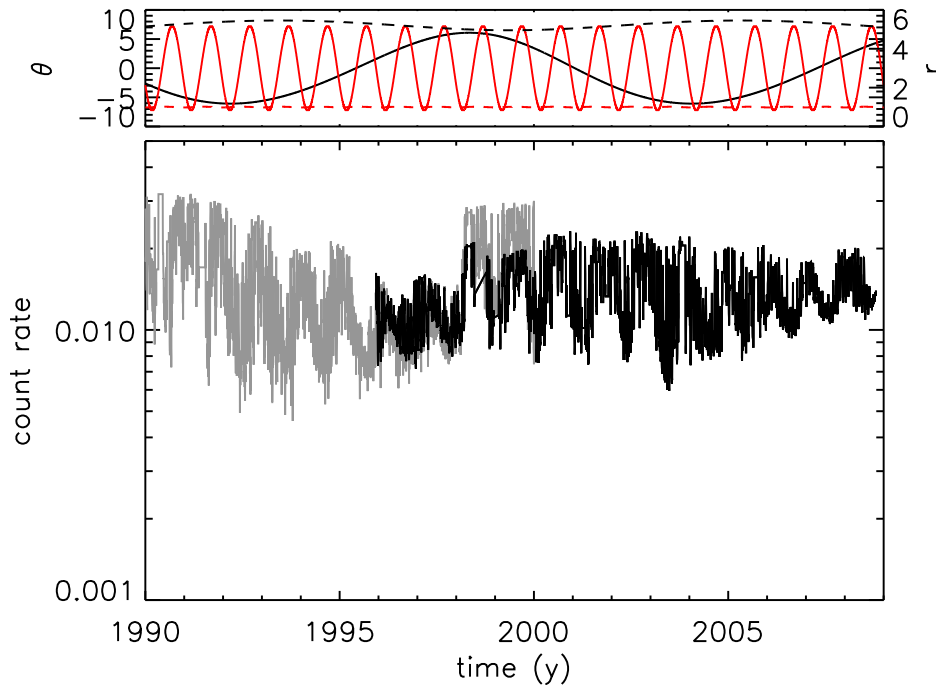


Figure 6.1: Electron data measured by IMP-8 and SOHO/EPHIN from 1990 to 2009. The the lower panel shows daily averaged IMP-8 measurements of 2 – 12 MeV electrons (grey line) from 1990 to 2000 and SOHO/EPHIN measurements of 2.64 – 10.4 MeV electrons from 1996 to 2009 (black line) in units of counts/second. The SOHO count rate was multiplied with a factor of four to fit the IMP-8 count rate. The upper panel displays the heliographic latitude  $\theta$  (solid lines) and the radial distance  $r$  to the Sun (dashed lines) of the Earth (red lines), which indicates the spacecraft position, and Jupiter (black lines).

by the Jovian electrons, as explained in chapter 4. Additionally, the data underlies a solar cycle dependence with the electron count rate variations reaching higher maxima and higher amplitudes during solar maximum periods than during solar minimum.

## SOHO

SOHO is an ongoing joint ESA/NASA mission (Domingo et al., 1995), which was launched on December 2, 1995. It is located at the L1 Lagrangian point between the Sun and the Earth and, therefore, moves around the Sun together with the Earth. It was the first solar observatory not to orbit the Earth, so that uninterrupted observations of the Sun became possible. Like IMP-8, several instruments supply plasma and energetic particle data.

For the evaluation of the model data, the 2.64 – 10.4 MeV electron measurements



of the EPHIN (Electron Proton Helium INstrument) (Müller-Mellin et al., 1995) built at the University of Kiel were chosen. The spacecraft data are shown in Fig. 6.1 for the years 1996 to 2009 together with the IMP-8 electron measurements from 1990 to 2000. The period after 2005 reveals an unexpected development of the count rate. The amplitude of the 13-months variation decreases while the flux maxima stay at the same level.

## Ulysses

Prior to the Ulysses mission, all other spacecraft took trajectories in the ecliptic plane. The spacecraft was launched on October 6, 1990, with the special task to explore the third dimension of the heliosphere (Wenzel et al., 1992). Its trajectory is displayed in Fig. 6.2. Ulysses was directed towards Jupiter to perform a swing-by maneuver in order to reach a trajectory around the Sun which is almost perpendicular to the ecliptic. Thus, the first measurements of the latitudinal dependence of the heliospheric structure became possible. One orbit of Ulysses takes  $\sim 6$  years.

This work employs the 2.5 – 7 MeV electron measurements collected with the KET (Kiel Electron Telescope) built at the University of Kiel (Simpson et al., 1992). The spacecraft data from 1990 to 2008 are shown in Fig. 6.3. At first, the electron count rate decreases slowly as Ulysses still moves in the ecliptic plane to larger radial

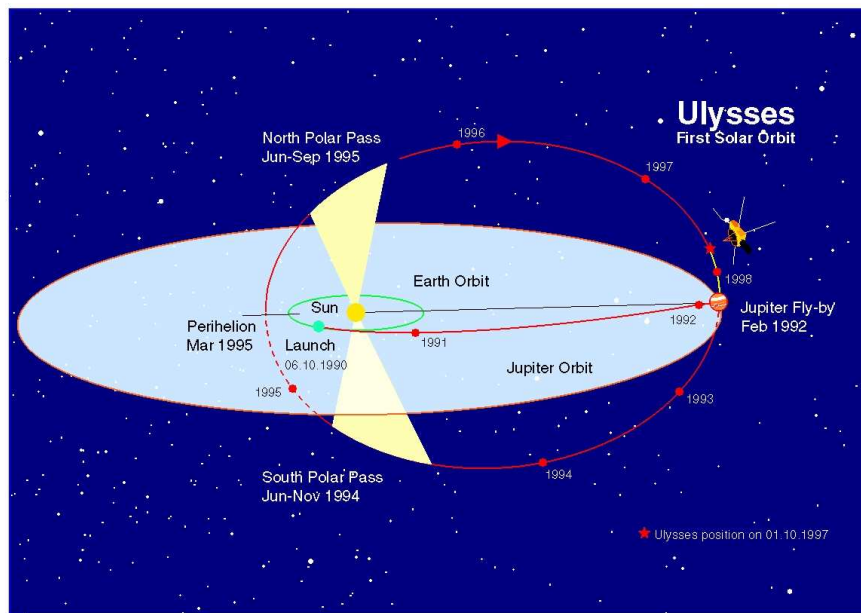


*Figure 6.2: The Ulysses trajectory. The Ulysses spacecraft was launched on October 6, 1990, and directed towards Jupiter. There it performed a swing-by maneuver to reach its final trajectory almost perpendicular to the ecliptic plane. (Taken from the ESA Web Site, 1997)*

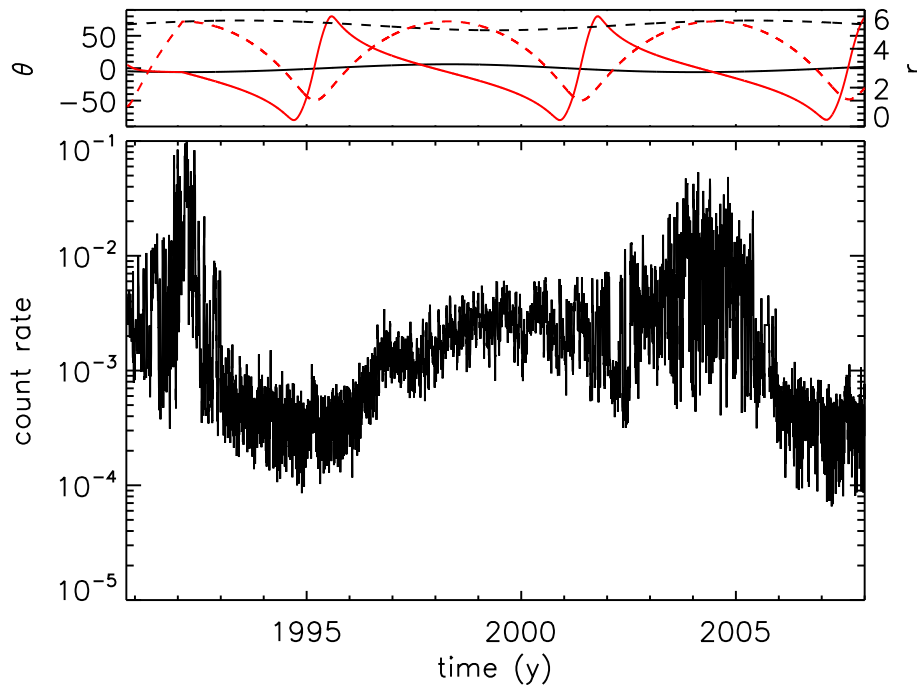


Figure 6.3: Electron data measured by *Ulysses*/*KET* from 1990 to 2008. The lower panel shows daily averaged corrected *Ulysses*/*KET* measurements of 2.5 – 7 MeV electrons in units of counts/second. The upper panel displays the heliographic latitude  $\theta$  (solid lines) and the radial distance  $r$  to the Sun (dashed lines) of the spacecraft (red lines) and Jupiter (black lines).

distances from the Sun. From  $\sim 1992.5$  on, the count rate rises again to peak when the spacecraft encounters Jupiter in February 1992. A second smaller peak appears during the ecliptic crossing of the first fast latitude scan (FLS). After 1996 the electron count rate rises again to stay constantly on a high level while *Ulysses* moves from the northern to the southern polar regions of the heliosphere. In February 2004 the spacecraft approached Jupiter again for a distant flyby, which is also reflected by the electron count rate.

## Model Results for the Electron Flux in the Inner Heliosphere

This section is dedicated to the description of the model results obtained in this work, while a comparison to earlier results is given in the conclusions of this chapter. As a first approach, the time dependence of the parameters influencing the particle transport described in chapter 4 is investigated without taking into account the variation of  $\kappa_{\parallel}$

with the HMF strength measured at Earth, i.e.  $f_2(t) = 1$  in equation (4.19). The two models describing the evolution of the PCH during the solar cycle are tested and discussed for a time dependence (a) directly related to the sunspot number (see Fig. 2.2) and a time dependence (b) shifted with respect to the sunspot cycle. In the numerical simulation code, the hyperbolic tangent functions in equations (4.8), (4.10), (4.26) and (4.28) become

$$\begin{aligned} \tanh\{g(t - t_0)\} &\longrightarrow \tanh\{g'(i - i_0)\} \\ \tanh\{g(t_0 - t)\} &\longrightarrow \tanh\{g'(i_0 - i)\} \end{aligned}$$

with  $i \in \mathbb{N}$  counting the time steps of the simulation and  $i_0$  defining the number of the time steps around which the solar cycle transitions are centered. The parameter

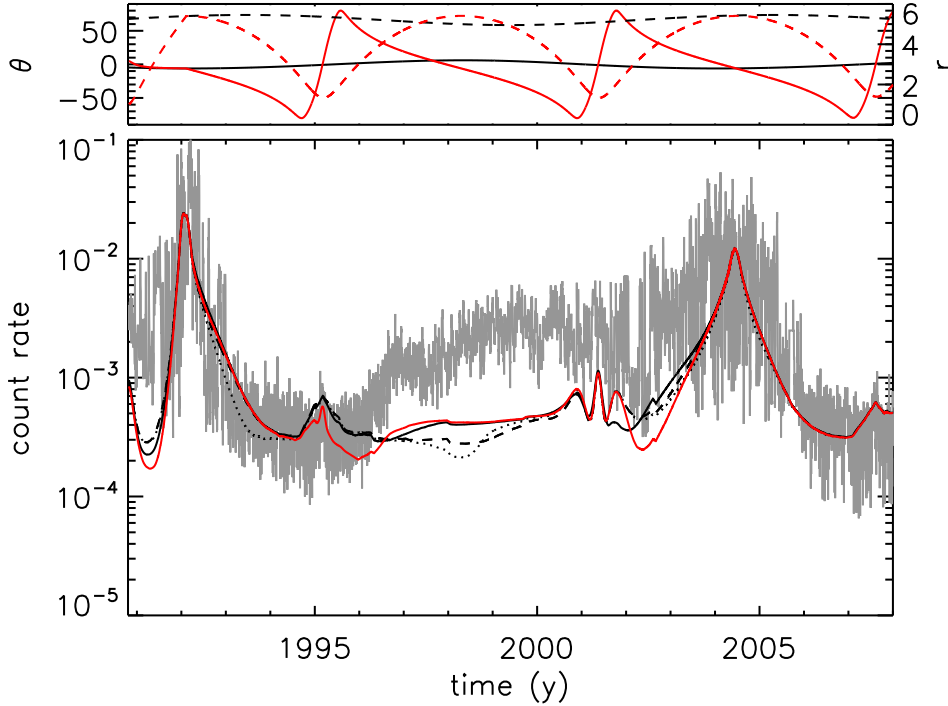


Figure 6.4: Comparison of Ulysses/KET measurements to model results for the 7 MeV electron flux. The dashed and dotted black lines display the results for the solar cycle models 1 and 2, respectively, as explained in chapter 4, directly related to the sunspot number. The black and red solid lines show the results for the models 1 and 2 with a time dependence shifted with respect to the sunspot cycle. The transition times from solar minimum to maximum and back are explained in the text. Parameters:  $u_{min} = 400$  km/s,  $u_{max} = 800$  km/s,  $v = 6$ ,  $g' = 0.075$ ,  $f_2(t) = 1$ . For the time-shifted solar cycle dependence, the transitions were set to  $t_0^{(1)} = 1990.85$ ,  $t_0^{(2)} = 1996.12$ ,  $t_0^{(3)} = 2002.24$ .

$g'$  determining the transition time from solar minimum to maximum and back was set to the value  $g' = 0.075$ . With a time step size of  $\Delta t = 0.0712 \text{ y} \approx 26 \text{ d}$  (the solar rotation period), this corresponds to a period of  $\sim 2$  years for one transition. The minimum and maximum solar wind speeds were chosen to  $u_{\min} = 400 \text{ km/s}$  and  $u_{\max} = 800 \text{ km/s}$ , respectively. The maximum enhancement of  $\kappa_{\perp\theta}$  was set to  $v = 6$ , the same value used by Lange et al. (2006) for their model calculations. The strength of the Jovian electron source is assumed to be constant during the solar cycle. In order to be able to differentiate between Jovian and galactic electrons, both components are computed in separate simulations with the same transport parameters.

The results of these four simulations are displayed in Fig. 6.4 and compared to Ulysses measurements. The dashed and dotted black lines show the electron flux along the Ulysses trajectory according to model 1 and 2, respectively, directly related to the sunspot number. Both lines show the large peaks during the Jupiter encounters in 1992 and 2004, as well as the small peaks during the ecliptic crossings of the fast

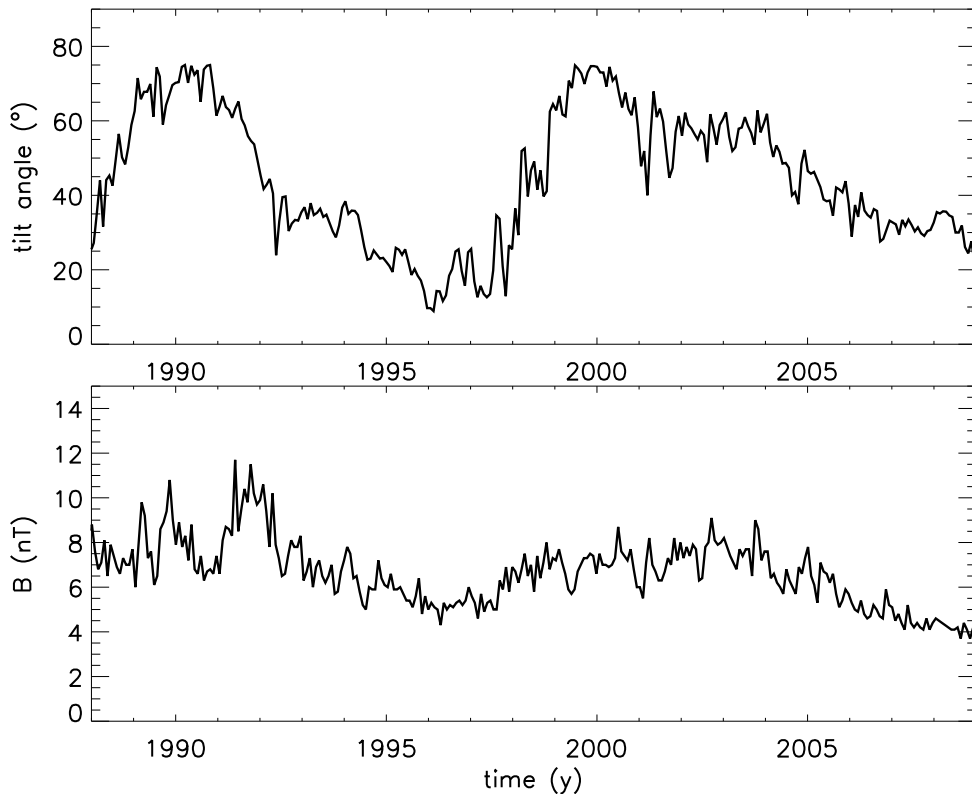


Figure 6.5: The upper panel displays the tilt angle  $\alpha$  between the solar rotational axis and the symmetry axis of the solar magnetic field (Hoeksema, 1995). The lower panel shows the HMF strength measured at the Earth’s orbit (Goddard Space Flight Center, 2009).

latitude scans in 1995, 2001 and 2007, characteristics which can also be found in the measured data. In both cases, the expected increase of the electron flux in 1996 does not appear. Model 2 suggests, that there might be such an increase late in 1998, but still both simulation results cannot explain the data measured by Ulysses. Therefore, both models were tested with a time dependence shifted with respect to the sunspot cycle. The transition from solar maximum to minimum conditions is centered around  $t_0^{(1)} = 1990.85$ , back to solar maximum conditions around  $t_0^{(2)} = 1996.12$  and again to solar minimum around  $t_0^{(3)} = 2002.24$ . The black and red solid lines in Fig. 6.4 represent the simulation results for model 1 and model 2, respectively. Both lines show the five peaks described above. The main difference can be found in the increase of the electron flux in the year 1996, which is more pronounced in the red line. Hence, model 2 with a shifted time dependence was chosen as the basis of the following investigation with the function  $f_2(t) = (B_0/B)^n$  relating the diffusion coefficients to the magnetic field strength of the HMF measured at the Earth's orbit and the tilt angle of the solar magnetic field.

These data are displayed in Fig. 6.5 for the time period from 1988 to 2009. The upper panel shows the tilt angle  $\alpha$  between the solar rotation axis and the solar magnetic field symmetry axis. During the solar cycle the tilt angle varies between  $\sim 80^\circ$  during solar maximum and  $\sim 10^\circ$  during solar minimum. Especially during the current solar minimum the tilt angle shows a noticeable behaviour of dropping very slowly to lower values, which is an interesting topic for modulation studies (Heber et al., 2009). Analytic formulae describing the solar cycle variation of the tilt angle are e.g. given by Alanko-Huotari et al. (2007) or Burger et al. (2008). The lower panel presents the HMF strength measured at the Earth's orbit. It shows the same solar cycle dependence as the tilt angle, varying between  $\sim 10$  nT during solar maximum and  $\sim 5$  nT during solar minimum conditions. These data are employed in the transport model as a measure of the total HMF turbulence and, hence, related to the diffusion tensor as explained in chapter 4.

To achieve a deeper insight into the solar cycle dependence of the  $\kappa_{\parallel}$  variation, the electron flux at the Earth's orbit and Ulysses is investigated with simulations for different negative values of  $n$  between 0 and  $-3$  in steps of  $\Delta n = 0.5$ . In contrast to the simulation presented previously, the maximum enhancement of  $\kappa_{\perp\theta}$  was chosen to  $v = 8$ . Additionally, the radial perpendicular component  $\kappa_{\perp r}$  was increased by 25% during the solar maximum period (Ferreira et al., 2001b; Lange et al., 2006). This leads to an enhanced diffusion of electrons into the inner heliosphere.

The results of these simulations for the electron flux at the Earth's orbit are displayed in Fig. 6.6. Seven lines represent the electron simulation data for the IMP-8 and SOHO spacecraft with  $n = 0$  for the lowest curve,  $n = -3$  for the highest electron data and the other lines ordered accordingly in between. The three high solid black lines computed with  $n \in [-2, -2.5, -3]$  are not able to explain the measured data during most parts of the solar cycle. The 13-months period caused by the Jovian electrons is visible only during the solar minimum phases between 1995 and 1998 and again after 2005, while the measured electron count rate is overestimated during so-

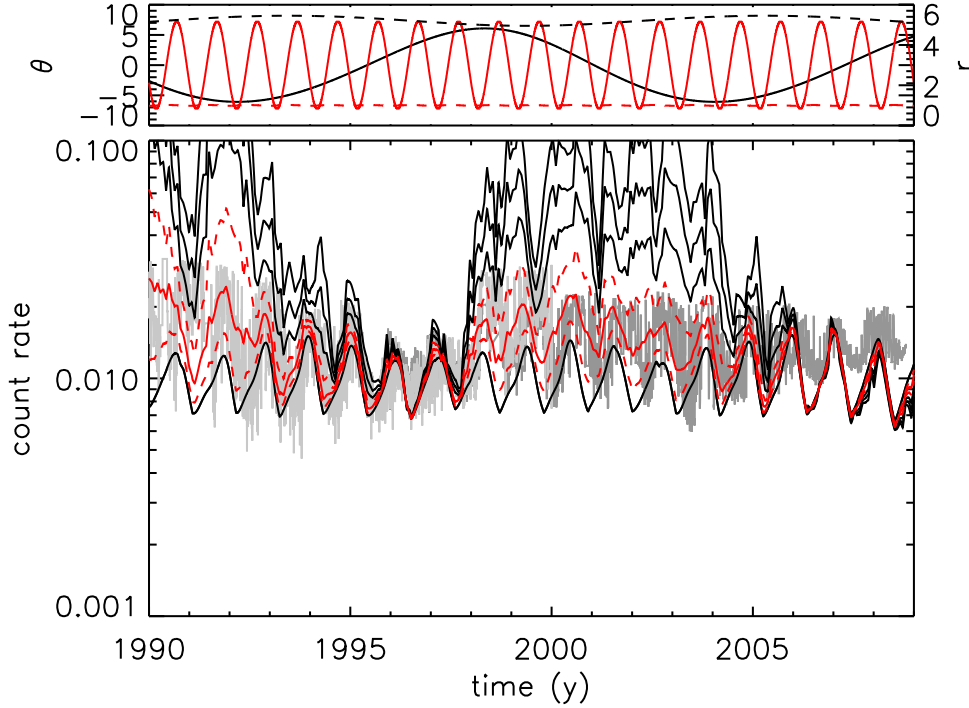


Figure 6.6: IMP-8 and SOHO/EPHIN measurements and the 7 MeV electron flux simulations for different constant values of  $n$ . The plot shows the results of seven simulations with  $n \in [0, -0.5, -1, -1.5, -2, -2.5, -3]$  ordered from the lowest ( $n = 0$ ) to the highest ( $n = -3$ ) curve. Parameters:  $u_{min} = 400$  km/s,  $u_{max} = 800$  km/s,  $v = 8$ ,  $g' = 0.075$ ,  $t_0^{(1)} = 1990.85$ ,  $t_0^{(2)} = 1996.12$ ,  $t_0^{(3)} = 2002.24$ . The upper panel is the same as in Fig. 6.1.

lar maximum to a large extent. This can be explained considering the magnetic field measurements shown in Fig. 6.5. During the two solar minima, the measured HMF strength has values around 5 nT. With  $B_0 = 5$  nT, the function  $f_2(t) = (B_0/B)^n$  describing the impact of the magnetic field strength on the particle transport becomes unity and the influence of  $B$  on the transport coefficients vanishes independently of the exponent  $n$ , while  $\kappa_{\parallel}$  is increased during solar maximum. The simulation with  $n = 0$  (no influence of  $B$  on  $\kappa_{\parallel}$  during the whole solar cycle) reproduces the 13-months period nicely, but there is almost no dependence on the solar activity cycle. The solid red line represents the simulation data for  $n = -1$  and was chosen to be the result closest to the IMP-8 and SOHO/EPHIN measurements and will, thus, be discussed in detail below. The two dashed red lines present the lower ( $n = -0.5$ ) and upper ( $n = -1.5$ ) limit for the exponent  $n$ . The period after 2005 cannot be explained applying the current model. Careful investigation is needed to decide whether SOHO/EPHIN has measured an influence of the solar cycle, which is not understood yet or the rising flux

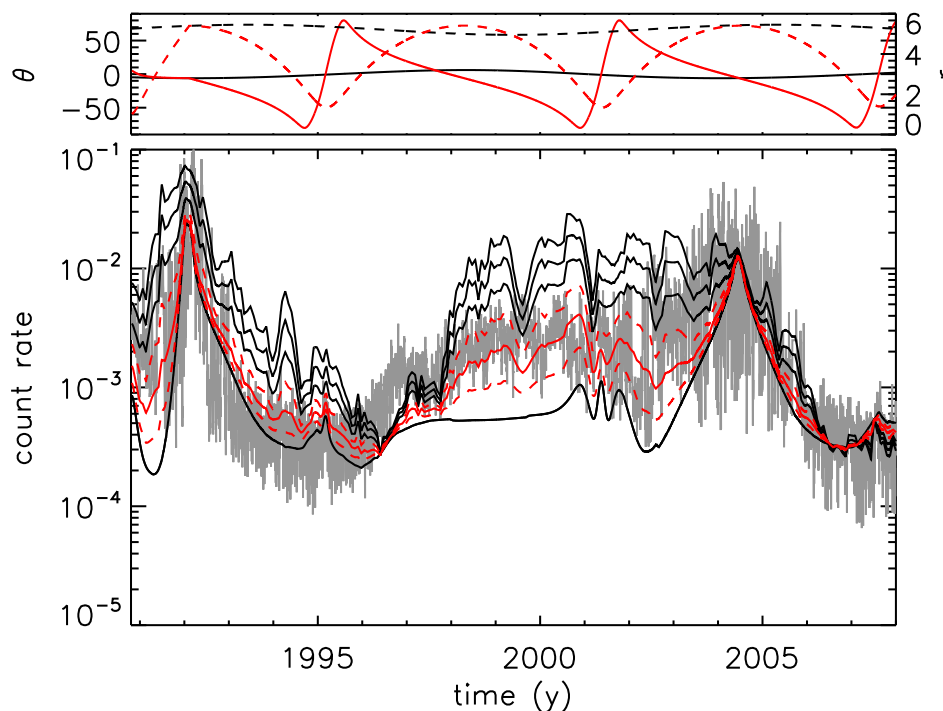


Figure 6.7: The same as Fig. 6.6, but for *Ulysses*/KET.

is caused by the instrument itself.

Figure 6.7 shows the results of the same simulations for the *Ulysses* spacecraft. Similar to the results at the Earth's orbit,  $n = 0$  produces the lowest curve, while  $n = -3$  leads to the highest electron flux levels. The red solid line ( $n = -1$ ) was chosen as the result to be on average closest to the *Ulysses*/KET measurements. The upper ( $n = -1.5$ ) and lower ( $n = -0.5$ ) red dashed lines represent the upper and lower limits for most parts of the *Ulysses* data. However, it is obvious that during the solar cycle different values of  $n$  produce the best data fit; especially between 1996 and 1998 the results for  $n \in [-2, -2.5, -3]$  show the high increase which was measured by *Ulysses*. This is conform to the IMP/SOHO measurements where all seven model results were able to explain the data between 1996 and 1998. After 2005 the different models are not distinguishable, consistent to the measurements at the Earth's orbit. These results and their comparison to the *Ulysses* data suggest the conclusion that  $n$  depends on the solar cycle. Ferreira et al. (2003b) relate  $n$  to the tilt angle  $\alpha$ , an approach which is discussed below.

The model results for  $n = -1$  are displayed in more detail in Fig. 6.8 for the IMP-8 and SOHO measurements and in Fig. 6.9 for the *Ulysses*/KET data, respectively. In both figures, the solid black line represents the total electron flux, while the dashed and dash-dotted black lines show the Jovian and galactic electrons, respectively. In

Fig. 6.8, the Jovian electrons show their 13-months period to be weakly affected by the solar cycle and the HMF strength. The variation shows lower maxima and a smaller amplitude during the solar minima compared to solar maximum conditions. However, a clear solar cycle dependence becomes evident in the galactic electrons by showing a flux level to be higher during solar maximum than during solar minimum. Although Jupiter is a strong electron source, Jovian electrons only dominate the ecliptic in the inner heliosphere during solar minimum conditions. Solar maximum periods allow the galactic electron component to rise to high values with Jovian electrons only reaching similar flux levels while the spacecraft are magnetically connected to Jupiter along a Parker spiral. Together, the model results for both electron components can explain the IMP-8 and SOHO/EPHIN measurements to a large extent. As mentioned above, the period after 2005 requires careful investigation to achieve consistency between model and measurements.

The simulation results show similar consequences of the solar cycle along the Ulysses trajectory (Fig. 6.9). The Jovian electron component rises while the spacecraft ap-

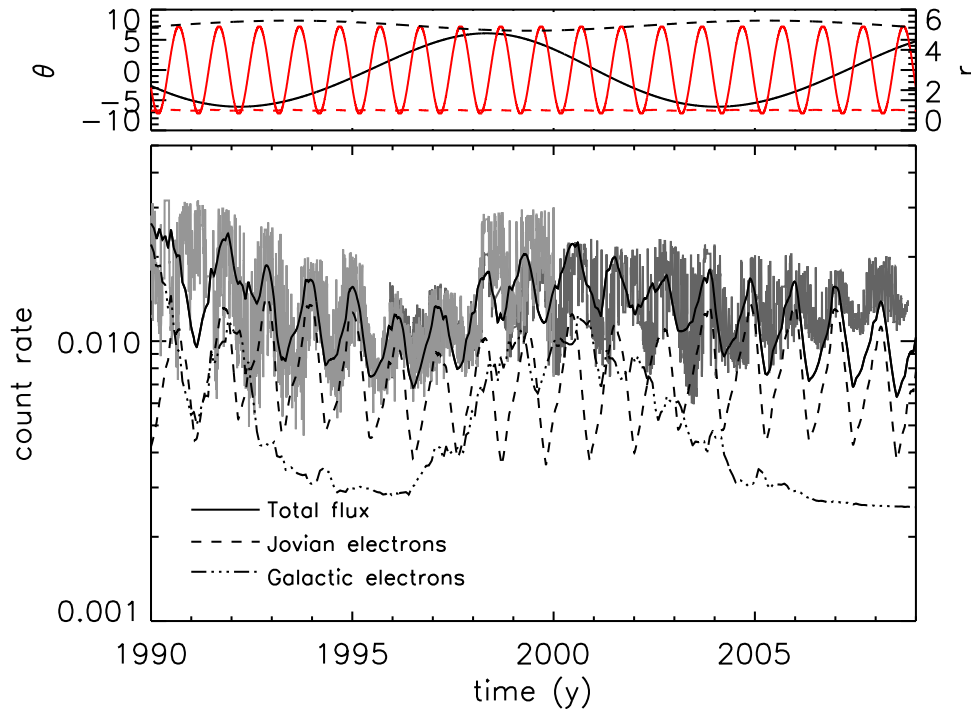


Figure 6.8: IMP-8 and SOHO/EPHIN measurements and the 7 MeV electron flux simulation for  $n = -1$ . The solid black line represents the total electron flux, while the dashed and the dash-dotted lines show the Jovian and galactic components, respectively. Parameters:  $u_{min} = 400$  km/s,  $u_{max} = 800$  km/s,  $v = 8$ ,  $g' = 0.075$ ,  $t_0^{(1)} = 1990.85$ ,  $t_0^{(2)} = 1996.12$ ,  $t_0^{(3)} = 2002.24$ .



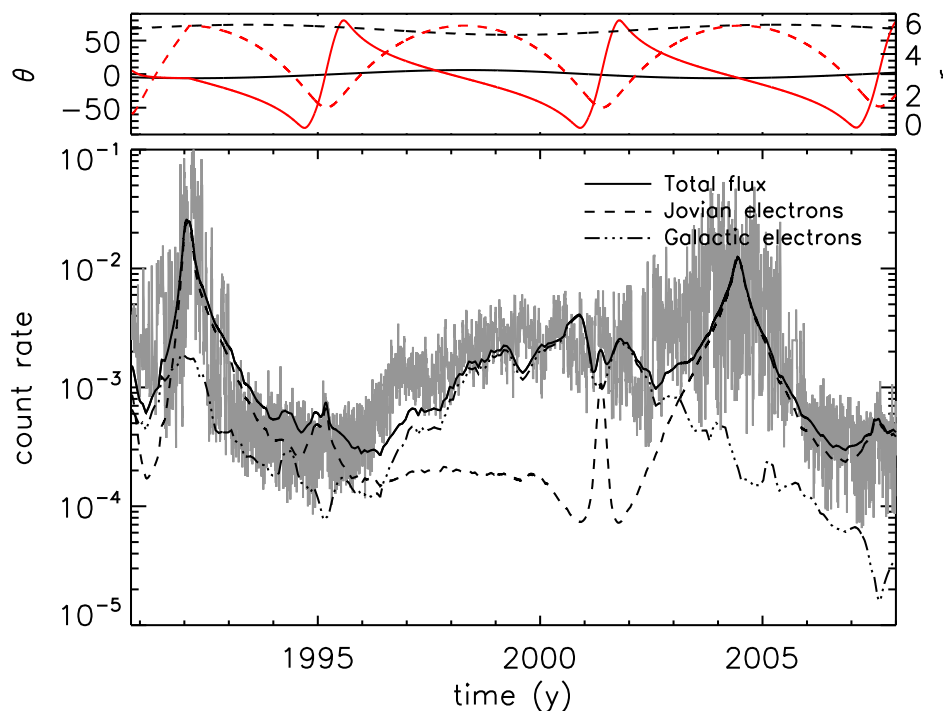


Figure 6.9: The same as Fig. 6.8, but for *Ulysses/KET*.

approaches the planet and reaches its maximum during the first encounter. The electron flux drops while *Ulysses* moves in latitude towards the heliographic south pole. A second lower maximum occurs when the spacecraft crosses the ecliptic after its first polar pass during the first fast latitude scan to stay on an almost constant level until the second south polar pass. The second FLS reveals a high peak in the Jovian electrons after which the electron flux rises again constantly until the second Jupiter encounter in 2004. The galactic electrons reveal a strong solar cycle dependence also along the *Ulysses* trajectory. From the beginning of the mission, the flux decreases to stay below the Jovian component during solar minimum conditions even over the solar poles. After 1996 the galactic electrons show the step-like increase, which is also seen in the *Ulysses/KET* measurements. During the solar maximum period, the galactic electron component exceeds the Jovians by up to one order of magnitude at all latitudes. The only exception is the second FLS, when both species are equally strong during the ecliptic crossing. The galactic component drops down slowly during the solar minimum after 2002 to reach its absolute minimum value in 2007. The simulation results for the 7 MeV electron flux along the *Ulysses* trajectory reveal that during solar minimum conditions the Jovian electrons do not only dominate the ecliptic in the inner heliosphere, but that the Jovian electrons are the most abundant electron component at all latitudes up to the heliographic poles. Additional investigation is

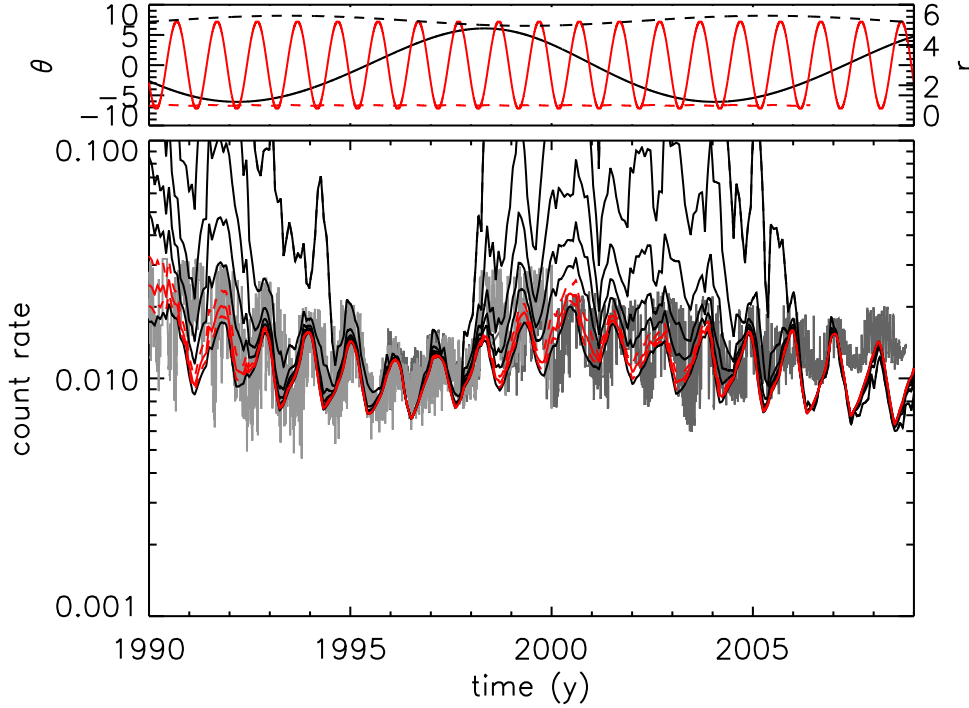


Figure 6.10: The same as Fig. 6.6, but with  $n = -\alpha/\alpha_0$ ,  $\alpha_0 \in [10^\circ, 20^\circ, 30^\circ, 40^\circ, 50^\circ, 60^\circ, 70^\circ, 80^\circ, 90^\circ]$  ordered from the lowest ( $\alpha_0 = 90^\circ$ ) to the highest ( $\alpha_0 = 10^\circ$ ) curve. Parameters:  $u_{min} = 400$  km/s,  $u_{max} = 800$  km/s,  $v = 8$ ,  $g' = 0.075$ ,  $t_0^{(1)} = 1990.85$ ,  $t_0^{(2)} = 1996.12$ ,  $t_0^{(3)} = 2002.24$ .

needed to explain the step-like increase in the electron count rate between 2006 and 2008. This effect is found in the simulation data for  $n = -1$ , but not as pronounced as it is seen in the data. As mentioned above, higher values of  $n$  lead to a closer fit to the data during that time period. Therefore, the variation of  $n$  during the solar cycle needs to be discussed.

Following an approach by Ferreira et al. (2003b), the exponent  $n$  is related to the tilt angle  $\alpha$  to account for the solar cycle dependence of  $n$ . The relation  $n = -\alpha/\alpha_0$  is tested for  $\alpha_0 \in [10^\circ, 20^\circ, 30^\circ, 40^\circ, 50^\circ, 60^\circ, 70^\circ, 80^\circ, 90^\circ]$ . The other parameters are kept as explained above. The results of these simulations are displayed in Fig. 6.10 for IMP-8 and SOHO/EPHIN ordered from the lowest ( $\alpha_0 = 90^\circ$ ) to the highest ( $\alpha_0 = 10^\circ$ ) curve. Similar to the simulations with constant values of  $n$ , the results of  $\alpha_0 \in [10^\circ, 20^\circ, 30^\circ, 40^\circ]$  (the four highest solid black lines) overestimate the electron count rates at the Earth's orbit during the solar maximum periods to a large extent. The results of  $\alpha_0 \in [50^\circ, 60^\circ, 70^\circ, 80^\circ, 90^\circ]$  define a narrow band. The solid red line ( $\alpha_0 = 70^\circ$ ) was chosen to be the closest to the IMP-8 and SOHO/EPHIN measurements and is discussed in detail below. The red dashed lines above ( $\alpha_0 = 60^\circ$ ) and below

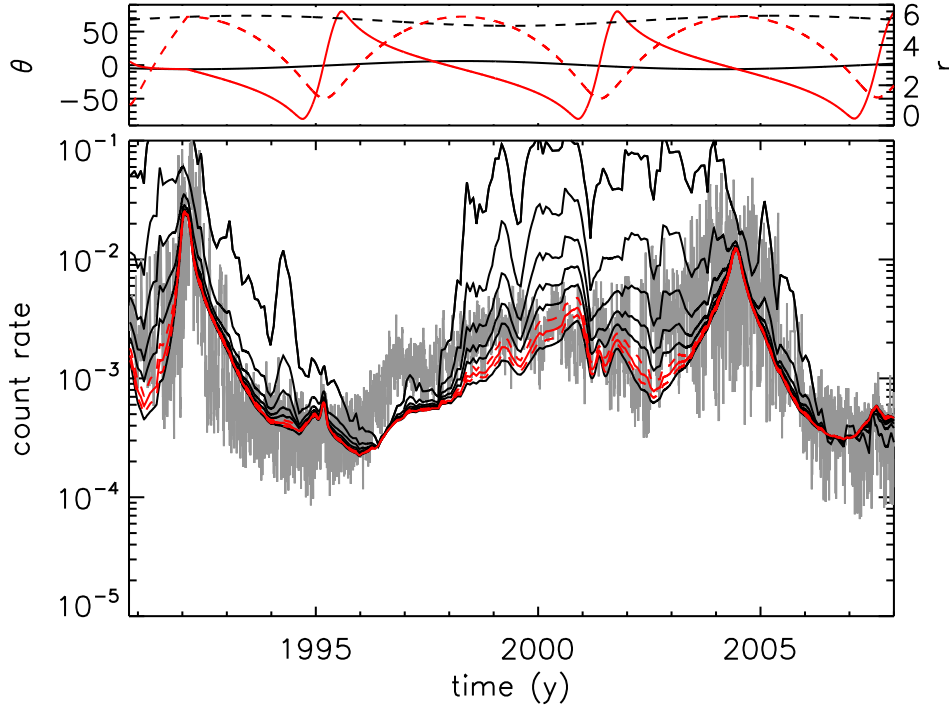


Figure 6.11: The same as Fig. 6.10, but for Ulysses/KET.

( $\alpha_0 = 80^\circ$ ) as well as the remaining two solid black lines ( $\alpha_0 = 50^\circ$  and  $\alpha_0 = 90^\circ$ ) appear to be close to the spacecraft data during most of the time. The effect that the different simulation results are hardly distinguishable in the comparison to Earth orbit measurements during the solar minimum phases can also be found for  $n = -\alpha/\alpha_0$  ( $(B_0/B)^n \approx 1$ ).

The comparison of the model results to the Ulysses/KET measurements is displayed in Fig. 6.11. The simulation data are ordered the same way as in Fig. 6.10 from  $\alpha_0 = 10^\circ$  (highest curve) to  $\alpha_0 = 90^\circ$  (lowest curve). The results for  $\alpha_0 \in [10^\circ, 20^\circ, 30^\circ]$  (solid black lines) overestimate the Ulysses data especially during the solar maximum periods. The remaining six curves show only little deviation and can, therefore, all be considered to be close to the data with the exception of the period from 1996 to 1999. During that time,  $\alpha_0 = 10^\circ$  and  $\alpha_0 = 20^\circ$  are the only values to explain the measured data. Considering the comparison to the IMP-8 and SOHO/EPHIN data,  $\alpha_0 = 70^\circ$  (solid red line) was also chosen as the best fit to the Ulysses/KET measurements and is discussed below. The neighbouring red dashed lines represent the values of  $\alpha_0 = 60^\circ$  for the higher and  $\alpha_0 = 80^\circ$  for the lower curve, respectively. From the Ulysses/KET comparison, not only  $\alpha_0 = 50^\circ$  and  $\alpha_0 = 90^\circ$  are very close to the data, but even the simulation with  $\alpha_0 = 40^\circ$  can explain the measurements as well.

Figures 6.12 and 6.13 display the comparison of the simulation results for  $n =$

$-\alpha/\alpha_0$ ,  $\alpha_0 = 70^\circ$ , to the IMP-8 and SOHO/EPHIN data and the Ulysses/KET data, respectively. In both Figures, the solid black line represents the total electron flux. The dashed line shows that of the Jovian electrons, while the dash-dotted line stands for the galactic component. Comparing the simulation data for  $\alpha_0 = 70^\circ$  (Fig. 6.12) to the results with a constant  $n = -1$  (Fig. 6.8), both results appear to be very similar. The Jovian electrons show their 13-months period and dominate the total electron flux, especially during the solar minimum phases. The galactic electrons underlie the same time dependence, resulting in a low fraction of the total electron flux during solar minimum conditions. During the solar maxima, however, the galactic electrons can enter the inner heliosphere more easily and dominate the electron flux at the Earth's orbit. A difference between the  $\alpha_0 = 70^\circ$  model and the  $n = -1$  model can be found in the dropping and rising phases of the galactic electron component from 1990 to 1993 and 1997 to 2000, respectively. The variation of  $n$  with the tilt angle leads to a slower decrease or increase of the flux compared to the simulation with a constant value of  $n$ .

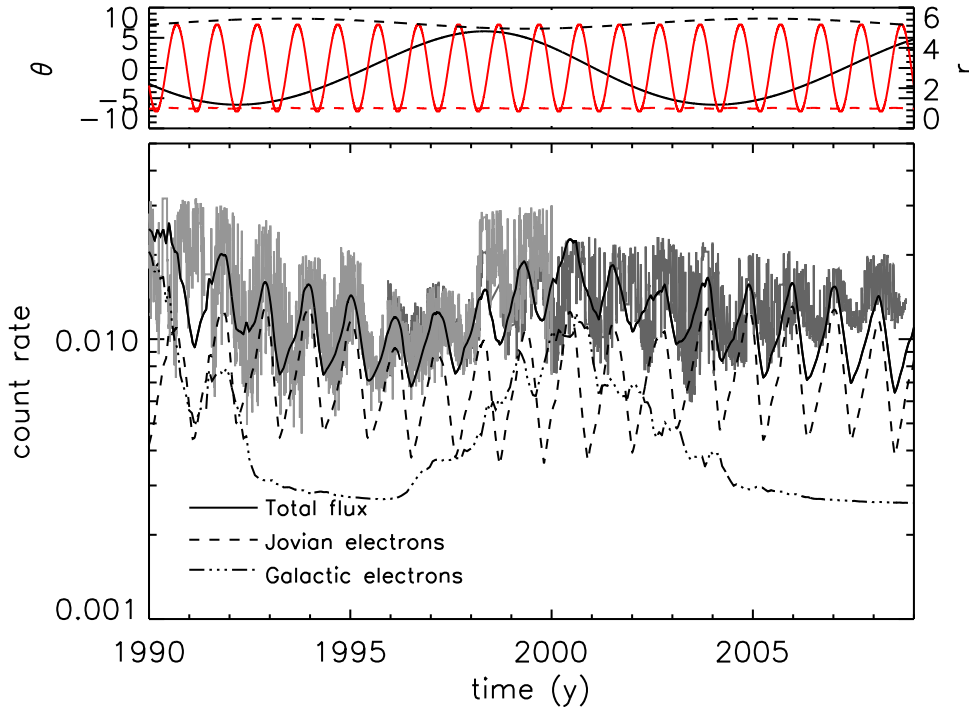


Figure 6.12: IMP-8 and SOHO/EPHIN measurements and the 7 MeV electron flux simulation for  $\alpha_0 = 70^\circ$ . The solid black line represents the total electron flux, while the dashed and the dash-dotted lines show the Jovian and galactic components, respectively. Parameters:  $u_{min} = 400$  km/s,  $u_{max} = 800$  km/s,  $v = 8$ ,  $g' = 0.075$ ,  $t_0^{(1)} = 1990.85$ ,  $t_0^{(2)} = 1996.12$ ,  $t_0^{(3)} = 2002.24$ .

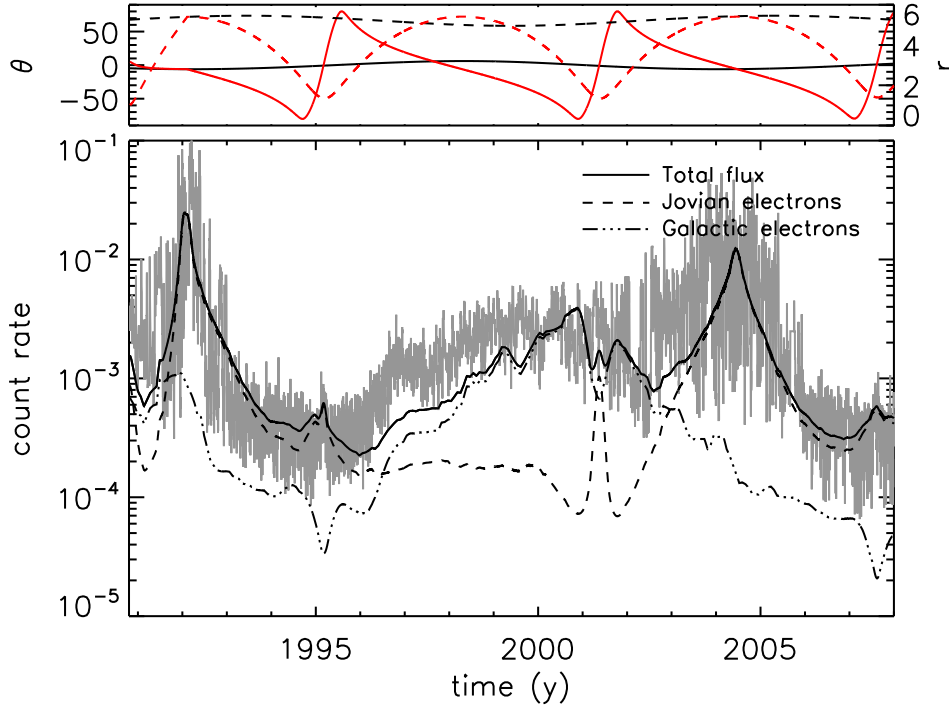


Figure 6.13: The same as Fig. 6.12, but for Ulysses/KET.

The simulation data with  $\alpha_0 = 70^\circ$  for the Ulysses trajectory shown in Fig. 6.13 also appear to be similar to the results with  $n = -1$  (Fig. 6.9). The Jovian electrons dominate the inner heliosphere up to high latitudes during the solar minimum phases, while the galactic electrons present the largest fraction of the total electron flux during solar maximum conditions with the exception of the ecliptic crossing of the second FLS. During the time period from 1996 to 1999, the electron flux behaves differently from the results shown in Fig. 6.9 with the galactic electron component rising more slowly for  $n = -\alpha/\alpha_0$ ,  $\alpha_0 = 70^\circ$ , than for  $n = -1$ , leading to a flattening of the step-like increase during that time. This effect was also observed in the IMP-8 and SOHO/EPHIN simulation data.

The explanation for the behaviour of the electron flux can be deduced from Fig. 6.14. The upper panel shows the HMF strength measured at the Earth's orbit (solid black line) and the tilt angle  $\alpha$  (solid red line). To guide the eye, the two model constants  $B_0 = 5$  nT (dashed black line) and  $\alpha_0 = 70^\circ$  (red dashed line) are added to the plot. From the tilt angle measurements, a variation of the exponent between  $n \approx -1/7$  and  $n \approx -1$  can be derived. The lower and middle panel display the simulation data for  $n = -\alpha/\alpha_0$ ,  $\alpha_0 = 70^\circ$ , from Figs. 6.12 and 6.13 (red line). For a comparison to the model with constant values of  $n$ , the values  $n = -1$  (higher black curve) and  $n = 0$  (lower black curve) were chosen from Fig. 6.6 and 6.7 due

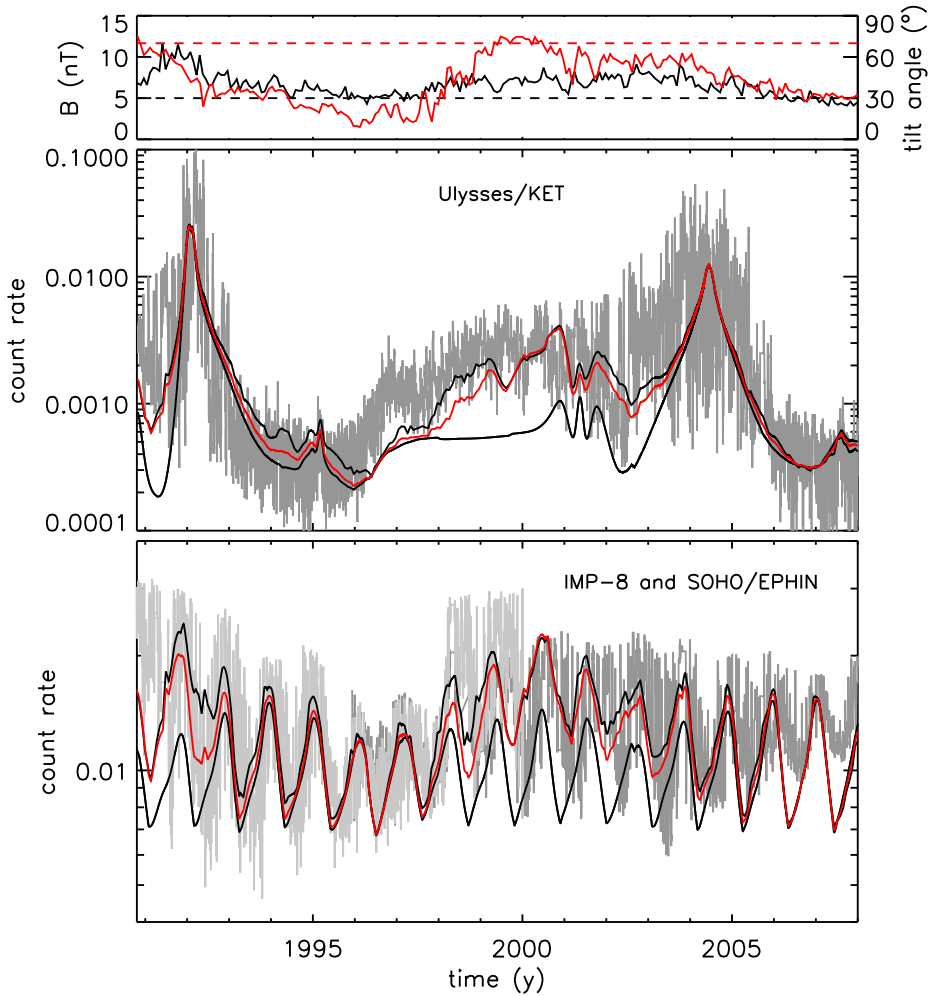


Figure 6.14: Comparison of the model results with varying  $n$  to simulations with constant values of  $n$ . The lower and middle panels compare the simulation for  $n = -\alpha/\alpha_0$ ,  $\alpha_0 = 70^\circ$ , from Figs. 6.12 and 6.13 (red line) to the results with  $n = -1$  (higher black line) and  $n = 0$  (lower black line) from Figs. 6.6 and 6.7. The upper panel displays the HMF strength measured at the Earth's orbit (solid black line) and the tilt angle (solid red line). The two horizontal lines are included to guide the eye at  $B_0 = 5$  nT (black dashed line) and  $\alpha_0 = 70^\circ$  (red dashed line).

to the variation of  $n$  deduced from the tilt angle measurements. For both, Ulysses and Earth orbit measurements, the simulation data for  $\alpha_0 = 70^\circ$  lie between the two black curves for  $n = -1$  and  $n = 0$ , varying between them according to the tilt angle measurements. This leads to a better fit to the measured data with the exception of the time period between 1996 and 1999, as well as the SOHO/EPHIN measurements after 2005. From 1996 to 1999 the tilt angle lies below  $30^\circ$ . Therefore,

the low values of  $n$  lead the simulation data of  $\alpha_0 = 70^\circ$  to be close to the  $n = 0$  curve. This causes the slow increase of the electron flux observed in the model data during that time period. From Fig. 6.13 it was already concluded that the model results for  $n \in [-2, -2.5, -3]$  provide better data fits between 1996 and 1998. Hence, it can be concluded that the simulations for the particle transport with the approach  $\kappa_{\parallel} \propto (B_0/B)^n$  and  $n = -\alpha/\alpha_0$  can explain the electron count rates along the Earth's and Ulysses' trajectories, but underestimate the impact of the magnetic field strength on the particle propagation between 1996 and 1999. Additional investigation is needed to gain a deeper insight into the transport parameters during that time period.

## Varying the Solar Cycle Parameters

To achieve a better agreement of model and measurements, the 7 MeV electron flux is investigated regarding its time dependence with different parameters describing the solar cycle. The solar cycle phases and transitions used in this study are displayed in Fig. 6.15. The solid black line represents the sunspot number from 1988 to 2009 (similar to Fig. 2.2). The dashed red line indicates the solar cycle phases and transitions applied to the model. In contrast to the study discussed above, the parameter  $g'$  describing the transition time from solar minimum to solar maximum and back is chosen to  $g' = 3/32$ , which corresponds to a period of 1.36 years. The solar cycle transitions were set to  $t_0^{(1)} = 1990.85$  (solar maximum to minimum),  $t_0^{(2)} = 1995.84$

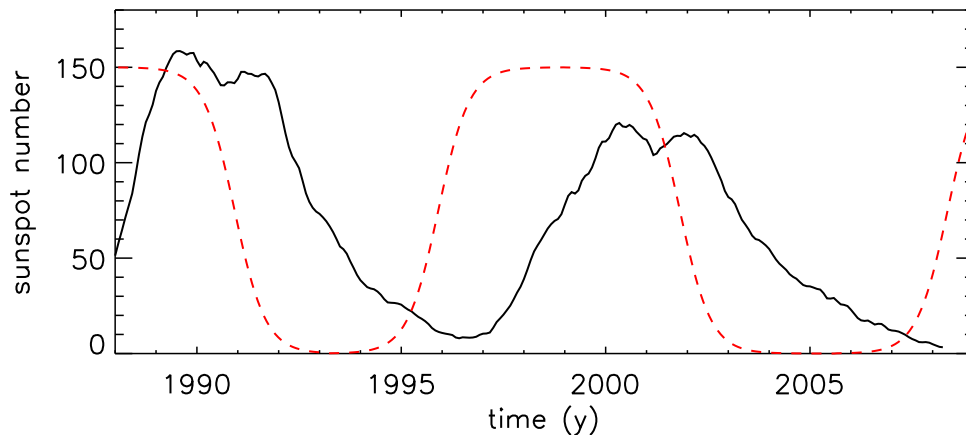


*Figure 6.15: The solar cycle dependence employed in the present simulation. This graph displays the sunspot number number from 1988 to 2009 (black solid line). Additionally, the red dashed line shows the solar cycle as it is employed in the simulations presented below. Note that the red dashed line does not indicate the sunspot number, but the phases of the solar cycle and the transitions in between.*

parameter	before	this study
$t_0^{(1)}$ (maximum $\rightarrow$ minimum)	1990.85	1990.85
$t_0^{(2)}$ (minimum $\rightarrow$ maximum)	1996.12	1995.84
$t_0^{(3)}$ (maximum $\rightarrow$ minimum)	2002.24	2001.75
$t_0^{(4)}$ (minimum $\rightarrow$ maximum)	—	2008.30
$g'$ (transition time)	0.075	3/32
enhancement of $\kappa_{\perp r}$	25%	35%

Table 6.1: A comparison of the solar cycle parameters used in this study and those used in the study before.

(back to solar maximum) and  $t_0^{(3)} = 2001.75$  (back to solar minimum). An additional transition back to solar maximum at  $t_0^{(4)} = 2008.30$  is needed to fit the Ulysses/KET measurements of the 2.5 – 7 MeV electron count rate.

In addition, the radial diffusion coefficient  $\kappa_{\perp r}$  is enhanced by 35% during solar maximum conditions, not only raising the electron transport into the inner heliosphere, but also increasing the electron flux in the outer heliosphere. From a comparison of model computations to Pioneer 10 measurements up to 70 AU, Ferreira (2002) deduced that the enhancement of  $\kappa_{\perp r}$  must not exceed 35% to fit the simulation data to measurements in the inner and outer heliosphere. The solar cycle parameters applied to the simulation in this investigation are compared to those used in the study discussed above in Table 6.1.

The simulations of the 7 MeV electron flux are tested with  $\kappa_{\parallel} \propto (B_0/B)^n$  and constant values of  $n \in [0, -0.5, -1, -1.5, -2, -2.5, -3]$ . The model results are compared to IMP-8 and SOHO/EPHIN data in Fig. 6.16. The values  $n = 0$  and  $n = -3$  predict the lowest and highest curves, respectively, until 2007, while the other results are ordered accordingly in between. After 2007, the lines reverse their order. The simulations with  $n \in [-1.5, -2, -2.5, -3]$  (black solid lines) overestimate the electron count rate to a large extent during solar maximum conditions, and the 13-months period caused by the Jovian electrons almost vanishes. The solid red line ( $n = -0.5$ ) was chosen as the best data fit in this investigation. A detailed discussion of this result as well as the Ulysses/KET comparison is omitted here, because it corresponds to the discussion of the study presented above (see pp. 67ff., Fig. 6.8 and Fig. 6.9). The upper and lower limits for the exponent  $n$  were chosen to  $n = 0$  and  $n = -1$ , respectively. This corresponds to the investigation of the tilt angle dependence of  $n$  presented above, where  $n$  was found to vary between 0 and  $-1$  due to the choice of the normalisation factor,  $\alpha_0 = 70^\circ$ . During solar minimum periods the different models are hardly distinguishable, because the magnetic field strength measured at the Earth’s orbit is in the range of 5 nT. Therefore, the function  $f_2(t) = (B_0/B)^n$  describing the impact of the magnetic field strength on the particle diffusion becomes unity independent of the exponent  $n$ . The period after 2005 can still not be explained by the current model



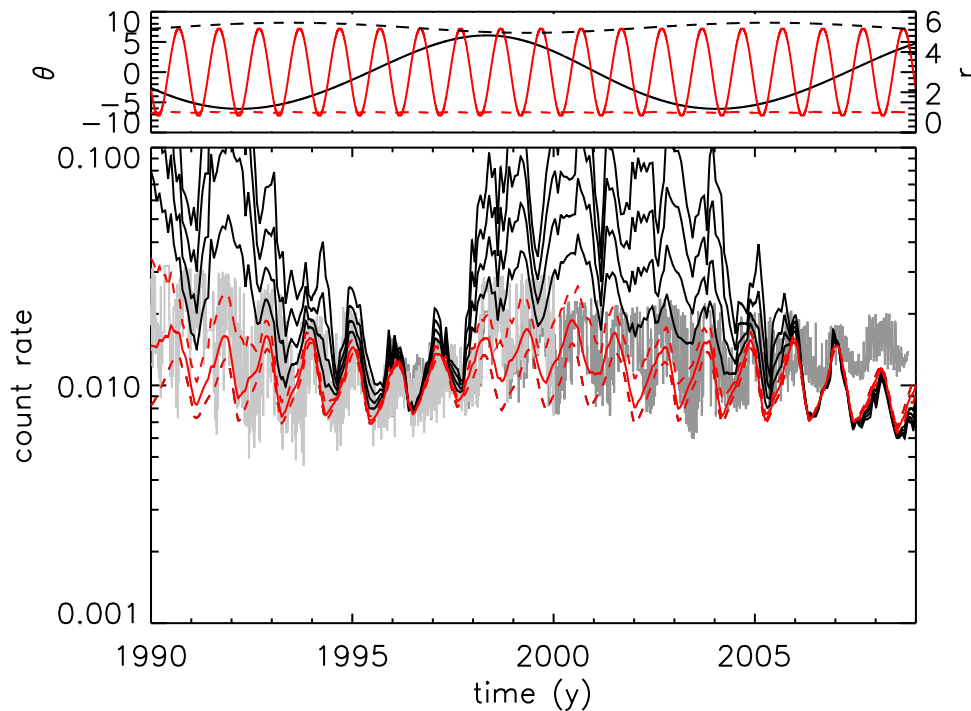


Figure 6.16: The same as Fig. 6.6, but for the parameters  $u_{min} = 400$  km/s,  $u_{max} = 800$  km/s,  $v = 8$ ,  $g' = 3/32$ ,  $t_0^{(1)} = 1990.85$ ,  $t_0^{(2)} = 1995.84$ ,  $t_0^{(3)} = 2001.75$ ,  $t_0^{(4)} = 2008.30$ . Note that a different exponent  $n$  was chosen as the best data fit in this study. The investigation presented above suggested  $n = -1$ , while  $n = -0.5$  leads to the best results here. A detailed discussion of the  $n = -0.5$  curve is omitted here, because it corresponds to the discussion of the study presented above (see pp. 67ff. and Fig. 6.8).

and needs further investigation to gain a deeper insight into the factors leading to the measured count rates. Note that a different exponent  $n$  was chosen as the best data fit in this study. The investigation presented above suggested  $n = -1$ , while  $n = -0.5$  leads to the best results here.

The simulation data for the 7 MeV electron flux along the Ulysses trajectory are displayed in Fig. 6.17. In contrast to the study above, the Ulysses/KET count rate is taken into account until 2009 here. A second step-like increase similar to 1996/97 appears in 2008. As in Fig. 6.16,  $n = 0$  and  $n = -3$  result in the lowest and highest electron flux, respectively, while the other lines are ordered accordingly in between. The reversal of this order in 2007 becomes more obvious in the Ulysses model data. Until that time, the values  $n \in [-1.5, -2, -2.5, -3]$  (solid black lines) lead to an overestimation of the count rate. In 2007, these results drop below the measurements. As for IMP-8 and SOHO/EPHIN, the best fit to the measurements was chosen to

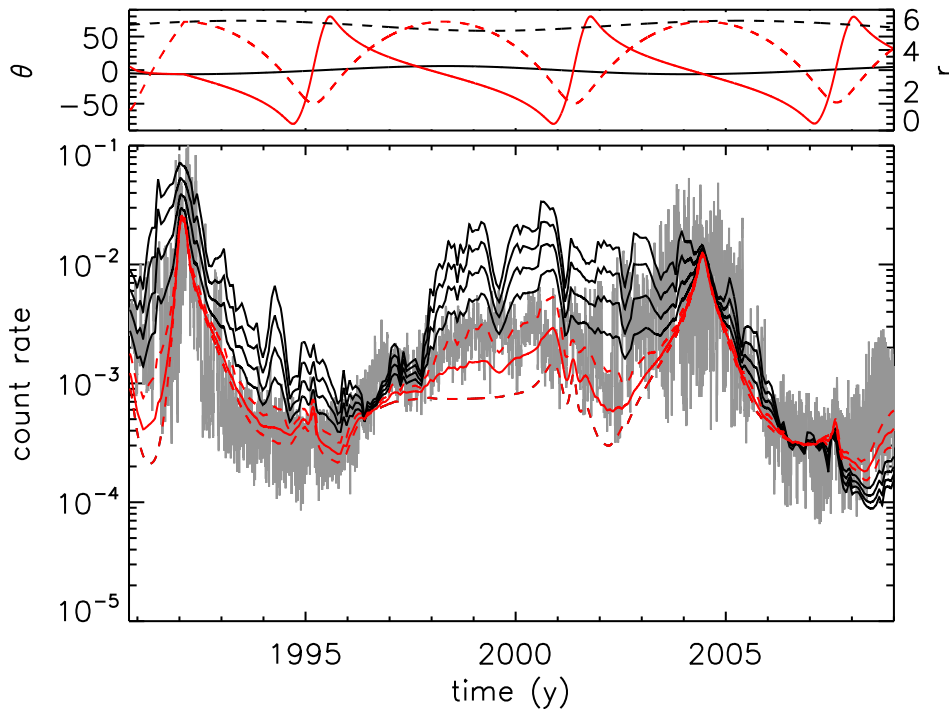


Figure 6.17: The same as Fig. 6.16, but for Ulysses/KET. A detailed discussion of the  $n = -0.5$  curve is omitted here, because it corresponds to the discussion of the study presented above (see pp. 67ff. and Fig. 6.9).

$n = -0.5$  (solid red line) with the upper and lower limits  $n = -1$  and  $n = 0$  (red dashed lines), respectively.

In comparison to the investigation presented above (Fig. 6.6 and 6.7), the new solar cycle parameters lead to a better agreement between the model and the measured count rates. Especially the fit of the step-like increase of the electron data in 1996/96 is improved. To reproduce the second increase in 2008, an additional transition from solar minimum to solar maximum conditions is needed. This is, however, not observed in any other data describing the solar cycle phase. Although the new solar cycle parameters lead to a better fit to the Ulysses/KET measurements, a higher value of  $n$  ( $n = -1.5$  or  $n = -2$ ) during 1997 would result in a better agreement than the chosen range of  $n$ .

The solar cycle dependence of  $n$  according to the approach by Ferreira et al. (2003b) with  $n = -\alpha/\alpha_0$  is tested for  $\alpha_0 \in [10^\circ, 20^\circ, 30^\circ, 40^\circ, 50^\circ, 60^\circ, 70^\circ, 80^\circ, 90^\circ]$ . The simulation results along the IMP-8 and SOHO trajectories are presented in Fig. 6.18 with  $\alpha_0 = 90^\circ$  and  $\alpha_0 = 10^\circ$  yielding the lowest and highest curves, respectively, and the others ordering accordingly. As in the study for constant values of  $n$ , the order reverses in 2007. For the values  $\alpha_0 \in [10^\circ, 20^\circ, 30^\circ, 40^\circ, 50^\circ]$  (solid black lines), the

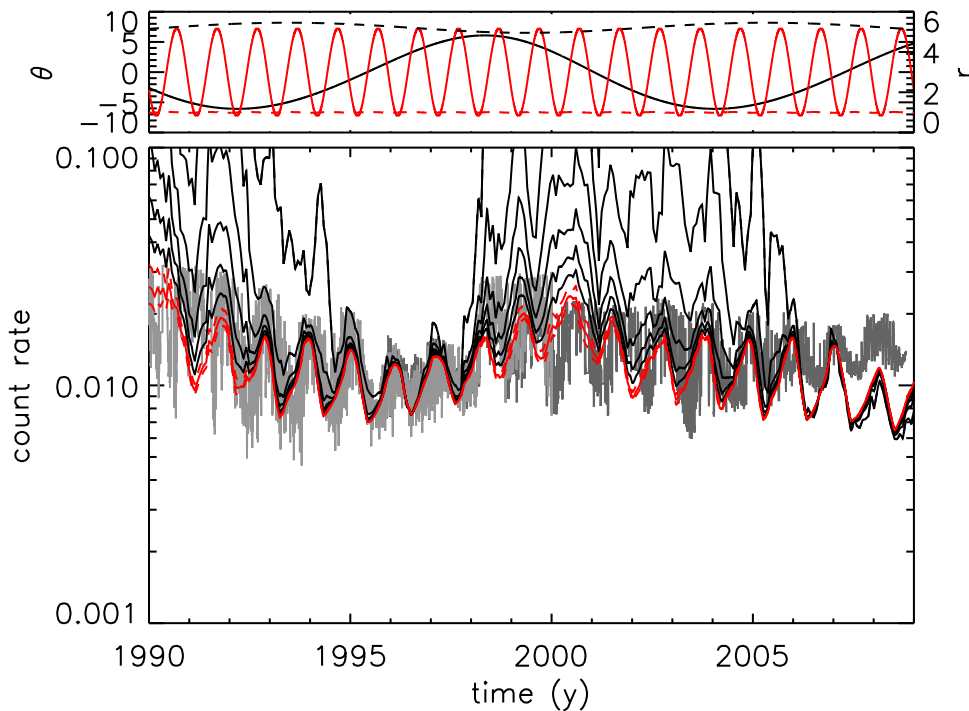


Figure 6.18: The same as Fig. 6.10, but for the parameters  $u_{min} = 400$  km/s,  $u_{max} = 800$  km/s,  $v = 8$ ,  $g' = 3/32$ ,  $t_0^{(1)} = 1990.85$ ,  $t_0^{(2)} = 1995.84$ ,  $t_0^{(3)} = 2001.75$ ,  $t_0^{(4)} = 2008.30$ . A detailed discussion of the  $\alpha_0 = 80^\circ$  curve is omitted here, because it corresponds to the discussion of the study presented above (see pp. 71ff. and Fig. 6.12).

electron count rate is overestimated during the solar maximum periods. The results of  $\alpha_0 = 80^\circ$  (solid red line) were chosen as the closest fit to the data. A detailed discussion would be similar to the discussion of the investigation presented above (see pp. 71ff., Fig. 6.12 and Fig. 6.13). Therefore, it is omitted here as well as for the Ulysses/KET data comparison. The upper and lower limits are given by  $\alpha_0 = 70^\circ$  and  $\alpha_0 = 90^\circ$ , respectively, while the value  $\alpha_0 = 60^\circ$  is also found to give simulation results very close to the measured count rate. During the solar minimum phases, the models are hardly distinguishable ( $B_0/B \approx 1$ ).

The comparison of these simulation results for Ulysses/KET is shown in Fig. 6.19. The data is ordered the same way as in Fig. 6.18 with  $\alpha_0 = 10^\circ$  yielding the highest curve and  $\alpha_0 = 90^\circ$  resulting in the lowest curve, until the order reverses in 2007. The other lines are ordered accordingly in between. For Ulysses/KET, only  $\alpha_0 \in [10^\circ, 20^\circ, 30^\circ]$  overestimate the measured count rate to a large extent during solar maximum conditions. The six remaining curves can be considered to be able to explain the electron count rate with the exception of the step-like increase in 1996/97. There,

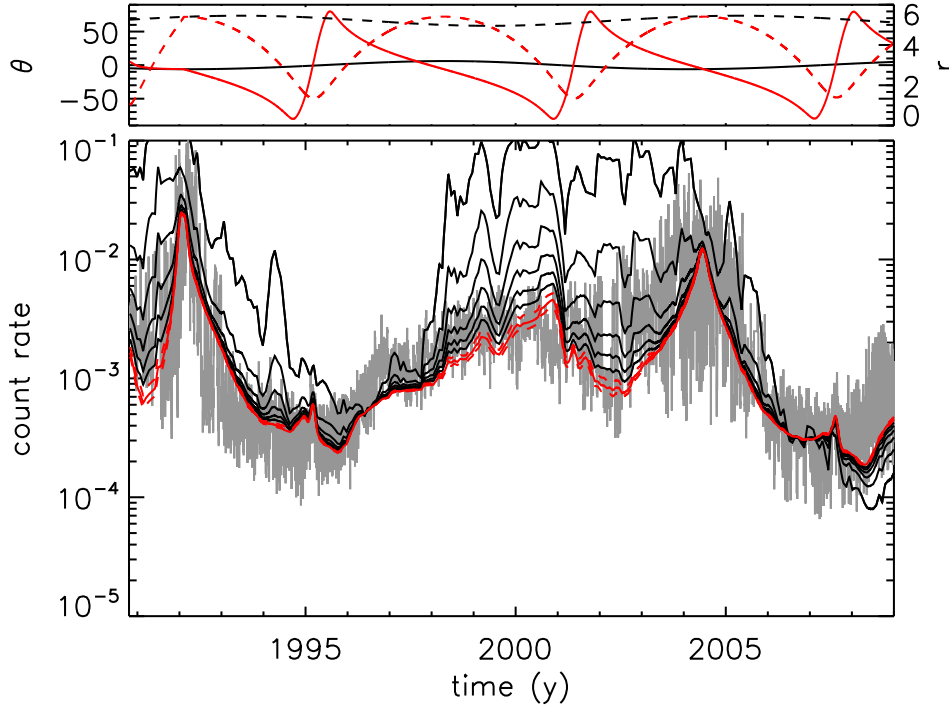


Figure 6.19: The same as Fig. 6.18, but for Ulysses/KET. A detailed discussion of the  $\alpha_0 = 80^\circ$  curve is omitted here, because it corresponds to the discussion of the study presented above (see pp. 71ff. and Fig. 6.13).

only the  $\alpha_0 = 10^\circ$  simulation can reproduce the measurements. The simulation with  $\alpha_0 = 80^\circ$  was chosen as the best data fit with  $\alpha_0 = 90^\circ$  and  $\alpha_0 = 70^\circ$  as the lower and upper limits, respectively. The values  $\alpha_0 \in [40^\circ, 50^\circ, 60^\circ]$ , which are also close to the measurements, can be excluded employing the IMP-8 and SOHO/EPHIN comparison as well as the results from Fig. 6.16 and 6.17, that  $n$  varies between 0 and 1.

A comparison of the  $\alpha_0 = 80^\circ$ , the  $n = 0$  and the  $n = -1$  simulations is presented in detail in Fig. 6.20. The upper panel displays the magnetic field strength  $B$  measured at the Earth's orbit (solid black line) and the tilt angle  $\alpha$  (solid red line). The two normalisation factors  $B_0$  and  $\alpha_0$  are indicated by the black and red dashed lines, respectively. The middle and lower panels show the simulation results for the Ulysses/KET and IMP-8 and SOHO/EPHIN electron flux, respectively. In both panels, the red lines represent the result from the  $n = \alpha/\alpha_0$  simulation with  $\alpha_0 = 80^\circ$ . This is compared to the simulations with constant values of  $n$ . Until 2007, the upper and lower black lines represent the  $n = -1$  and  $n = 0$  results, respectively. These two lines reverse their order in 2007. As in Fig. 6.14, the red line varies between the two black lines, corresponding to the tilt angle variation. The value  $\alpha_0 = 80^\circ$  leads to a variation of  $n$  between 0 and  $-1$ . The tilt angle leads the  $\alpha_0 = 80^\circ$  line to be close

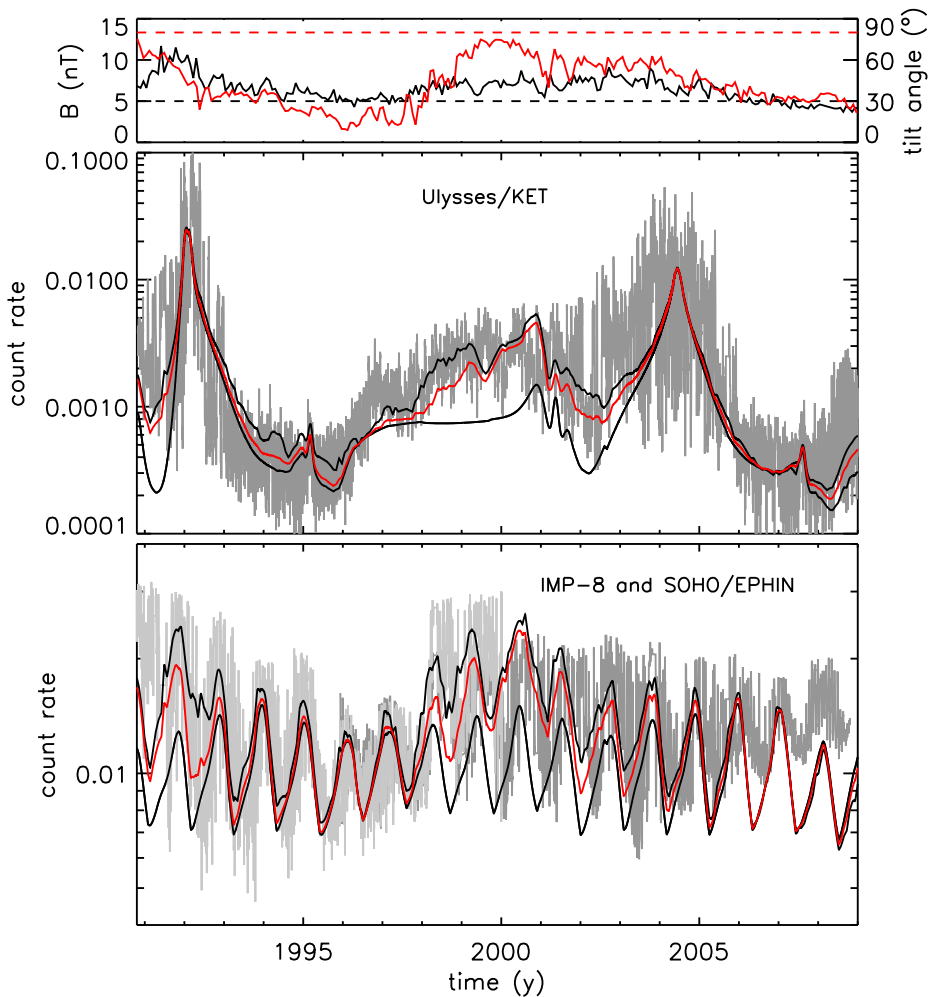


Figure 6.20: Comparison of the model results with varying  $n$  to simulations with constant values of  $n$ . The lower and middle panels compare the simulation for  $n = -\alpha/\alpha_0$ ,  $\alpha_0 = 80^\circ$ , from Fig. 6.18 and 6.19 (red line) to the results with  $n = -1$  (higher black line) and  $n = 0$  (lower black line) from Fig. 6.16 and 6.17. The upper panel displays the HMF strength measured at the Earth's orbit (solid black line) and the tilt angle (solid red line). The two horizontal lines are included to guide the eye at  $B_0 = 5$  nT (black dashed line) and  $\alpha_0 = 80^\circ$  (red dashed line).

to the  $n = 0$  result during the solar minimum phases, while it follows the  $n = -1$  curve during solar maximum conditions.

In comparison to Fig. 6.14, an improvement of the simulation results becomes visible. The new solar cycle parameters lead to a better agreement between the simulation results and the measurements. In contrast to the study presented above, the range of the exponent  $-1 < n < 0$  found in Fig. 6.18 and 6.19 corresponds to the results of the

tilt angle investigation. However, the increases in the Ulysses/KET data in 1996/97 and 2008 still need additional investigation. In 1996/97, the models with the constant exponents  $n = -1.5$  and  $n = -2$  (see Fig. 6.17) lead to a better fit to the measured data. For the second increase in 2008, an additional transition from solar minimum to solar maximum is needed to reproduce the measured data. This is, however, not seen in any data describing the solar cycle.

## Conclusions

For the first time, the compound approach suggested by Ferreira et al. (2003b) was tested in time-dependent simulations of the 7 MeV electron flux in the heliosphere, relating the parallel diffusion coefficient  $\kappa_{\parallel}$  to the HMF strength measured at the Earth's orbit. A comparison to the corresponding count rates measured with the IMP-8, SOHO and Ulysses spacecraft reveals a good agreement of the model computations and the measured data. The results found in this chapter are consistent with the findings of, e.g., Ferreira et al. (2003a) and Ferreira and Potgieter (2004) who tested the compound approach for electrons and protons with a rigidity of 2.5 GV and electrons and helium with a rigidity of 1.2 GV to be conform to the corresponding particle count rates measured by different spacecraft. Ferreira et al. (2001) and Ferreira et al. (2003c) computed intensities of few-MeV electrons along the Ulysses trajectory applying their steady state model without the compound approach. Their findings are also consistent with the results of this work to a large extent.

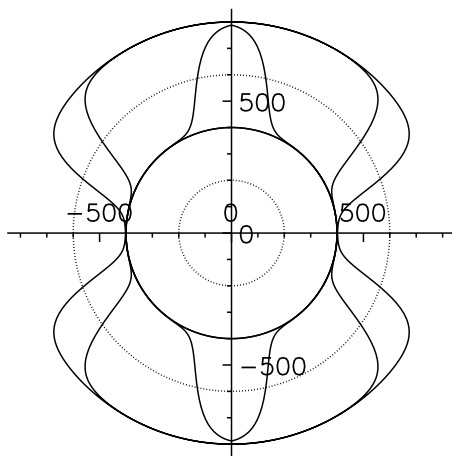


Figure 6.21: The same as the right panel of Fig. 4.6.

The perpendicular diffusion coefficients  $\kappa_{\perp r}$  and  $\kappa_{\perp \theta}$  are related to  $\kappa_{\parallel}$ . To achieve a good fit of the 7 MeV electron flux simulations to the IMP-8, SOHO and Ulysses count rates, both perpendicular coefficients are varied depending on the solar cycle, see also Ferreira (2002) and Lange (2004). While  $\kappa_{\perp \theta}$  is enhanced by a factor of eight in the fast solar wind during solar minimum conditions,  $\kappa_{\perp r}$  is increased globally by 35% during the solar maximum periods. This anti-correlated behaviour has also been reported e.g. by Ferreira et al. (2001b) and Lange et al. (2006).

Two models describing the time-evolution of the polar coronal holes and, therefore, the parameters  $\kappa_{\perp \theta}$  and  $u_{SW}$  in the PCH were tested in the model and discussed. From a comparison to Ulysses data, the second model (see Fig. 6.21) was

chosen to be the most appropriate description of this development. Note that Lange et al. (2006) employ the first model in their simulations. Additionally, a time shift of the  $\kappa_{\perp r}$ ,  $\kappa_{\perp \theta}$  and  $u_{SW}$  variations with respect to the sunspot cycle was deduced.

For the first time it was shown that transitions from solar maximum to minimum conditions around  $t_0^{(1)} = 1990.85$ , back to solar minimum conditions around  $t_0^{(2)} = 1995.84$ , again to solar minimum around  $t_0^{(3)} = 2001.75$  and from minimum to maximum conditions around  $t_0^{(4)} = 2008.30$  as well as a transition time of 1.36 years are needed to reproduce the electron count rates measured by IMP-8, SOHO/EPHIN and Ulysses/KET in model computations. Lange et al. (2006) employed only one transition from solar minimum to maximum conditions around  $t_0 = 1995.8$ , but found the same transition time in their simulations of the 7 MeV electron flux. Recently, Jiang et al. (2010) developed a new model computing the time variation of the tilt angle. In their investigation they find the tilt angle to increase earlier than predicted by older models, which would be consistent with the time shift found in the results of this study.

According to the compound approach, the parallel diffusion coefficient is related to the HMF strength measured at the Earth's orbit and  $\kappa_{\parallel} \propto (B_0/B)^n$ . Simulations for constant values of the exponent  $n$  reveal that  $n$  varies between 0 and  $-1$  during the solar cycle for 7 MeV electrons. This result was confirmed in the investigation with a time dependence  $n$ , relating  $n$  to the tilt angle  $\alpha$  employing the relation  $n = -\alpha/\alpha_0$ . Here,  $\alpha_0 = 80^\circ$  was found to lead to the best fit to all spacecraft data. However, the solar cycle dependence of  $n$  for 7 MeV electrons still needs additional investigation, because the increase in the Ulysses/KET electron count rate in 1996/97 can only be reproduced with  $n < -1$ . Note that Ferreira et al. (2003a) and Ferreira and Potgieter (2004) use positive values of  $n$  for high energy particles, while this work employs negative values of  $n$  for low energy electrons consistent with the findings of Engelbrecht and Burger (2010).

Lange et al. (2006) and Lange and Fichtner (2008) give two possible explanations for the high electron count rate measured by the Ulysses spacecraft between 1998 and the second Jupiter encounter. While Lange et al. (2006) suggest a variation of the Jovian source up to a factor of eight, Lange and Fichtner (2008) put forward the question, whether there are Kronian electrons inside the heliosphere, in addition to the well-known Jovian electrons. Assuming the Kronian magnetosphere (Saturn's magnetosphere) as a second planetary electron source, they can explain the high electron count rate found by Ulysses at least for low energies ( $\leq 2$  MeV). This work, however, shows for the first time that the Ulysses/KET electron count rate can be reproduced without varying the Jovian source strength or assuming additional planetary electron sources. Here, the variation of  $\kappa_{\parallel}$  proportional to the HMF strength measured at the Earth's orbit, as assumed in the compound approach, leads to an agreement of the simulation data and the measured electron count rate.





# Chapter 7

## A theoretical Study of the Electron Propagation in a Fisk-type HMF

Fisk (1996) proposed an alternative HMF model to explain the Ulysses measurements during solar minimum conditions. Following this new theory, Schwadron and McComas (2003), Burger and Hitge (2004), Burger et al. (2008) and Hitge and Burger (2010) elaborated different refinements of the Fisk field taking into account more realistic properties of the coronal magnetic field and the solar wind (see chapter 3). The Schwadron-Parker hybrid HMF model (Hitge and Burger, 2010) was chosen here as the most adequate analytic expression of a Fisk-type field for the investigation of the 7 MeV electron behaviour on short time scales ( $< 26$  days) during solar minimum conditions. The results of this study are presented in this chapter.

### The Electron Flux in a Schwadron-Parker HMF

The analytic expression of the Schwadron-Parker HMF model is given by equation (3.28). Its influence on the diffusion tensor is discussed in chapter 4. The latitudinal dependence of the diffusion tensor  $\hat{\kappa}$  in spherical polar coordinates is shown in Fig. 4.12 in a frame corotating with the solar equator. Therefore, a time-dependent behaviour of the transport parameters in an observer's rest frame and, consequently, 26-day variations of the electron count rate at mid to high latitudes are expected from the influence of a Fisk-type HMF. To test this theory, the time-dependent behaviour of the 7 MeV electron count rate is investigated on time scales shorter than the solar rotation. In this study the same diffusion coefficients as in chapter 6 are used, see equations (4.19) and (4.23). In contrast to the investigation of the particle propagation in a Parker field, the impact of the HMF strength on  $\kappa_{\parallel}$  is neglected and  $f_2(t)$  is set to unity to obtain the possibility of studying only the impact of the HMF structure. Additionally, no enhancement of  $\kappa_{\perp\theta}$  is assumed at high latitudes ( $v = 1$ ). For the study of the particle flux behaviour on short time scales, the time step was set to  $\Delta t = 0.13$  d and Jupiter was kept at a fixed position in the ecliptic. The parameters

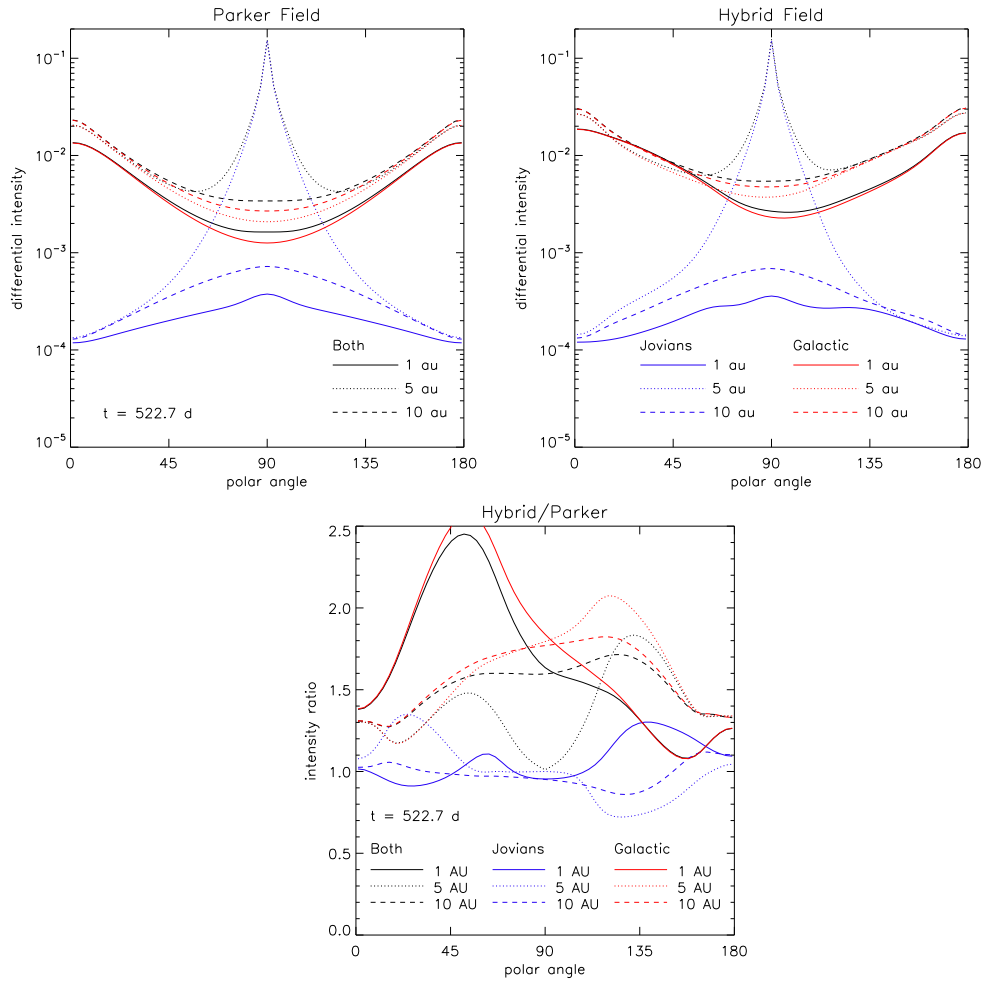


Figure 7.1: A comparison of latitudinal profiles of the 7 MeV electron intensity in the Parker HMF (top left panel) and the Schwadron-Parker hybrid HMF (top right panel) at Jupiter’s heliographic longitude. The bottom panel shows the electron intensity ratios of the hybrid field to the Parker field. The black lines represent the total intensity, the blue lines show the Jovian electrons and the red lines display the galactic electrons. The data was evaluated at the distances 1 AU (solid lines), 5 AU (dotted lines) and 10 AU (dashed lines) at a fixed time.

required for the Schwadron-Parker field are taken from Fig. 3.15 for solar minimum conditions. Note that this work presents a qualitative study. The diffusion coefficients will have to be adjusted to reproduce the Ulysses/KET count rates quantitatively.

Figure 7.1 compares the latitudinal profiles of the electron intensity expected in a Parker HMF (top left panel) and a Schwadron-Parker HMF (top right panel) at Jupiter’s heliographic longitude and presents the corresponding intensity ratios in the bottom panel. The three distances 1 AU (solid lines), 5 AU (dotted lines) and 10 AU

(dashed lines) to the Sun were chosen for the comparison. The two top panels show similar results. The galactic electrons (red lines) dominate the inner heliosphere around the ecliptic and at high latitudes. The Jovian electrons (blue lines) only provide the largest fraction of the total intensity (black lines) around the ecliptic plane at 5 AU, leading to an intensity peak around Jupiter's position. Note that this is in contrast to the results found in the simulation of the solar cycle dependence of the electron count rate (see chapter 6). This is a consequence of the latitudinal diffusion coefficient  $\kappa_{\perp\theta}$  not being enhanced ( $v = 1$ ) in this study for comparative reasons. The treatment of the perpendicular diffusion coefficients in a Fisk-type HMF model to reproduce Ulysses measurements is a complex topic due to the field line structure. This is, however, not the goal of this investigation. Therefore, the same set of diffusion coefficients is employed in both HMF models to keep the results comparable. This leads to electron intensities dominated by galactic electrons in the inner heliosphere,

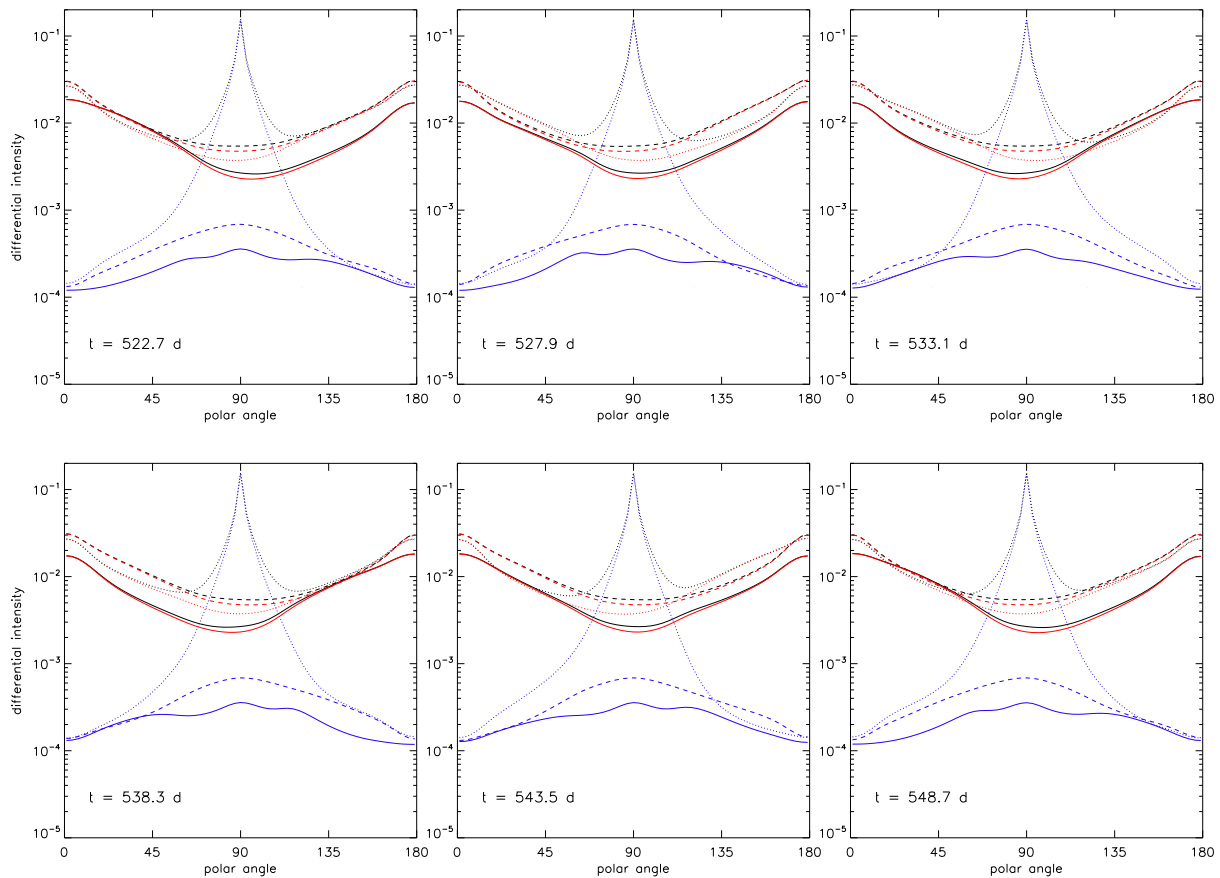
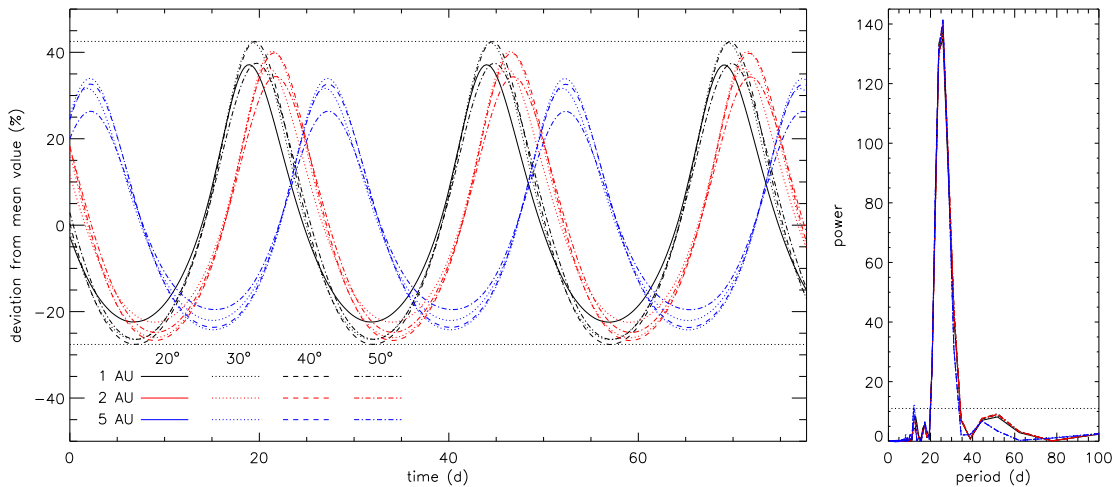


Figure 7.2: A time series of six latitudinal profiles of the 7 MeV electron intensity in the Schwadron-Parker HMF model equally spaced in time and covering a period of 26 days. This Figure employs the same colours and line styles as Fig. 7.1.

similar to solar maximum conditions. The reproduction of the Ulysses measurements will need additional investigation of perpendicular diffusion in a Fisk-type HMF.

Comparing the top left and right panels of Fig. 7.1, the electron intensities are symmetric with respect to the ecliptic ( $90^\circ$ ) in the Parker field, while they show a noticeable asymmetry in the hybrid field due to the field structure. This can also be found in the ratios shown in the bottom panel. At almost all positions considered in this comparison, the hybrid HMF predicts higher electron intensities than the Parker HMF, mainly caused by a higher inflow of galactic electrons. A clear asymmetry of the intensities can be found at all three distances with the electron intensity being higher in the northern hemisphere at 1 AU than in the southern hemisphere. The complex influence of the Schwadron-Parker HMF model becomes evident when this asymmetry changes at larger distances. At 5 AU and 10 AU, the intensity is higher in the southern hemisphere.

As the diffusion coefficients in the spherical polar coordinate system change with time and, like the Schwadron-Parker HMF model itself, show a point symmetry with respect to the coordinate system origin, this behaviour is expected to be transferred to the electron intensities. Figure 7.2 displays a time series of six latitudinal profiles of the 7 MeV electron intensities in the Schwadron-Parker HMF model equally spaced



*Figure 7.3: Variation of the 7 MeV electron intensity at different positions in the inner heliosphere. The left panel displays the deviation of the electron intensities from their mean value for the distances of 1 AU (black lines), 2 AU (red lines) and at Jupiter's position of 5 AU (blue lines) from the Sun at the polar angles of  $20^\circ$  (solid lines),  $30^\circ$  (dotted lines),  $40^\circ$  (dashed lines) and  $50^\circ$  (dash-dotted lines). The horizontal black dotted lines represent the upper and lower limits of the deviations, respectively. The right panel shows the corresponding frequency analysis employing a Lomb algorithm. The colour coding is taken from the left panel. The horizontal dotted line indicates the 99% significance level.*

in time with 26 days in between. The colour coding and line styles are chosen as in Fig. 7.1. The first panel (upper left) is the same picture already shown above in Fig. 7.1. Over time, the electron intensities vary at mid to high latitudes. This influence of the Fisk-type field can be observed in the galactic electrons as well as in the Jovian electrons. Considering the total electron intensity at 1 AU (solid black line), the first panel reveals higher values in the northern hemisphere than in the southern hemisphere. During the solar rotation this picture changes and the electron intensity increases in the South, while it decreases in the North until it changes back again to reach its original values after 26 days. Accordingly, the same evolution can be noticed at 5 AU and 10 AU.

These variations are studied in Fig. 7.3 for the distances of 1 AU (black lines), 2 AU (red lines) and 5 AU (blue lines) from the Sun at the polar angles of  $20^\circ$  (solid lines),  $30^\circ$  (dotted lines),  $40^\circ$  (dashed lines) and  $50^\circ$  (dash-dotted lines). The left panel displays the deviations of the total electron intensities from their mean value at these twelve places of consideration for a time period of three solar rotations (78 days). The horizontal black dotted lines show the minimum and maximum deviation, respectively. There is a considerable systematic fluctuation of the electron intensities with a broad minimum and a narrow maximum and a periodicity of 26 days. The intensities vary between  $\sim -27\%$  and  $\sim 43\%$  around their mean values. The amplitude depends on the position in the heliosphere. The right panel shows the corresponding frequency analysis employing the Lomb algorithm (Lomb, 1976), called Lomb analysis in the following. The colour coding is taken from the left panel. The horizontal black dotted line indicates the 99% significance level. For these twelve positions taken into account in this study, a clear periodicity of 26 days becomes evident. These results emphasise the assumption, that 7 MeV electron intensities can be used as a remote sensing method for the HMF model.

## Ulysses Electron Measurements at high Latitudes

Until now, no clear signal of a Fisk-type field could be found in magnetic field measurements in the inner heliosphere (Roberts et al., 2007) and it is still under discussion whether or not this type of HMF model is detectable in magnetic field measurements in the inner heliosphere (Burger et al., 2008). The simulation results shown in Fig. 7.1 to 7.3 suggest that a Fisk-type HMF will lead to systematic variations of galactic and Jovian electron intensities, especially in the inner heliosphere, the space accessible to the Ulysses spacecraft. Therefore, the electron data measured by Ulysses/KET at high latitudes is analysed regarding their periodic behaviour.

Figure 7.4 displays the daily averaged Ulysses/KET 2.5 – 7 MeV electron count rate from 1995.6 to 1996.3. The upper panel displays the trajectory data of Ulysses and Jupiter, similar to Fig. 6.3. During the considered time span, the spacecraft moved from  $80^\circ$  North to  $40^\circ$  North, the latitudes where the influence of a Fisk-type HMF should be most pronounced during solar minimum conditions. The middle panel

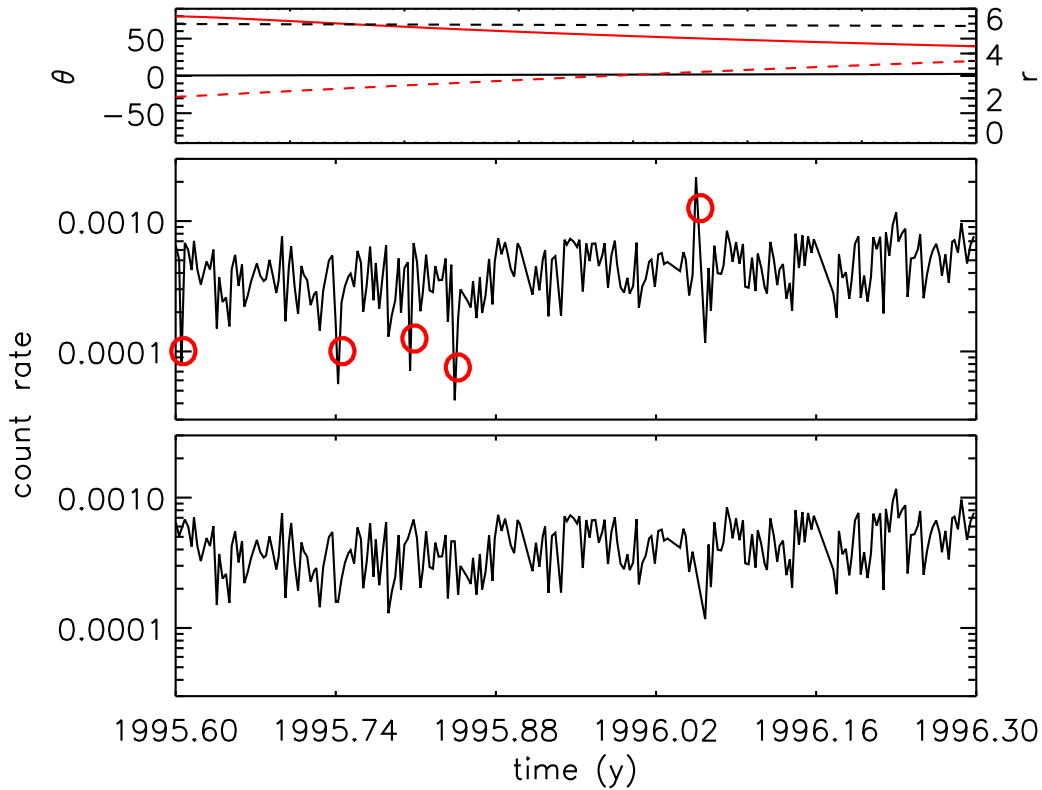


Figure 7.4: *Ulysses/KET* electron measurements at high latitudes. The upper panel displays the heliographic latitude  $\theta$  (solid lines) and the radial distance  $r$  to the Sun (dashed lines) of the spacecraft (red lines) and Jupiter (black lines). The middle panel displays the daily averaged corrected 2.5 – 7 MeV electron count rate from 1995.6 to 1996.3. For the further analysis, the five values marked with red circles are excluded from the data. The resulting count rate is shown in the bottom panel.

shows the original corrected count rate. The outlying data points marked with red circles are neglected in the further investigation due to a reduction of particle events using proton data. The resulting data are shown in the bottom panel and used in the following analysis.

The variation of the *Ulysses/KET* electron data from 1995.6 to 1996.3 is displayed in Fig. 7.5. The upper panel presents the deviation from the running mean of the detrended electron count rate with a mean value of the deviation of 37%. Lomb analyses of different subsets of the time period from 1995.6 to 1996.3 were performed (see Table 7.1). The results are displayed in the lower panels of Fig. 7.5. For all five cases, a periodicity of 26 days is found with the power of the periodicity lying above the

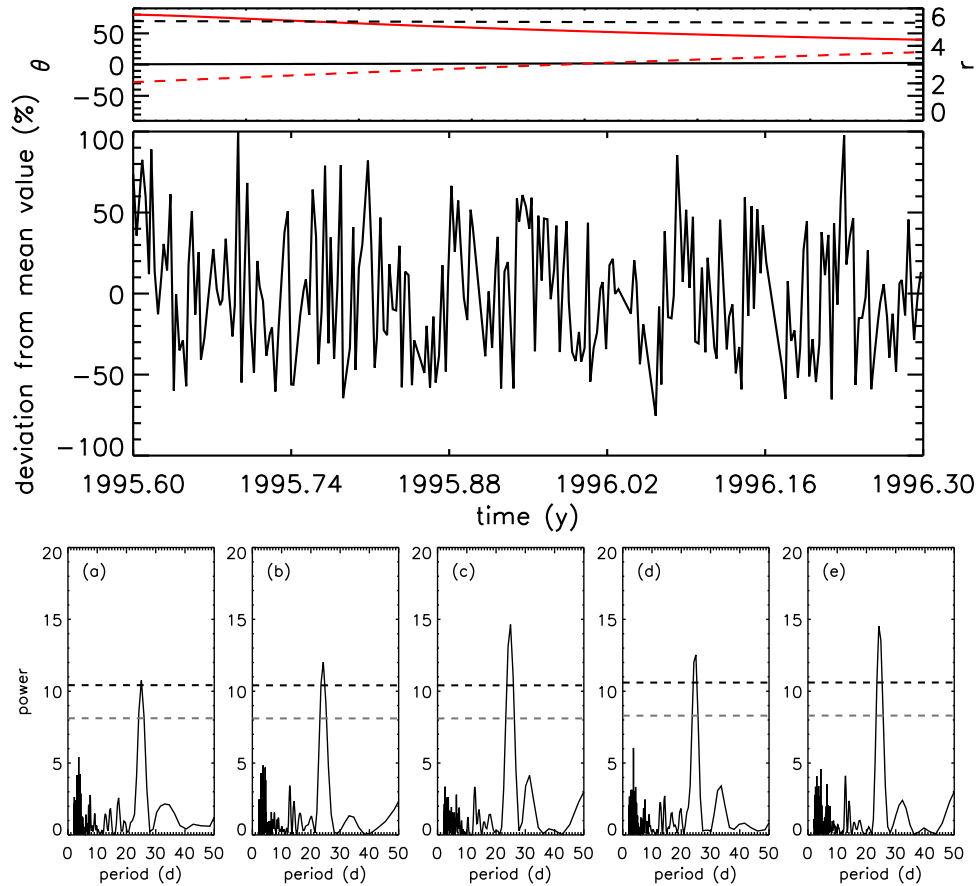


Figure 7.5: Variation of the 2.5 – 7 MeV electron count rate measured by Ulysses/KET at high latitudes. The upper panel shows the deviation from the running mean of the detrended electron count rate from 1995.6 to 1996.3. The lower panels display the Lomb analyses of the electron data for different subsets of the time period shown in the upper panel: (a) 1995.6 – 1996.1, (b) 1995.7 – 1996.2, (c) 1995.8 – 1996.3, (d) 1995.6 – 1996.2 and (e) 1995.7 – 1996.3. The black and grey dashed horizontal lines indicate the 99% and 90% significance levels, respectively.

99% significance level (black dashed line). The periodicity in the electron count rates gets stronger towards lower latitudes (panels b, c and e), but is, however, detectable up to the highest latitudes (panels a and d) accessible to the spacecraft.

To assure that these 26-day variations can be induced by a Fisk-type HMF, it is necessary to eliminate the possibility that they are caused by CIRs. Hence, the Ulysses/KET measurements of 250 – 2000 MeV protons are investigated for a correlation to the electron count rate. This study is shown in Fig. 7.6. The upper panel shows the deviation from the running mean of the detrended proton count rate. During most of the measurement, no periodic behaviour is visible. Not before  $\sim 1996.1$ , when Ulysses approaches low latitudes, fluctuations appear in the proton count rate. This

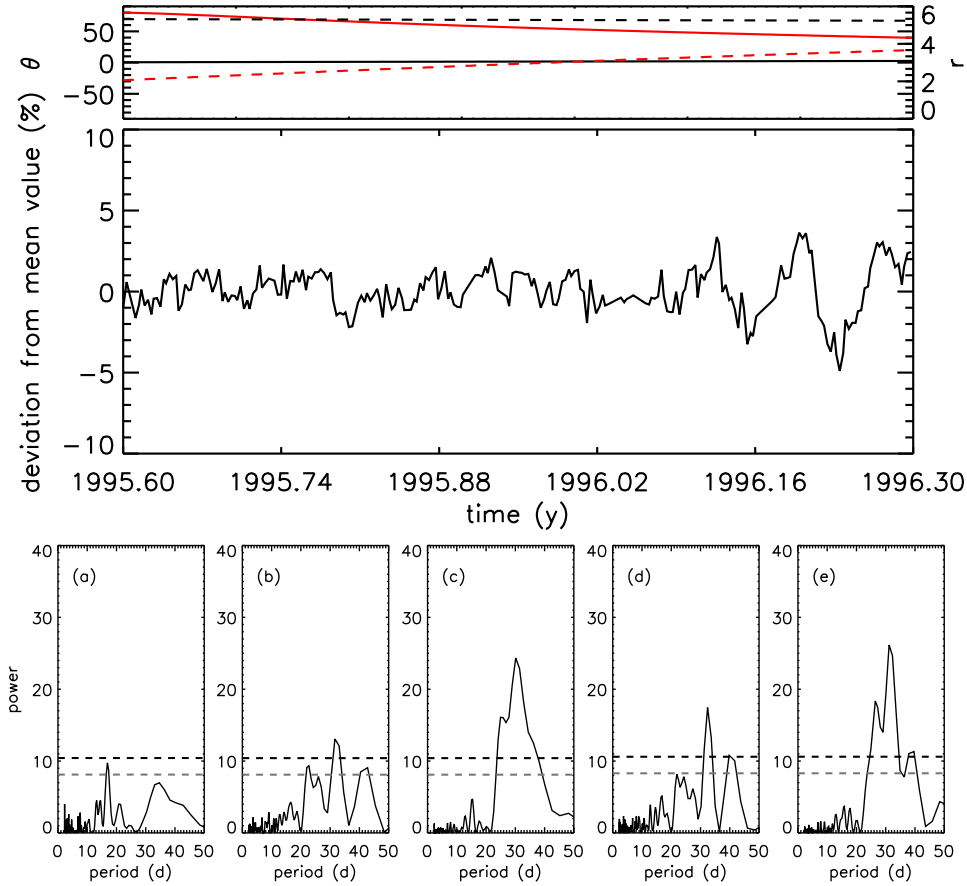


Figure 7.6: The same as Fig. 7.5, but for 250 – 2000 MeV protons.

becomes evident in the Lomb analyses (lower panels) for different subsets of the measurement. At the highest latitudes (panels a and b), the protons reveal a periodicity of  $\sim 15$  days, while they show a variation with a periodicity  $> 30$  days at lower latitudes (panels b, c and d). A periodicity of 26 days only appears in panels c and e, where the measurements after 1996.1 are fully taken into account.

An additional possible source of the electron variations can be found in the solar wind. Therefore, an analysis of the solar wind speed is performed. The upper panel of Fig. 7.7 displays the detrended deviation of the daily averaged solar wind speed measured by Ulysses/SWOOPS from 1995.6 to 1996.3 with an average deviation of 2.4%. The lower panels present the Lomb analyses of different subsets of this time period (solid black line) with the black and grey dashed lines indicating the 99% and the 90% significance levels, respectively. All five panels reveal a 26-day period in the solar wind speed with a power above the 99% significance level. This leads to the question whether the electron variations are related to the solar wind speed variations.



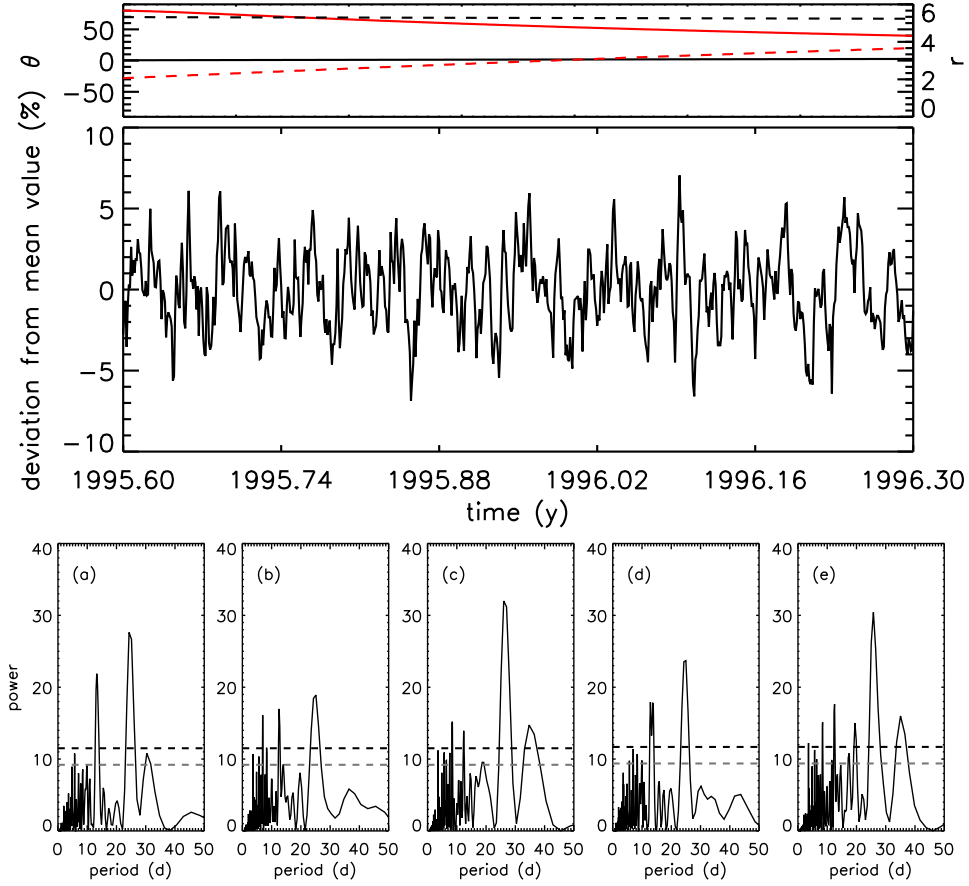


Figure 7.7: The solar wind speed measured by *Ulysses*/*SWOOPS* at high latitudes. The upper panel shows the deviation from the running mean of the daily averaged solar wind speed measured from 1995.6 to 1996.3. The lower panels display the Lomb analyses of the solar wind speed for the same time intervals as in Fig. 7.5. The black and grey dashed horizontal lines indicate the 99% and 90% significance levels, respectively.

To achieve a deeper insight into these possible correlations, the Pearson correlation coefficient (Bronstein et al., 2008)

$$\text{cor}(x, y) = \frac{\sum_{i=1}^n (x_i - \langle x \rangle) (y_i - \langle y \rangle)}{\sqrt{\sum_{i=1}^n (x_i - \langle x \rangle)^2 \cdot \sum_{i=1}^n (y_i - \langle y \rangle)^2}} \quad (7.1)$$

with  $\text{cor}(x, y) \in [-1, 1]$  is computed for the electron and proton count rates, as well as the electron count rate and the solar wind speed. Here,  $x$  and  $y$  denote the electron

time period	maximum power	e-p correlation	e- $u_{sw}$ correlation
(a) 1995.6 – 1996.1	10.75	–0.11	0.22
(b) 1995.7 – 1996.2	12.02	–0.10	0.16
(c) 1995.8 – 1996.3	14.64	–0.21	0.11
(d) 1995.6 – 1996.2	12.53	–0.16	0.17
(e) 1995.7 – 1996.3	14.53	–0.17	0.14
average:	12.89	–0.15	0.16

Table 7.1: Overview of the electron data Lomb analyses, the electron-proton correlation ( $e-p$ ) and the electron-solar wind speed correlation ( $e-u_{sw}$ ).

and proton/solar wind speed data arrays, respectively, and

$$\langle x \rangle = \frac{1}{n} \sum_{i=1}^n x_i \quad \text{and} \quad \langle y \rangle = \frac{1}{n} \sum_{i=1}^n y_i \quad (7.2)$$

are the corresponding mean values. Depending on the result of the function, a decision can be made whether a correlation between the two measurements exists:

$$cor(x, y) = \begin{cases} 1 & \text{almost certain correlation} \\ 0 & \text{no correlation} \\ -1 & \text{almost certain anti-correlation.} \end{cases} \quad (7.3)$$

The correlation coefficient is computed for the corresponding time periods that were discussed in Figs. 7.5, 7.6 and 7.7 and is presented in Table 7.1 together with the maximum power of the 26-day period of the electron count rate taken from the Lomb analysis. The correlation coefficient yields low negative values for the electron-proton correlation for all chosen subsets of the data, only beginning to rise when the lowest latitudes of the utilised measurements are taken into account. Following this analysis, the conclusion is obvious that the electrons and protons are not correlated and behave independently at mid to high latitudes. This can also be deduced from Fig. 7.8. The left panel shows the data points of the deviation from the running mean of the detrended electron count rate plotted over the corresponding data points of the deviation of the detrended proton count rate. If there was a correlation between these two data sets, a regular pattern of the data point distribution would be expected. This is, however, not the case.

The solar wind speed analysis leads to a similar situation. The correlation coefficient yields low positive values for all subsets of the measurement, rising towards higher latitudes. However, the correlation coefficient of the electron count rate and the solar wind speed is too low to indicate a correlation. This is supported by the right panel of Fig. 7.8. The data points of the deviation from the running mean of the detrended electron count rate are plotted over the corresponding data points of the deviation of the detrended solar wind speed. Again, no regular pattern appears in the data point

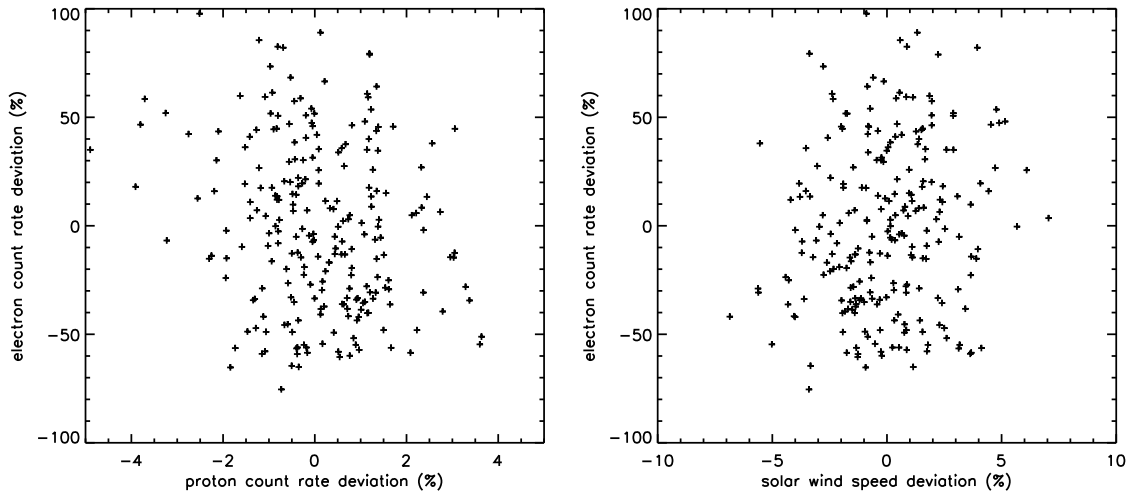


*Figure 7.8: A test for a correlation between the Ulysses electron count rate and the proton count rate or the solar wind speed. The left panel shows the data points of the deviation of the detrended electron count rate plotted over the corresponding data points of the deviation of the detrended proton count rate. The right panel displays the same, but for the electron count rate and solar wind speed deviation. In both panels, the data points do not reveal a regular pattern.*

distribution, indicating that no correlation can be found between the electron count rate and the solar wind speed.

For a comparison to the current study, the time-span analysed by Heber et al. (1997) is re-investigated for a correlation between the 250 – 2000 MeV proton count rate and the solar wind speed. These authors find recurrent variations in the proton count rate and relate them to the solar wind speed variations. This analysis is shown in Fig. 7.9. The upper left panel displays the detrended deviations of the proton count rate (red line) and the solar wind speed (black line) from their respective mean values between 1996.1 and 1996.4. The recurrent and anti-correlated variations become evident. The upper right panel presents the corresponding Lomb analysis with the same colour coding. The dashed lines represent the 99% significance levels. For both measurements, the Lomb analysis reveals a strong periodicity with the same duration. The lower panel shows the detrended deviation of the proton count rate plotted over the corresponding data points of the solar wind speed deviation being arranged close to the corresponding regression line, which was added to the plot to guide the eye. The correlation coefficient yields a value of  $-0.58$  for these measurements. In contrast to the investigation of a possible electron-proton or electron-solar wind speed correlation, this study suggests a possible correlation between the proton count rate and the solar wind speed (see also Heber et al., 1997).

Based on this investigation, the HMF is assumed to cause the 26-day variations

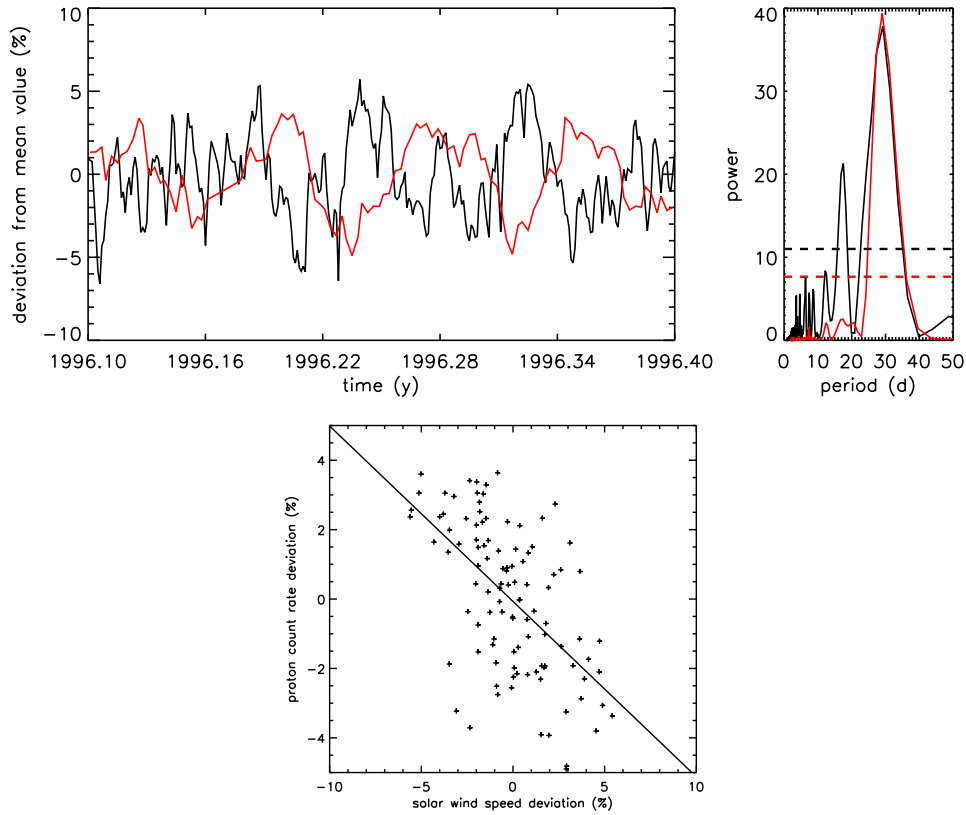


Figure 7.9: Correlation of the proton count rate and the solar wind speed between 1996.1 and 1996.4. The upper left panel shows the detrended deviation of the 250 – 2000 MeV proton count rate (red line) and the solar wind speed (black line) from their respective mean values. The upper right panel displays the corresponding Lomb analysis with the same colour coding and the dashed lines indicating the 99% significance levels. The same analysis as in Fig. 7.8 is shown in the lower panel, but for the proton count rate and solar wind speed deviations. To guide the eye, the regression line corresponding to these data points was added to the picture.

found in the electron count rate. Further assuming that the structure of the HMF is described by a Fisk-type HMF model, i.e. the Schwadron-Parker field (Hitge and Burger, 2010), implications on the parameters describing the field structure can be deduced from the Ulysses/KET electron measurements.

## Implications of Ulysses Electron Measurements on the Fisk Theory

Following the assumption that the 26-day variation found in the Ulysses/KET electron data is caused by a Fisk-type HMF, consequences for the Fisk theory can be derived by

comparing the model data of the 7 MeV electron count rate with Ulysses measurements. The simulation parameters are kept the same as for the results shown in Figs. 7.1 to 7.3, but with a time step of  $\Delta t = 0.52$  days. To study the conclusion by Roberts et al. (2007) that the HMF parameters employed in the Fisk theory have been overestimated so far, simulations for four different values of the Fisk angle (a)  $\beta = \beta_{\text{model}} \approx 12^\circ$  (see Fig. 3.15), (b)  $\beta = (3/4)\beta_{\text{model}}$ , (c)  $\beta = (1/2)\beta_{\text{model}}$  and (d)  $\beta = (1/4)\beta_{\text{model}}$  were performed, with  $\beta_{\text{model}}$  being the value of the Fisk angle assumed for solar minimum conditions by Burger et al. (2008). Note that a value around  $30^\circ$  was proposed for  $\beta$  in the original theory and was used in following studies relating to the Fisk field (Fisk, 1996; Zurbuchen et al., 1997; Roberts et al., 2007). These model results for the 7 MeV electron count rate along the Ulysses trajectory are presented in Fig. 7.10. The left panels show the simulation results for the detrended deviation from the running mean of the daily-averaged electron count rate for the four values of the Fisk angle  $\beta$  mentioned above from 1995.8 to 1996.2. In all four cases, the varying HMF structure

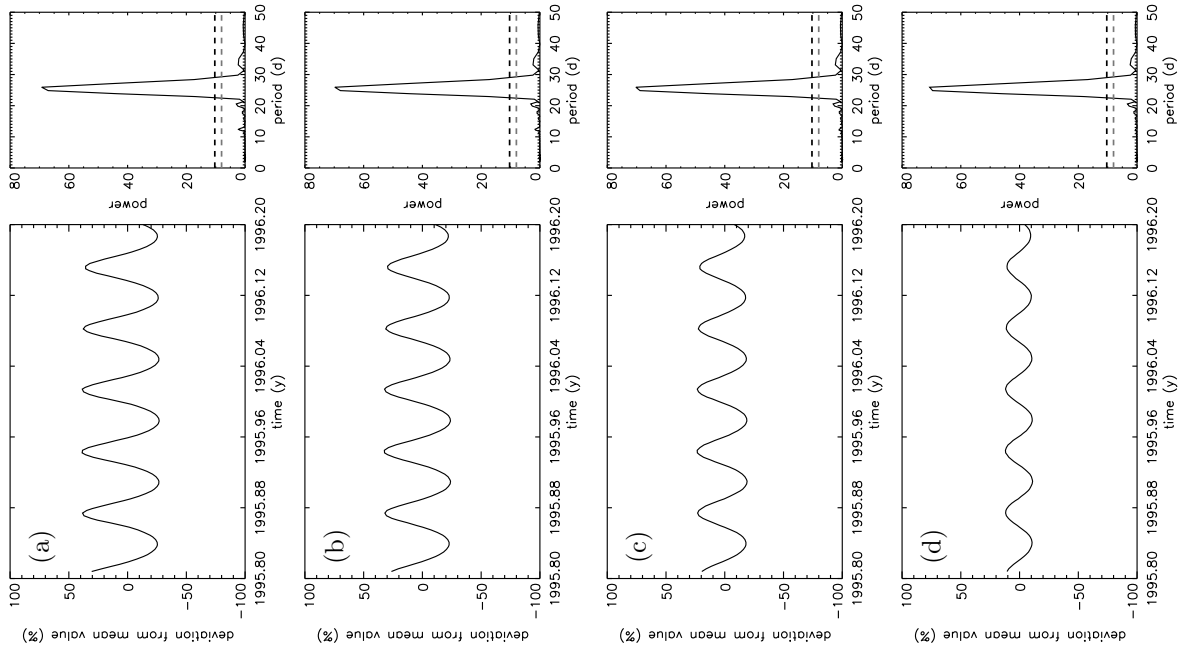


*Figure 7.10: Model results for the 7 MeV electron count rate along the Ulysses trajectory in a Schwadron-Parker HMF model from 1995.8 to 1996.2. The left panels show the detrended deviation of the electron count rate for different values of the Fisk angle  $\beta$ : (a)  $\beta = \beta_{\text{model}} \approx 12^\circ$  (see Fig. 3.15), (b)  $\beta = (3/4)\beta_{\text{model}}$ , (c)  $\beta = (1/2)\beta_{\text{model}}$  and (d)  $\beta = (1/4)\beta_{\text{model}}$ . The right panels present the corresponding Lomb analyses finding a 26-day variation in the model data in all four cases.*

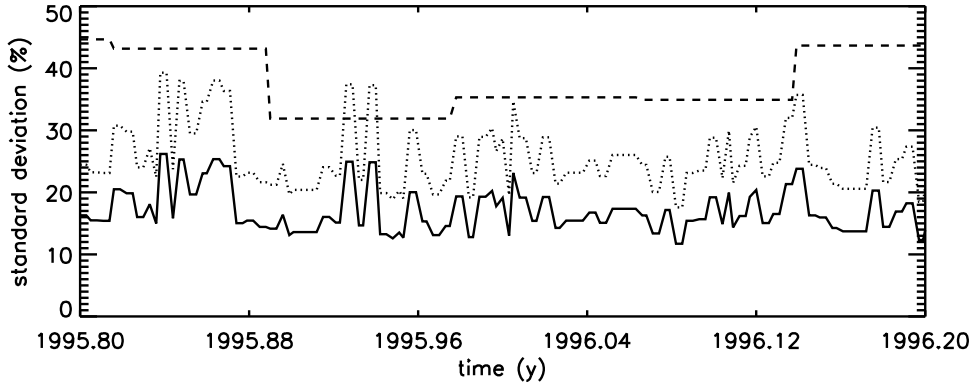


Figure 7.11: The noise amplitude added to the simulation data for the comparison to the *Ulysses* count rate. The solid line is computed from the Poisson statistics of the electron count rate (see Fig. 7.4). The dotted line is obtained by multiplying the solid line with a factor of 1.5. The dashed line represents the standard deviation of the electron count rate computed for periods of 26 days.

transfers its time dependence to the 7 MeV electron count rate, where considerable variations up to several 10% depending on  $\beta$  are observed in the simulation data. The corresponding Lomb analyses shown in the right panels reveal a periodicity of 26 days. The variation amplitude depends highly on the Fisk angle  $\beta$ . The lowering of  $\beta$  leads to a decreasing fraction of the Fisk field in the Schwadron-Parker hybrid HMF and, therefore, to a less wavy structure of the HMF field lines. The difference between the maximum and minimum values of the deviation drop from  $\sim 60\%$  (a) down to  $\sim 20\%$  (d).

Employing the  $\beta$  dependence of the variation amplitude, the possibility arises to find restrictions for the Fisk angle by applying the same amount of noise which is seen in the measurements to the simulation data. Limits for the value of  $\beta$  can be found by comparing the maximum power of the 26-day variations found in the Lomb analyses of the simulation data and the *Ulysses*/KET measurements. White noise was added to the simulation data with the IDL function `randomn` and the Box-Muller method (Box and Muller, 1958). Three different average amplitudes of the noise were applied to the model and tested against the measured data. The noise amplitudes are displayed in Fig. 7.11. The solid line is the standard deviation of the electron count rate measured by *Ulysses*/KET computed from Poisson statistics. The dashed line represents the standard deviation

$$\Delta f = \sqrt{\frac{1}{n-1} \sum_{n=1}^N (f_i - \langle f \rangle)^2}$$

computed for time periods of 26 days with the average count rate  $\langle f \rangle$ . The latter will overestimate the noise amplitude, because systematic variations will lead to a

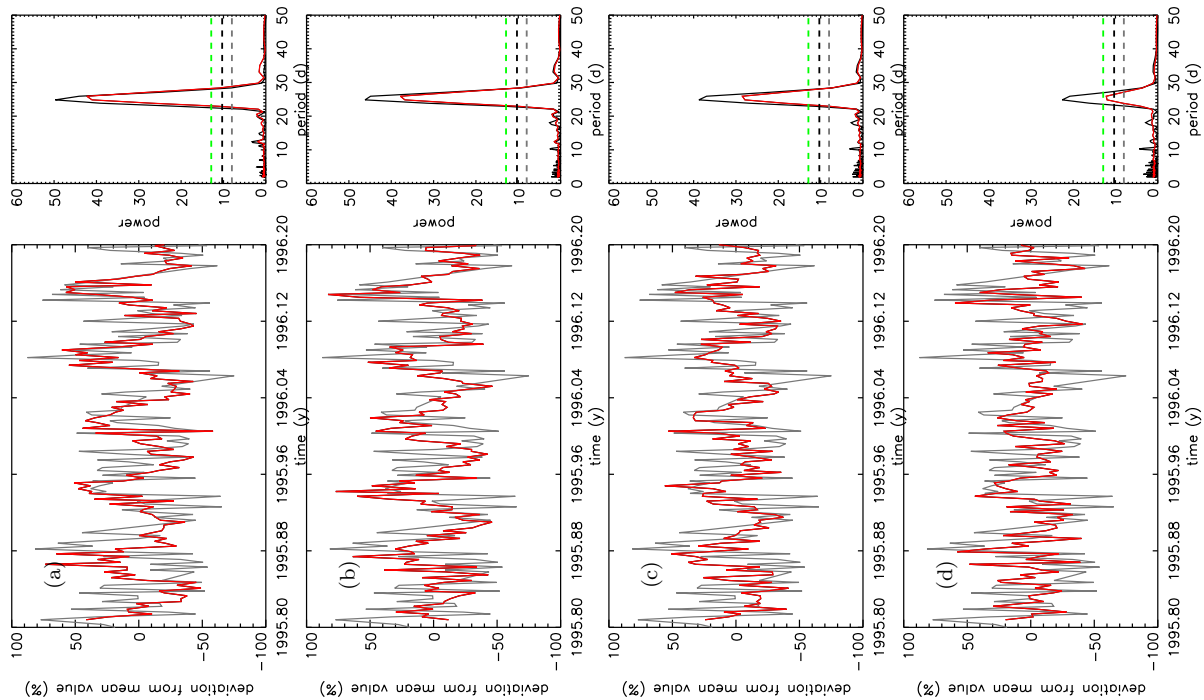


Figure 7.12: Comparison of the Ulysses/KET electron measurements and the model data (see Fig. 7.10) with additional white noise. The average noise amplitude is computed from the Poisson statistics of the Ulysses/KET electron count rate (see Fig. 7.11). The left panels show the simulation data from Fig. 7.10 with additional white noise (red line) and the electron data from Fig. 7.4 (grey line). The right panels show the corresponding Lomb analyses with the black and grey dashed lines representing the 99% and 90% significance levels, respectively. The green dashed line indicates the averaged maximum power of the Lomb analysis of the Ulysses/KET electron count rate (see Table 7.1). For this study, white noise is added to the simulation data randomly and analysed with the Lomb algorithm 100 times. The average of these frequency analysis results is represented by the red line. The black line displays the frequency analysis with the maximum power of the 26-day periodicity chosen from the 100 Lomb analyses that were performed to obtain the average.

higher standard deviation in addition to the noise. The Poisson statistics will, however, underestimate the noise, because the process of the electron data correction needed to obtain the count rate from the raw data leads to additional errors. This is accounted for in the dotted line, where an average standard deviation is obtained by multiplying the black line with a factor of 1.5. This was chosen to account for the additional noise added to the KET measurements by neutrons and gamma rays produced by the RTG (Radioisotope Thermoelectric Generator). The comparison of the model to the Ulysses/KET data is discussed for these three noise amplitudes in the following.

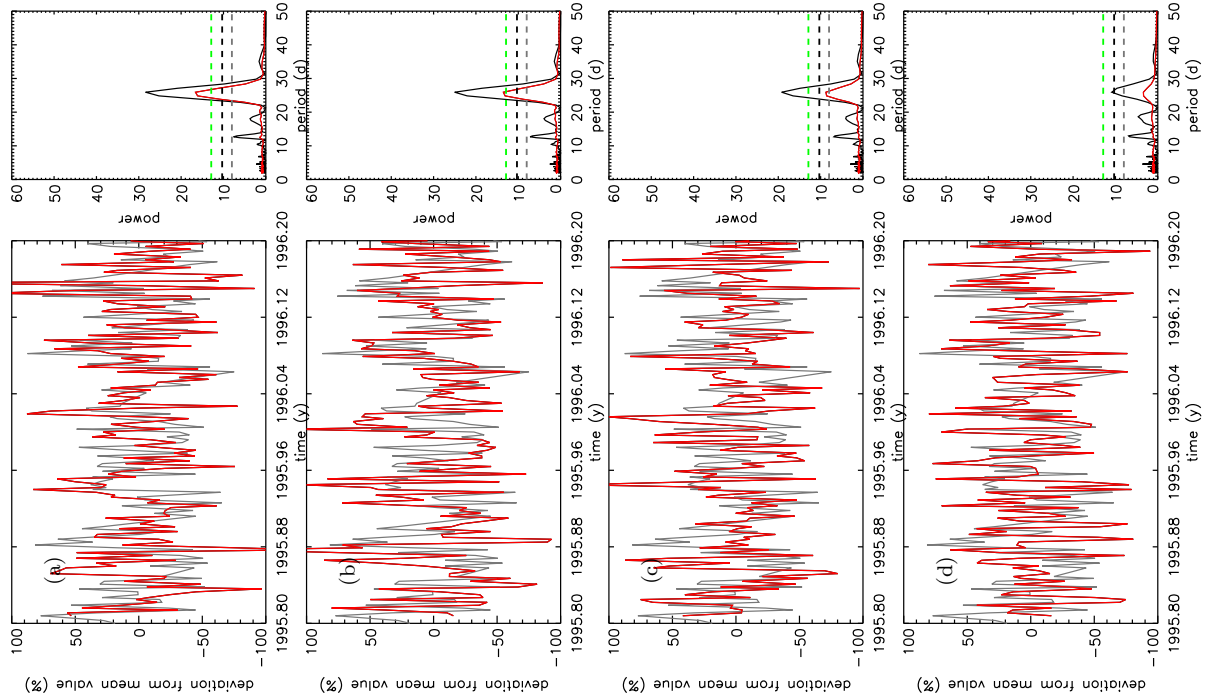


Figure 7.13: The same as Fig. 7.12, but with the standard deviation computed for periods of 26 days as an upper limit of the noise amplitude (see Fig. 7.11).

Figure 7.12 displays the simulation results shown in Fig. 7.10 with additional white noise with the lower limit noise amplitude computed from the Poisson statistics of the Ulysses/KET electron count rate (solid line in Fig. 7.11). The left panels present the model (red line) and Ulysses/KET data (grey line). In this comparative illustration, the impression arises that the variation found in the model data can also be seen in the Ulysses measurements and that both are in phase. The model variation amplitudes decrease from panel (a) to panel (d) due to the lower waviness of the field lines in the Schwadron-Parker HMF. The influence of the white noise applied to the model data becomes evident in the Lomb analyses displayed in the right panels. Since the addition of noise to the simulation data is a statistical process leading to different results in the Lomb analysis, the addition of noise and the Lomb analysis were performed 100 times. The average of these frequency analyses is represented by the red line. The black line displays the frequency analysis with the maximum power of the 26-day variations chosen from the 100 Lomb analyses. The black and grey dashed lines represent the 99% and the 90% significance levels, respectively, while the green dashed line indicates the averaged maximum power of the Lomb analysis of the Ulysses/KET electron count rate (see Fig. 7.5 and Table 7.1.) To obtain an agreement between model and measurement, the simulation data in the left panels must match the Ulysses/KET data. For the variation amplitude, this is the case in



panels (a), (b) and (c) of Fig. 7.12. However, the noise added to the simulation data is underestimated in this case. In addition, the peak of the averaged Lomb analysis (red curve in the right panels) should be in the range of the averaged maximum power of the Ulysses/KET data Lomb analysis (dashed green line). If this is the case, the combination of the amplitude of the systematic variations due to the Fisk-type HMF and the noise match the corresponding quantities of the measured data. This can only be seen in panel (d), where the variation amplitude found in the model (left panel) is too low to fit the measured data. Figure 7.12 suggests that no agreement between model and measurement can be achieved in this case.

Figure 7.13 displays the same study as Fig. 7.12, but for the upper limit noise amplitude (dashed line in Fig. 7.11). In a comparison of the measured and computed data, a decision which value of  $\beta$  leads to the best fit of model and spacecraft data is not possible based on the left panels. Furthermore, the noise added to the simulation data overestimates that of the measurements. The Lomb analyses (right panels) reveal that the strong noise masks the effect of the 26-day variations. The power of the periodicity found with the frequency analysis is considerably lower than in Fig. 7.12. For  $\beta = (1/2)\beta_{\text{model}}$  (panel c) the power of the 26-day variations drops below the 99% significance level and almost disappears for  $\beta = (1/4)\beta_{\text{model}}$  (panel d). For the upper

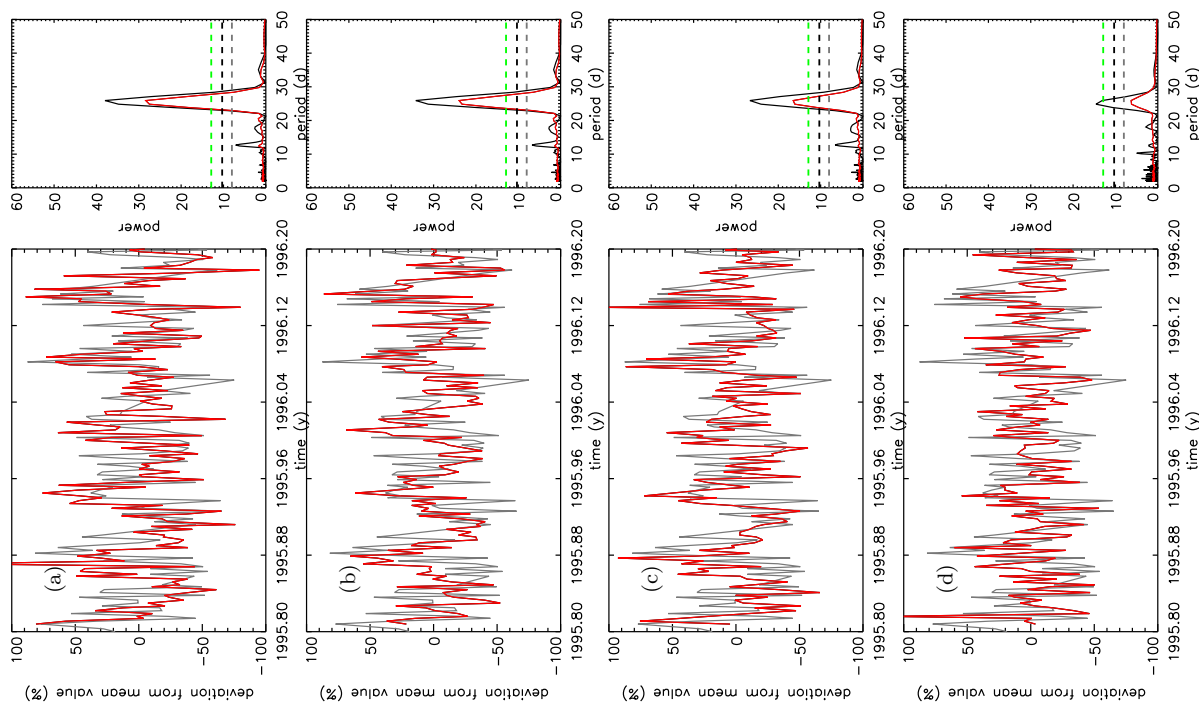


Figure 7.14: The same as Fig. 7.12, but for the noise amplitude computed from Poisson statistics multiplied with a factor of 1.5 as an average value of the noise amplitude (see Fig. 7.11).

limit noise amplitude, the Lomb analyses suggest panels (a) and (b) to be the best data fits, where the influence of the Fisk field is the strongest due to large values of  $\beta$ . However, Roberts et al. (2007) – assuming the Fisk theory is applicable – state that the parameters of the Fisk theory are overestimated until now. Their finding and the comparison of model and measurements in the left panels lead to the conclusion that there is also no agreement of model and measurements to be found in Fig. 7.13.

The average noise amplitude (dotted line in Fig. 7.11) was added to the simulation data in Fig. 7.14. The colour coding and line styles are the same as in Fig. 7.12. It becomes obvious that the amount of noise added to the computed data is in the range of the measurement noise in this case (left panels). The variation amplitudes of the simulation data fit to the amplitude of the measured data in panels (a), (b) and (c). Only panel (d) can be excluded in this comparison. The corresponding Lomb analyses show that the 26-day variations are too strong in panels (a) and (b) for  $\beta = \beta_{\text{model}}$  and  $\beta = (3/4)\beta_{\text{model}}$ , respectively, while  $\beta = (1/4)\beta_{\text{model}}$  (d) not only leads to the variation amplitude being too low, but also to weak variations with an average power below the 90% significance level. Panel (c), however, reveals an average power of the 26-day variations in the frequency analysis (red line) to be in the range of the 26-day variations found in the Ulysses/KET electron data (green dashed line). Therefore, this analysis suggests that the best fit of model and measurements in a Schwadron-Parker HMF model can be found with a reduced Fisk angle around  $\beta = (1/2)\beta_{\text{model}} \approx 6^\circ$  for the considered time period and diffusion coefficients, supporting the finding of Roberts et al. (2007).

## Consequences for the HMF Structure and the Transport of Energetic Particles

As a last step, the consequences of the low value of the Fisk-angle  $\beta$  derived above are presented for the HMF structure and the latitudinal diffusion. The Schwadron-Parker hybrid HMF is compared to the Parker HMF for  $\beta = 12^\circ$ , the value assumed for solar minimum by Burger et al. (2008), and  $\beta = 6^\circ$ , the value of the Fisk-angle derived in this work from Ulysses/KET electron measurements. Figure 7.15 displays magnetic field lines for two different values of  $\beta$ . The upper left panel presents a 3D illustration of two field lines of the Schwadron-Parker HMF model for  $\beta = 12^\circ$  with different footpoints on the source surface. The black line starts at the heliographic equator ( $\theta_0 = 90^\circ$ ), while the red line originates at a colatitude of  $30^\circ$ . In the equatorial region the HMF is a Parker field. The high latitude field line reveals a complex structure connecting a wide range of heliographic latitudes. This is also reflected in the right panel. A two-dimensional unwound of three field lines with different footpoints on the source surface are shown here. The red line ( $\theta_0 = 30^\circ$ ) covers a latitudinal range of  $32^\circ$ , while the blue line ( $\theta_0 = 65^\circ$ ) connects a range of  $22^\circ$ . The black line ( $\theta_0 = 90^\circ$ ) is covered by the abscissa and stays in the equatorial plane. The lower two panels

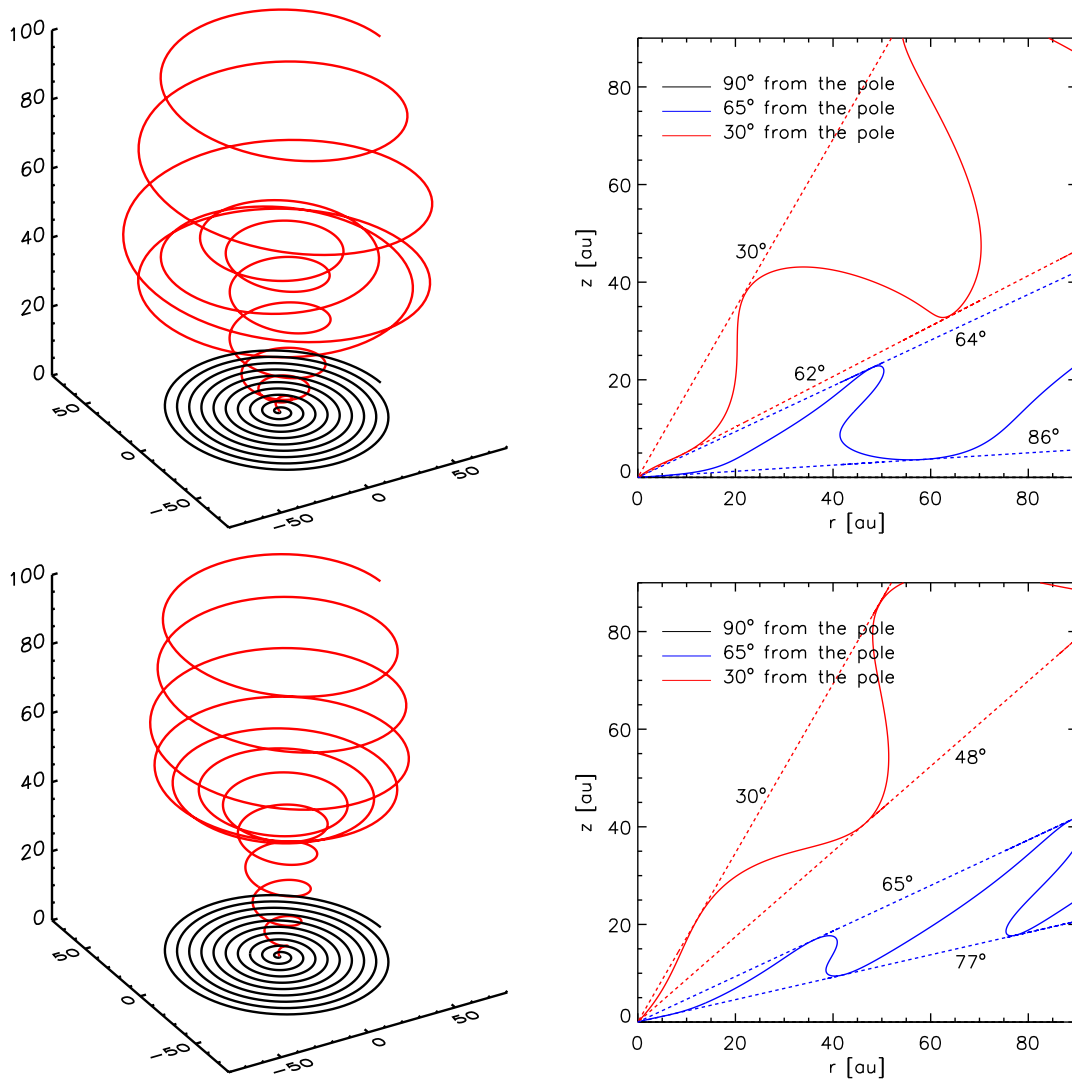


Figure 7.15: 3D and 2D illustrations of the Schwadron-Parker field with the parameters derived in this chapter. The HMF structure is shown for two values of the Fisk-angle:  $\beta = 12^\circ$  (upper panels) and  $\beta = 6^\circ$  (lower panels). The left panels display the three-dimensional structure of two magnetic field lines with different initial colatitudinal positions (red line:  $\theta_0 = 30^\circ$ , black line:  $\theta_0 = 90^\circ$ ). The right panels present three magnetic field lines in an unwound projection to emphasize the wavy structure of the field lines. The black lines are covered by the abscissa and are, therefore, not visible. The dotted lines indicate the latitudinal extension of the corresponding field lines. For comparative reasons, the same parameters as in Fig. 3.16 were used, but with the two different Fisk-angles mentioned above.

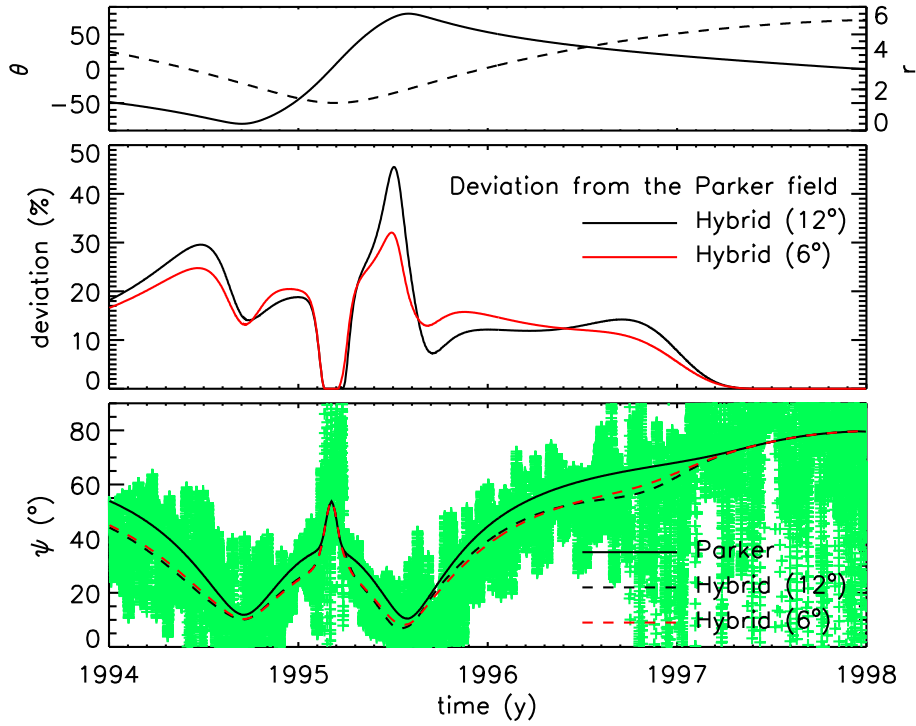


Figure 7.16: Comparison of the magnetic field angle,  $\psi$ , computed for different HMF configurations to Ulysses measurements. The upper panel shows the Ulysses trajectory (latitude: solid line, radial distance to the Sun: dashed line). The lower panel displays the magnetic field angle  $\psi$  computed from the Parker field (solid black line) and the Schwadron-Parker hybrid HMF for  $\beta = 12^\circ$  (dashed black line) and  $\beta = 6^\circ$  (dashed red line). The green crosses represent the Ulysses HMF measurements. For this study, the magnetic field polarity was neglected. The middle panel represents the deviation of the  $\beta = 12^\circ$  (black line) and  $\beta = 6^\circ$  (red line) hybrid HMF models to the Parker field.

show the same field lines, but for  $\beta = 6^\circ$ . The three-dimensional structure of the high latitude HMF line becomes more Parker-like, only connecting a narrow band of latitudes. This becomes evident in the 2D projection. The red and blue HMF lines only cover ranges of  $18^\circ$  and  $12^\circ$ , respectively. Considering the latitudinal transport of energetic particles, this leads to the conclusion that the influence of the Fisk-type HMF structure on the diffusion coefficient,  $\lambda_{\theta\theta}$ , is lower than expected from the original theory.

The angle  $\psi$  of the magnetic field vector with respect to the radial direction is computed by

$$\psi = \arctan \left( -\frac{B_\phi}{\sqrt{B_r^2 + B_\theta^2}} \right) \quad (7.4)$$

and presented in Fig. 7.16 for the Ulysses trajectory from 1994 to 1998. The upper panel shows the Ulysses radial distance from the Sun  $r$  (dashed line) and latitude  $\theta$  (solid line). The lower panel compares  $\psi$  for the Parker field (solid black line) and the Schwadron-Parker hybrid HMF with  $\beta = 12^\circ$  (dashed black line) and  $\beta = 6^\circ$  (dashed red line) to Ulysses magnetic field measurements (green crosses). As expected from the Fisk theory,  $\psi$  is closer to the measured values for the two hybrid fields, while the Parker field overestimates the measurements at mid to high latitudes. The middle panel presents the deviation of  $\psi$  in the two hybrid models (black line:  $\beta = 12^\circ$ , red line:  $\beta = 6^\circ$ ) from  $\psi$  in the Parker field. Both hybrid HMF models differ from the Parker model by  $\sim 20\%$  at mid to high latitudes, while both models lead to a Parker field in the equatorial region and over the solar poles. However, the two hybrid models show a very similar behaviour and are not distinguishable in a comparison of the angle  $\psi$  between the models and the measured values.

The influence of the Schwadron-Parker HMF model on the transport of 7 MeV electrons is presented in Figs. 7.17 to 7.20. The mean free path in the Parker and

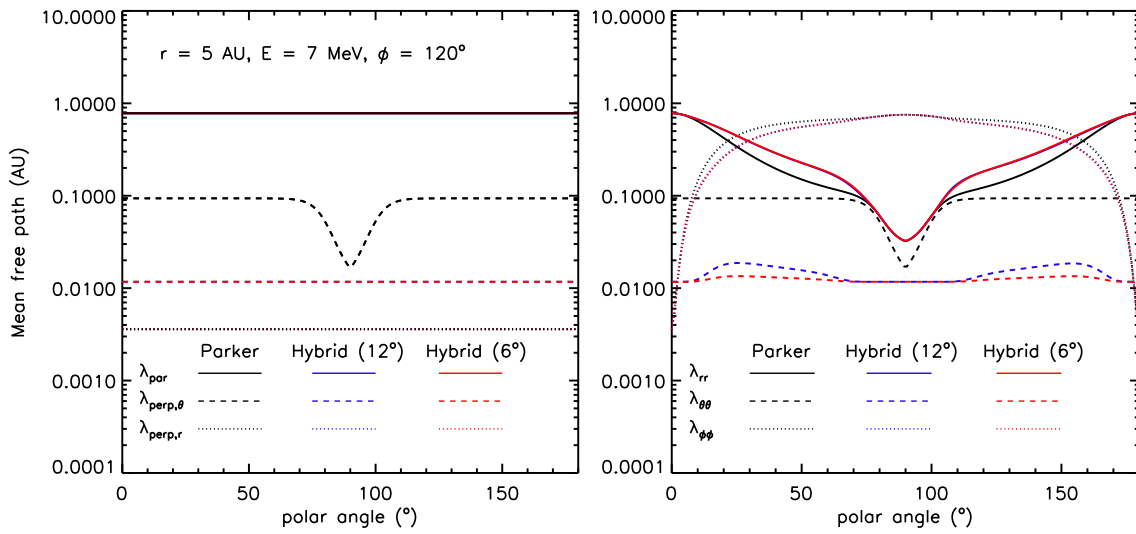


Figure 7.17: The latitudinal dependence of the mean free path in different HMF configurations for 7 MeV electrons at 5 AU and  $\phi = 120^\circ$ . The left panel displays  $\lambda_{\parallel}$  (solid lines),  $\lambda_{\perp\theta}$  (dashed lines) and  $\lambda_{\perp r}$  (dotted lines) in magnetic field aligned coordinates for the Parker HMF (black lines) and the Schwadron-Parker hybrid HMF with  $\beta = 12^\circ$  (blue lines) and  $\beta = 6^\circ$  (red lines). For the two hybrid HMF models, the same set of diffusion coefficients is applied. Therefore, the red and blue lines lie on top of each other. For the Parker field,  $\lambda_{\perp\theta}$  is enhanced by a factor of eight at higher latitudes and is, therefore, different from  $\lambda_{\perp\theta}$  in the hybrid fields. However,  $\lambda_{\parallel}$  and  $\lambda_{\perp r}$  lie on top of the corresponding curves for the hybrid fields. The right panel shows  $\lambda_{rr}$  (solid lines),  $\lambda_{\theta\theta}$  (dashed lines) and  $\lambda_{\phi\phi}$  (dotted lines) in spherical polar coordinates for the same HMF models.

the Schwadron-Parker fields are shown in Fig. 7.17 for  $r = 5$  AU,  $\phi = 120^\circ$  and  $E = 7$  MeV. The longitude  $\phi = 120^\circ$  was chosen, because the maximum influence of the Fisk-type fields on  $\lambda_{\theta\theta}$  can be found there. The left panels present  $\lambda_{\parallel}$  (solid lines),  $\lambda_{\perp\theta}$  (dashed lines) and  $\lambda_{\perp r}$  (dotted lines) for the Parker field (black lines) and the Schwadron-Parker HMF model with  $\beta = 12^\circ$  (blue lines) and  $\beta = 6^\circ$  (red lines). The red and blue lines lie on top of each other, because in the two hybrid models the same diffusion coefficients are employed. For the Parker field,  $\lambda_{\parallel}$  and  $\lambda_{\perp r}$  also do not differ from the hybrid models. The only difference is the latitudinal mean free path  $\lambda_{\perp\theta}$ , where the parameters for solar minimum conditions applied in chapter 6 are used. In comparison to solar maximum conditions, the mean free path  $\lambda_{\perp\theta}$  shows an enhancement by a factor of eight at higher latitudes. This was proposed by Ferreira (2002) as a consequence of high turbulence in the fast solar wind and to account for the influence of a Fisk-type HMF to reproduce Ulysses measurements. The right panel shows  $\lambda_{rr}$  (solid lines),  $\lambda_{\theta\theta}$  (dashed lines) and  $\lambda_{\phi\phi}$  (dotted lines) in spherical polar coordinates for the same HMF models. While  $\lambda_{\phi\phi}$  behaves very similar in all three HMF models, a major difference can be found in  $\lambda_{rr}$  at mid to high latitudes leading to a higher radial particle transport in the Fisk-type field models compared to the Parker field. Considering the latitudinal transport, both hybrid HMF models only lead to very low enhancements in  $\lambda_{\theta\theta}$ , which is hardly recognisable for  $\beta = 6^\circ$ . This illustration shows that the Fisk theory can only account for a low fraction of the enhancement in the latitudinal transport needed to reproduce the Ulysses measurements during solar minimum conditions.

A comparison of the enhancement produced by the Schwadron-Parker field models to the enhancement needed in the Parker field to reproduce the Ulysses measurements is presented in Fig. 7.18. The fraction

$$F = \frac{\Delta_F}{\Delta_P} \cdot 100\% \quad (7.5)$$

of the enhancement accounted for by the hybrid HMF models is shown for  $\beta = 12^\circ$  and  $\phi = 0^\circ$  (upper left panel),  $\beta = 12^\circ$  and  $\phi = 180^\circ$  (lower left panel),  $\beta = 6^\circ$  and  $\phi = 0^\circ$  (upper right panel) and  $\beta = 6^\circ$  and  $\phi = 180^\circ$  (lower right panel). Here,  $\Delta_P$  and  $\Delta_F$  denote the differences of the mean free path  $\lambda_{\theta\theta}$  between solar minimum and solar maximum in a Parker field and the Fisk-type fields, respectively, and are computed by

$$\begin{aligned} \Delta_P &= \lambda_{\theta\theta}^{\text{P,solmin}} - \lambda_{\theta\theta}^{\text{solmax}} \\ \Delta_F &= \lambda_{\theta\theta}^{\text{F,solmin}} - \lambda_{\theta\theta}^{\text{solmax}} \end{aligned} \quad (7.6)$$

with the mean free path  $\lambda_{\theta\theta}^{\text{P,solmin}}$  and  $\lambda_{\theta\theta}^{\text{F,solmin}}$  in the Parker- and the Fisk-type HMF during solar minimum conditions, respectively, and the latitudinal mean free path  $\lambda_{\theta\theta}^{\text{solmax}}$  during solar maximum conditions. The  $\beta = 12^\circ$  hybrid HMF reveals locally restricted bands connecting low and high latitudes, in which the field structure causes an enhanced latitudinal transport. The effect is low up to a radial distance of 5 AU to

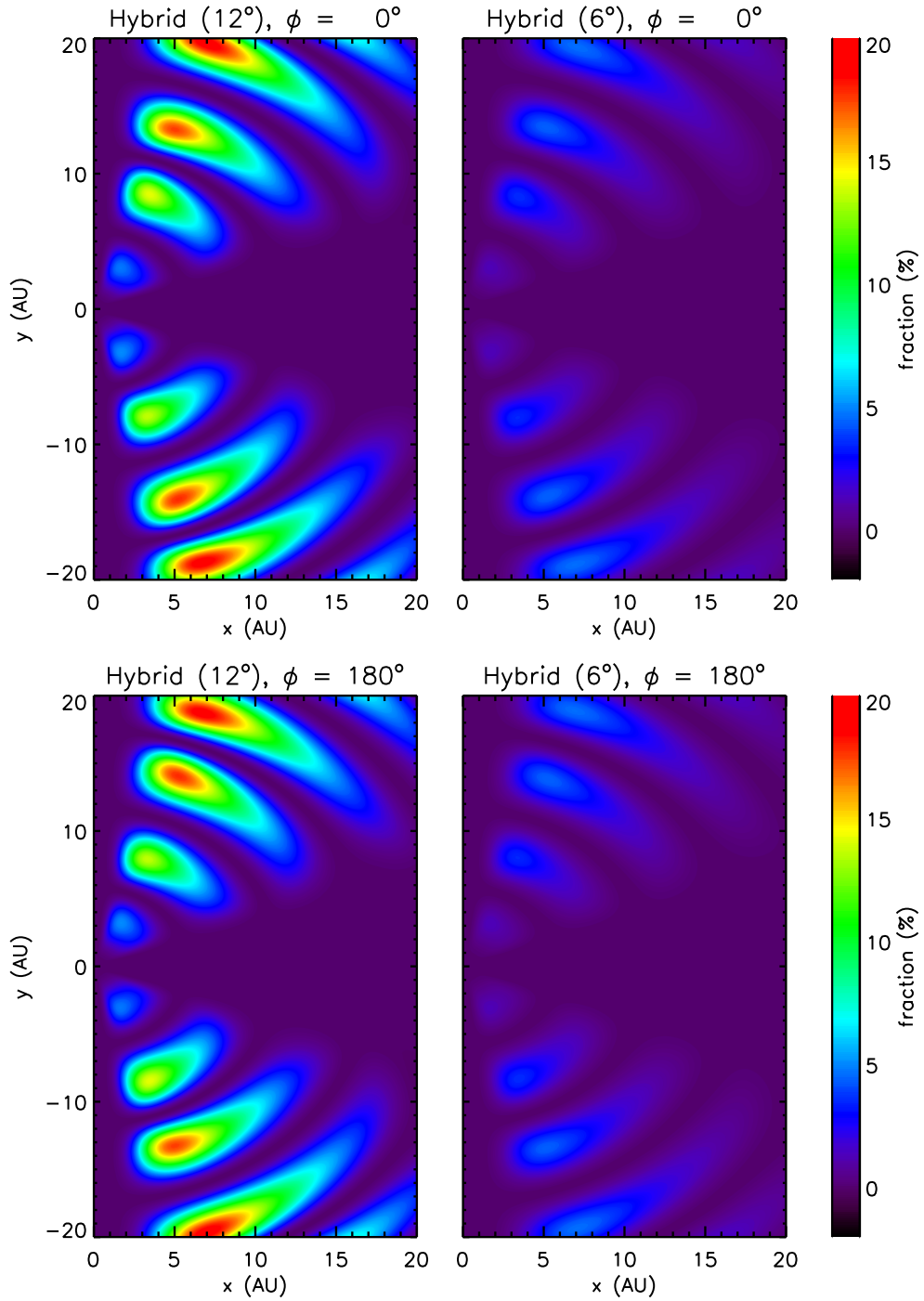


Figure 7.18: The fraction of the  $\lambda_{00}$ -enhancement provided by the Schwadron-Parker HMF model according to equation (7.5).

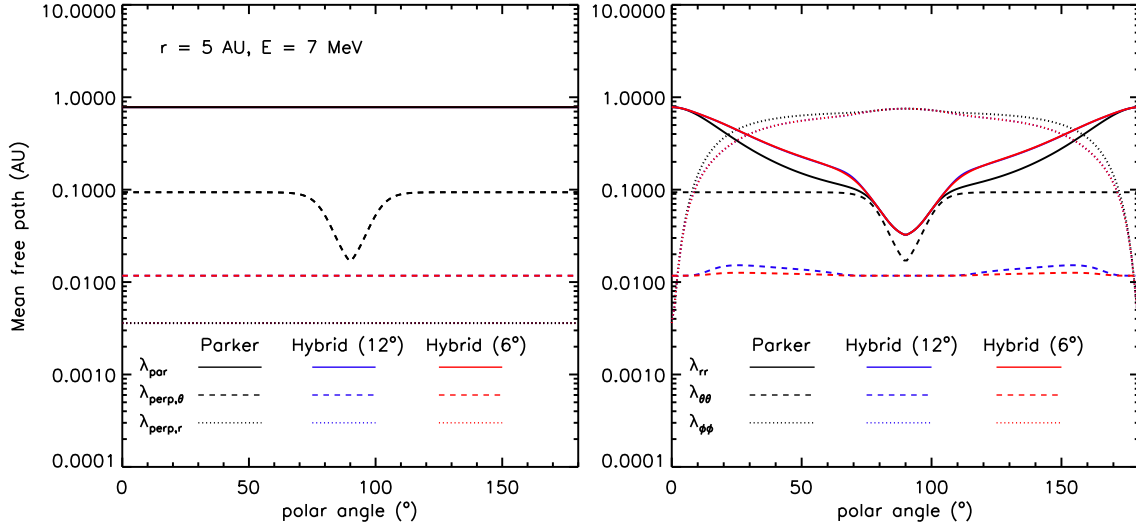


Figure 7.19: The same as Fig. 7.18, but with  $\lambda_{rr}$ ,  $\lambda_{\theta\theta}$  and  $\lambda_{\phi\phi}$  averaged over a solar rotation.

the Sun, where the Schwadron-Parker HMF only accounts for  $\sim 5\%$  of the enhancement expected from simulations of the 7 MeV electron transport in a Parker field. The influence of the Fisk-type field increases toward the outer heliosphere, rising to  $\sim 20\%$  at a radial distance of  $\sim 20$  AU to the Sun at the two heliographic longitudes shown in Fig. 7.18. Comparing the upper and lower left panels, the point symmetry of the Schwadron-Parker HMF model with respect to the origin of the coordinate system becomes evident in this study. The right panels showing the influence of the hybrid field with  $\beta = 6^\circ$  reveal the same structure as the left panels. However,  $\beta = 6^\circ$  leads to a lower enhancement of  $\lambda_{\theta\theta}$  and, therefore, accounts for a lower fraction of the enhancement needed in the Parker case during solar minimum conditions. The effect adds up to  $\sim 2\%$  closer than 5 AU to the Sun and rises to  $\sim 6\%$  at a distance of  $\sim 20$  AU to the Sun.

Figures 7.17 and 7.18 only consider the influence of a Fisk-type HMF on short time scales ( $< 26$  days). To study its influence on the long-term modulation of energetic particles, the mean free path has to be averaged over a solar rotation. This is shown in Fig. 7.19. The left panel is the same as the left panel in Fig. 7.17. The right panel presents  $\lambda_{rr}$  (solid lines),  $\lambda_{\theta\theta}$  (dashed lines) and  $\lambda_{\phi\phi}$  (dotted lines) in spherical polar coordinates for the three HMF models considered in this investigation averaged over a solar rotation. All coefficients basically show the same behaviour as in Fig. 7.17. However, the averaged enhancement of  $\lambda_{\theta\theta}$  is lower than for  $\lambda_{\theta\theta}$  at  $\phi = 120^\circ$ , where the maximum effect of the Schwadron-Parker field was shown.

Figure 7.20 presents the fraction of the  $\lambda_{\theta\theta}$  enhancement needed in the Parker field accounted for by the two Fisk-type fields considered in this study averaged over a solar



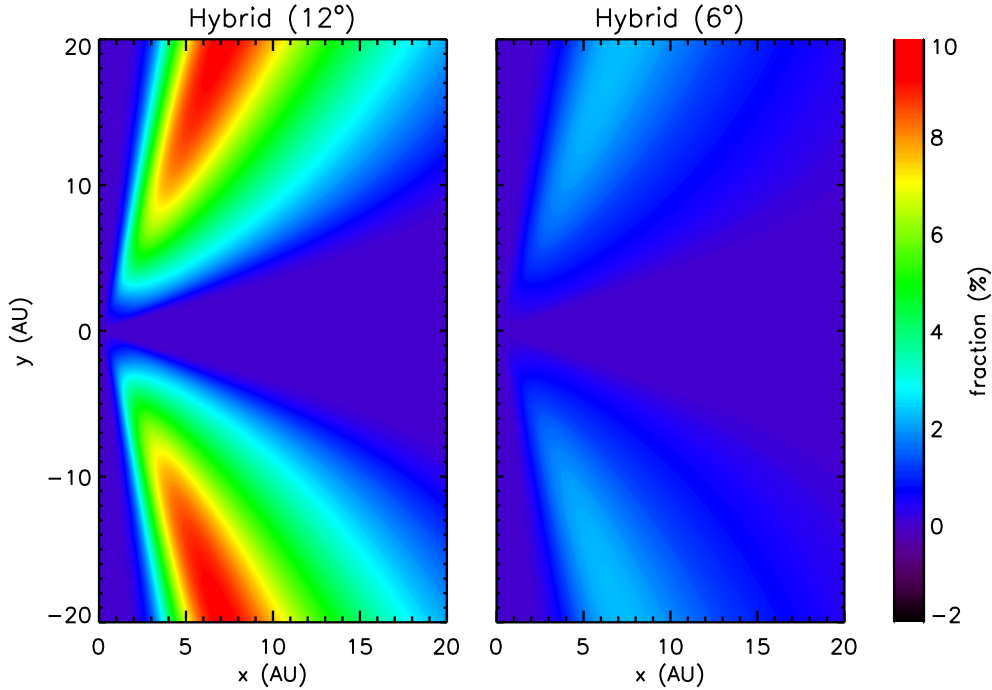


Figure 7.20: The same as Fig. 7.18, but with  $\lambda_{\theta\theta}$  averaged over a solar rotation. Note that the scale of the colour table is different from Fig. 7.18.

rotation. The left panel shows the  $\beta = 12^\circ$  case, while the right panel displays the influence of the  $\beta = 6^\circ$  hybrid field. Note that the scale of the colour table is different from Fig. 7.18. For both cases, the averaging leads to a smearing of the enhancement over the radial distance. The average effect of the Schwadron-Parker hybrid field is low at distances  $< 5$  AU to the Sun and rises towards the outer heliosphere. For the  $\beta = 12^\circ$  case, it reaches values of  $\sim 10\%$  at high latitudes at a distance of  $\sim 20$  AU to the Sun. However, the study presented above indicated that  $\beta = 6^\circ$  is a more realistic value of the Fisk-angle during the time considered here. For this case, the averaged influence of the Schwadron-Parker HMF model only accounts for up to  $\sim 3\%$  of the  $\lambda_{\theta\theta}$  enhancement found in the Parker field in chapter 6 during the time period from 1995.6 to 1996.3 and for the diffusion coefficients employed in this work.

## Conclusions

In this chapter, a qualitative investigation of the electron intensities in a Fisk-type heliospheric magnetic field became possible for the first time. Therefore, the 7 MeV electron flux in the heliosphere could be used as a remote sensing method for the HMF structure. To achieve this, the Schwadron-Parker hybrid HMF (Hitge and Burger,

2010) was chosen as the most adequate representation of a Fisk-type field. Simulations of the 7 MeV electron flux in the heliosphere reveal 26-day variations at mid to high latitudes in the inner heliosphere. The analysis of the Ulysses/KET 2.5 – 7 MeV electron data lead to the conclusion, that a 26-day variation can also be found in the electron count rate at mid to high latitudes of the Ulysses trajectory between 1995.6 and 1996.3. A further analysis of proton and solar wind speed data could exclude CIRs or the solar wind to cause the electron variations. These results lead to the conclusion that the HMF structure is Fisk-like at the corresponding latitudes during the considered period of time, a finding which could not be derived from magnetic field measurements in the inner heliosphere so far (Roberts et al., 2007; Burger et al., 2008).

In addition, realistic parameters for the Fisk theory could be derived from a comparison of model computations and Ulysses/KET measurements. The important Fisk-angle  $\beta$  was estimated to be in the order of  $30^\circ$  in the original theory and related studies (Fisk, 1996; Zurbuchen et al., 1997; Roberts et al., 2007). This work shows, however, that  $\beta$  was overestimated so far and is found to be in the order of  $6^\circ$  for the investigated time period and diffusion coefficients. The consequence of this finding is a low Fisk effect in the HMF structure. The field appears to be almost Parker-like with the field lines only connecting narrow bands in latitude, while connections from low latitudes to the polar regions were expected from the original Fisk theory.

With the new value of the Fisk angle  $\beta$ , the influence of the Schwadron-Parker HMF structure on the latitudinal particle diffusion during solar minimum conditions was investigated quantitatively. Ferreira (2002) proposed the latitudinal diffusion coefficient to be increased during solar minimum conditions in the fast solar wind due to two possible reasons: high turbulence in the fast solar wind (Jokipii et al., 1995) and a Fisk-type HMF structure. For 7 MeV electrons, the increase of the latitudinal diffusion coefficient is shown to be a factor of eight in chapter 6. The fraction of this enhancement caused by a Schwadron-Parker HMF with  $\beta = 6^\circ$  is found to be around 3% averaged over a solar rotation in the inner heliosphere ( $r \leq 20$  AU). Therefore, this work demonstrates that the HMF structure contains a Fisk-type component. However, the Fisk-type HMF structure only plays a minor role for the latitudinal diffusion in the long-term modulation of 7 MeV electrons.

# Chapter 8

## Summary and Conclusions

In this work the propagation of 7 MeV electrons in the heliospheric magnetic field was investigated for the first time in a 3D and time-dependent model for two different models of the heliospheric magnetic field: the Parker field and, for the first time, also for a Fisk-type field. The computed electron intensities were compared to the corresponding measurements of the IMP-8, SOHO and Ulysses spacecraft. The main results of these investigations are presented in the following.

### The Electron Flux in a Parker HMF

For the first time, the compound approach for the diffusion tensor suggested by Ferreira et al. (2003b) was applied to a time-dependent simulation of the 7 MeV electron flux in the heliosphere. The corresponding count rates of the IMP-8, SOHO and Ulysses spacecraft were reproduced over almost two solar cycles (1990 – 2009) relating the parallel diffusion coefficient  $\kappa_{\parallel}$  to the magnetic field strength of the HMF measured at the Earth's orbit. To achieve this, the perpendicular diffusion coefficients  $\kappa_{\perp\theta}$  and  $\kappa_{\perp r}$  were varied with the solar cycle phases.  $\kappa_{\perp\theta}$  was increased by a factor of eight in the fast solar wind during solar minimum conditions. The time evolution of the polar coronal holes during the transition from solar maximum to solar minimum and back was discussed. This work finds the transition to be best described by a polar coronal hole opening over the solar poles and spreading towards lower latitudes during the development from solar maximum to minimum conditions. In agreement with Ferreira et al. (2001b) and Lange et al. (2006),  $\kappa_{\perp r}$  was increased globally by 35% during solar maximum conditions.

In this investigation a time shift of the solar cycle dependence of  $\kappa_{\perp\theta}$ ,  $\kappa_{\perp r}$  and  $u_{sw}$  with respect to the sunspot cycle was found. The transitions from solar maximum to minimum conditions and back are centered around  $t_0^{(1)} = 1990.85$ ,  $t_0^{(2)} = 1995.84$ ,  $t_0^{(3)} = 2001.75$  and  $t_0^{(4)} = 2008.30$  with a transition time of 1.36 years. The transition from solar minimum to maximum conditions around  $t_0^{(2)} = 1995.84$  is consistent with Lange et al. (2006). However, the latter authors employ only one transition between

the solar cycle phases. For the first time, the full solar cycle evolution between 1990 and 2009 was discussed in this work. Especially the last transition back to solar maximum conditions employed in this work has not been found in any measured data describing the solar cycle yet.

The compound approach relating the parallel diffusion coefficient to the HMF strength measured at the Earth's orbit by  $\kappa_{\parallel} \propto (B_0/B)^n$ ,  $B_0 = 5$  nT, leads to a good agreement of the model results and the corresponding electron count rates measured with IMP-8, SOHO and Ulysses within the same simulation, consistent to the results of Ferreira et al. (2003a) and Ferreira and Potgieter (2004) for high energy electrons, protons and helium. This work showed that the exponent  $n$  varies between 0 and  $-1$  during the solar cycle for 7 MeV electrons. The approach relating  $n$  to the tilt angle of the heliospheric magnetic field by  $n = -\alpha/\alpha_0$  could reproduce the spacecraft data best with  $\alpha_0 = 80^\circ$ . Note that Ferreira et al. (2003a) and Ferreira and Potgieter (2004) use positive values of  $n$  for high energy particles. This work shows for the first time that the electron count rates at the Earth's orbit and Ulysses can be reproduced applying only the compound approach for the diffusion tensor, while Lange et al. (2006) suggest a varying source strength of the Jovian magnetosphere and Lange and Fichtner (2008) introduce the Kronian magnetosphere as a second planetary electron source at low energies.

## 7 MeV Electron Intensities in a Fisk-type HMF

The Fisk model for the heliospheric magnetic field could not be verified with magnetic field measurements so far. The simulations performed in this work showed that a Fisk-type field structure leads to strong variations of the diffusion parameters on time scales of the solar rotation for electrons at energies of 7 MeV. Therefore, a qualitative study of the 7 MeV electron intensities in a Schwadron-Parker HMF (Hitge and Burger, 2010) was employed to find a remote sensing method for the HMF structure. The simulations performed in this work revealed a strong variation of the electron flux at mid to high latitudes in the inner heliosphere, the space accessible to the Ulysses spacecraft. Hence, the 2.5 – 7 MeV electron count rates of Ulysses were investigated for 26-day variations finding these periodicities between 1995.6 and 1996.3 when Ulysses was at high heliographic latitudes. The analysis of electron measurements in the range of a few MeV performed in this work suggests for the first time the existence of a Fisk-type HMF and showed, that the 2.5 – 7 MeV electron count rate measured by Ulysses at high latitudes contains the imprint of a Fisk-type heliospheric magnetic field.

From a comparison of the simulation results to the measured electron data, a realistic value of the Fisk angle  $\beta$  was derived. This angle determines the strength of the Fisk effect in the heliospheric magnetic field and was estimated to be in the order of  $\beta \approx 30^\circ$  in the original theory (Fisk, 1996; Zurbuchen et al., 1997). This value was employed in most investigations of the Fisk field, especially in comparisons to HMF measurements (Roberts et al., 2007). This work, however, could demonstrate it to be

much lower than assumed so far. The best fit could be obtained for  $\beta \approx 6^\circ$ , consistent to the finding of Roberts et al. (2007) who conclude that – if the Fisk theory is applicable –  $\beta$  was overestimated so far.

Based on the new value for the Fisk angle, the consequences for the field structure can be discussed. With  $\beta \approx 6^\circ$ , the Schwadron-Parker HMF appears to be almost Parker-like, with field lines merely connecting narrow bands in latitude. The study of the perpendicular diffusion coefficient  $\kappa_{\perp\theta}$  demonstrated, that the Fisk-type HMF structure shows only a low influence in the long-term modulation of 7 MeV electrons. In the investigation of the electron modulation in a Parker field, an enhancement of  $\kappa_{\perp\theta}$  by a factor of eight was needed to reproduce the Ulysses measurements at high latitudes. This enhancement was motivated by high turbulence in the fast solar wind or a Fisk-type HMF structure. This work, however, shows that the Fisk field only accounts for  $\sim 3\%$  of this increase in  $\kappa_{\perp\theta}$ . Therefore, the investigations performed in this work show that the Ulysses electron count rate reveals a Fisk component of the heliospheric magnetic field. However, the Fisk field only has a minor influence in the long-term modulation of 2.5 – 7 MeV electrons in the heliosphere.



# Chapter 9

## Future Prospects

The investigations performed in this work addressed two problems previously unsolved in heliophysics. The compound approach for the diffusion tensor (Ferreira et al., 2003b) was shown to be applicable for electron propagation in a Parker field in the energy range of a few MeV. The corresponding count rates of the three spacecraft IMP-8, SOHO and Ulysses were reproduced over a time period of almost two solar cycles. It was demonstrated that the heliospheric magnetic field contains a Fisk field component and realistic parameters for the Fisk theory were derived from a comparison of electron simulations and the Ulysses electron count rate. However, new questions arise from the results presented in this work.

### Long-term Modulation of Energetic Electrons in a Parker Field

Although this work presents simulation results for the 7 MeV electron flux in the heliosphere to be conform to the electron count rates measured by IMP-8, SOHO/EPHIN and Ulysses/KET, additional investigation is needed to gain a deeper insight into the open questions found in the current investigation.

The time-period of almost two solar cycles covered by this work can be extended into the past. The IMP-8 spacecraft was launched in 1973 and continuously measured the electron count rate at energies of 2 – 12 MeV. Additionally, the two Helios missions, Pioneer 10 and 11, as well as the Voyager 1 and 2 spacecraft supplied electron count rates to be compared to simulation data.

This work employs a solar cycle dependence of  $\kappa_{\perp r}$ ,  $\kappa_{\perp \theta}$  and  $u_{\text{SW}}$  which is shifted with respect to the sunspot cycle. Especially the increase of the electron count rate found in the Ulysses/KET data in 2008 needs a transition from solar minimum to maximum conditions to be explained by the model. Recent studies by Jiang et al. (2010) find a similar behaviour of the tilt angle in their model which is at least partly consistent with the time shift found in this work. The transition from solar minimum to solar maximum conditions around  $t_0 = 2008.30$  is, however, not found in any

measured data describing the solar cycle. Therefore, additional investigation is needed to find the cause of the time shift between the solar cycle dependence of the parameters determining the propagation of energetic particles in the heliosphere and the sunspot cycle.

The step-like increase found in the Ulysses/KET electron count rate in 1996/97 is fitted best by simulations employing an exponent  $n < -1$ , while  $0 > n > -1$  is valid for the remaining time periods. This leads to the question which additional effects cause the special behaviour of  $n$  during the years 1996 and 1997.

The comparison of the simulation data to the SOHO/EPHIN electron count rate reveals a discrepancy after the year 2005. While the EPHIN data increases during this time period, the simulations result in a decreasing electron count rate. To find the reason for this disagreement, a comparison to other spacecraft measurements obtained near the Earth's orbit as well as an analysis of the instrument are needed.

Recently, new approaches to the computation of the parallel and perpendicular diffusion coefficients were developed (see e.g. Teufel and Schlickeiser, 2002, 2003; Matthaeus et al., 2003; Shalchi et al., 2004). These new theories need to be applied to a 3D and time-dependent propagation model and tested against spacecraft count rates of energetic charged particles.

## The 7 MeV Electron Flux in a Fisk-type HMF

The qualitative investigation of the 7 MeV electron flux in a Fisk-type field revealed for the first time that the corresponding electron measurements of the Ulysses spacecraft contain the imprint of such a field structure. However, the reproduction of the count rates in a time-dependent simulation is a complex problem. Therefore, an important problem to be solved is a quantitative reproduction of the Ulysses count rates in a Fisk-type HMF. One possibility to achieve this aim is the application of different theories describing the diffusion coefficients (see e.g. Teufel and Schlickeiser, 2002, 2003; Matthaeus et al., 2003; Shalchi et al., 2004). Additionally, a refinement of the statistical methods employed for the comparison of the simulation data to the measured count rates is needed, e.g. the standard deviations of the Ulysses count rates and the simulation data with noise could be used as a measure for the agreement between both data sets.

The analytic expression of the Fisk-type Schwadron-Parker HMF model (Hitge and Burger, 2010) needs to be tested against magnetic field measurements with the new parameter  $\beta \approx 6^\circ$  found in this work to see whether this field structure can be confirmed with existing HMF measurements. If the predicted variations of the field vector are masked by other effects in the inner heliosphere, this kind of study can reveal hints how or where in the heliosphere the Fisk-type HMF structure can be found with future magnetic field measurements.

Finally, the influence of a Fisk-type field on the long-term modulation of energetic charged particles needs to be tested in a time-dependent simulation. To achieve this,



a new approach describing the time-dependence of the Fisk-angle  $\beta$  will be needed taking into account the results of these investigations.

The achievements presented in this work put forward several open questions which need to be answered in the further discussion of particle propagation and the Fisk theory. However, this work showed the existence of a Fisk-type HMF structure employing the electron transport in the heliosphere as a remote sensing method. The influence of the Fisk field on the long-term modulation of electrons in the energy range of a few MeV could be estimated to be almost negligible. Hence, the results of this work present an significant step forward in the discussion of particle propagation and the heliospheric magnetic field structure, which can be used as a basis for future research.



# Bibliography

- Abramowitz, M., Stegun, I. A. (Eds.), 1965. Handbook of Mathematical Functions. Dover Publications.
- Adler Planetarium, Chicago, 2010. Cosmic Ray Shielding. [http://www.nasa.gov/mission\\_pages/ibex/allsky\\_visuals.html](http://www.nasa.gov/mission_pages/ibex/allsky_visuals.html) (visited on January 6, 2010).
- Alanko-Huotari, K., Usoskin, I. G., Mursula, K., Kovaltsov, G. A., 2007. Cyclic variations of the heliospheric tilt angle and cosmic ray modulation. *Advances in Space Research* 40, 1064–1069.
- Balogh, A., Lanzerotti, L. J., Suess, S. T., 2007. The Heliosphere through the Solar Activity Cycle, 1st Edition. Springer Berlin.
- Balogh, A., Smith, E. J., Tsurutani, B. T., Southwood, D. J., Forsyth, R. J., Horbury, T. S., May 1995. The Heliospheric Magnetic Field Over the South Polar Region of the Sun. *Science* 268, 1007–1010.
- Biermann, L., 1951. Kometenschweife und solare Korpuskularstrahlung. *Zeitschrift für Astrophysik* 29, 274–286.
- Blandford, R. D., Ostriker, J. P., Apr. 1978. Particle acceleration by astrophysical shocks. *Astrophys. J. Lett.* 221, L29–L32.
- Blom, J. G., Verwer, J. G., 1994. VLUGR3: A Vectorizable Adaptive Grid Solver for PDEs in 3D. I. Algorithmic Aspects and Applications. *Applied Numerical Mathematics* 16 (1-2), 129–156.
- Blom, J. G., Verwer, J. G., 1996. Algorithm 759: VLUGR3: A Vectorizable Adaptive Grid Solver for PDEs in 3D. II. Code Description. *ACM Transactions on Mathematical Software* 22 (3), 329–347.
- Borrmann, T., Fichtner, H., 2005. On the dynamics of the heliosphere on intermediate and long time-scales. *Adv. Space Res.* 35, 2091–2101.
- Box, G. E. P., Muller, M. E., 1958. A Note on the Generation of Random Normal Deviates. *The Annals of Mathematical Statistics* 29 (2), 610–611.

- 
- Bronstein, I. N., Semendjajew, K. A., Musiol, G., Muehlig, H., 7 2008. Taschenbuch der Mathematik, 7th Edition. Harri Deutsch.
- Burger, R. A., 2005. Cosmic-ray modulation and the heliospheric magnetic field. *Advances in Space Research* 35, 636–642.
- Burger, R. A., Hitge, M., Dec. 2004. The Effect of a Fisk-Type Heliospheric Magnetic Field on Cosmic-Ray Modulation. *Astrophys. J. Lett.* 617, L73–L76.
- Burger, R. A., Krüger, T. P. J., Hitge, M., Engelbrecht, N. E., Feb. 2008. A fisk-parker hybrid heliospheric magnetic field with a solar-cycle dependence. *Astrophys. J.* 674, 511–519.
- Burger, R. A., Potgieter, M. S., Heber, B., Dec. 2000. Rigidity dependence of cosmic ray proton latitudinal gradients measured by the Ulysses spacecraft: Implications for the diffusion tensor. *J. Geophys. Res.* 105, 27447–27456.
- Büsching, I., Kopp, A., Pohl, M., Schlickeiser, R., Perrot, C., Grenier, I., Jan. 2005. Cosmic-Ray Propagation Properties for an Origin in Supernova Remnants. *Astrophys. J.* 619, 314–326.
- Charbonneau, P., Jun. 2005. Dynamo models of the solar cycle. *Living Reviews in Solar Physics* 2, 2ff.
- Chenette, D. L., Conlon, T. F., Simpson, J. A., 1974. Burst of relativistic electrons from Jupiter observed in interplanetary space with the time variation of the planetary rotation period. *J. Geophys. Res.* 79, 3551–3558.
- Choudhuri, A. R., Jun. 2000. The current status of kinematic solar dynamo models. *Journal of Astrophysics and Astronomy* 21, 373–377.
- Choudhuri, A. R., 2008. How far are we from a standard model of the solar dynamo? *Advances in Space Research* 41, 868–873.
- Dikpati, M., Gilman, P. A., Aug. 2007. Global solar dynamo models: simulations and predictions of cyclic photospheric fields and long-term non-reversing interior fields. *New Journal of Physics* 9, 297ff.
- Domingo, V., Fleck, B., Poland, A. I., Dec. 1995. The SOHO Mission: an Overview. *Solar Physics* 162, 1–2.
- Drury, L. O., Völk, J. H., Aug. 1981. Hydromagnetic shock structure in the presence of cosmic rays. *Astrophys. J.* 248, 344–351.
- Dunzlaff, P., Heber, B., Kopp, A., Rother, O., Müller-Mellin, R., Klassen, A., Gómez-Herrero, R., Wimmer-Schweingruber, R., Oct. 2008. Observations of recurrent cosmic ray decreases during solar cycles 22 and 23. *Annales Geophysicae* 26, 3127–3138.

- Engelbrecht, N. E., 2009. Private communication.
- Engelbrecht, N. E., Burger, R. A., Apr. 2010. Effects of various dissipation range onset models on the 26-day variations of low-energy galactic cosmic-ray electrons. *Advances in Space Research* 45, 1015–1025.
- Eraker, J. H., Jun. 1982. Origins of the low-energy relativistic interplanetary electrons. *Astrophys. J.* 257, 862–880.
- Erdős, G., Balogh, A., 2005. In situ observations of magnetic field fluctuations. *Advances in Space Research* 35, 625–635.
- Erlykin, A. D., Sloan, T., Wolfendale, A. W., Jan. 2009. Solar activity and the mean global temperature. *Environmental Research Letters* 4 (1), 014006.
- ESA Web Site, 1997. Ulysses First Solar Orbit. <http://sci.esa.int/science-e-media/img/ee/Ulysses-Orbit-1.jpg> (visited on November 17, 2009).
- Evans, G., Blackledge, J., Yardley, P., 11 1999. *Numerical Methods for Partial Differential Equations*, 1st Edition. Springer.
- Ferrando, P., May 1997. MeV to GeV electron propagation and modulation: results of the KET-telescope onboard ULYSSES. *Advances in Space Research* 19, 905–915.
- Ferrando, P., 1999. Observation of a  $\sim 7$  MeV Electron Super-flux at 5 AU by Ulysses. In: *International Cosmic Ray Conference*. Vol. 7 of *International Cosmic Ray Conference*. pp. 135–138.
- Ferreira, S. E. S., 2002. *The Heliospheric Transport of Galactic Cosmic Rays and Jovian Electrons*. Ph.D. thesis, Potchefstroomse Universiteit, South Africa.
- Ferreira, S. E. S., Potgieter, M. S., Mar. 2004. Long-Term Cosmic-Ray Modulation in the Heliosphere. *Astrophys. J.* 603, 744–752.
- Ferreira, S. E. S., Potgieter, M. S., Burger, R. A., Heber, B., 2000. Modulation effects of anisotropic perpendicular diffusion on cosmic ray electron intensities in the heliosphere. *J. Geophys. Res.* 105, 18305–18314.
- Ferreira, S. E. S., Potgieter, M. S., Burger, R. A., Heber, B., Fichtner, H., 2001a. The modulation of Jovian and galactic electrons in the heliosphere. I. Latitudinal transport of a few-MeV electrons. *J. Geophys. Res.* 106 (A11), 24979–24988.
- Ferreira, S. E. S., Potgieter, M. S., Burger, R. A., Heber, B., Fichtner, H., Lopate, C., Dec. 2001b. Modulation of Jovian and galactic electrons in the heliosphere: II. Radial transport of a few MeV electrons. *J. Geophys. Res.* 106, 29313–29322.

- Ferreira, S. E. S., Potgieter, M. S., Heber, B., Aug. 2003a. Particle drift effects on cosmic ray modulation during solar maximum. *Advances in Space Research* 32, 645–650.
- Ferreira, S. E. S., Potgieter, M. S., Heber, B., Fichtner, H., Jun. 2003b. Charge-sign dependent modulation in the heliosphere over a 22-year cycle. *Annales Geophysicae* 21, 1359–1366.
- Ferreira, S. E. S., Potgieter, M. S., Heber, B., Fichtner, H., Burger, R. A., Ferrando, P., 2001. A study of the compatibility between observations and model simulations for Jovian and galactic electrons. *Advances in Space Research* 27, 553–558.
- Ferreira, S. E. S., Potgieter, M. S., Heber, B., Fichtner, R., Kissmann, R., Aug. 2003c. Transport of a few-MEV jovian and galactic electrons at solar maximum. *Advances in Space Research* 32, 669–674.
- Ferreira, S. E. S., Potgieter, M. S., Scherer, K., Nov. 2007. Transport and acceleration of anomalous cosmic rays in the inner heliosheath. *Journal of Geophysical Research (Space Physics)* 112, 11101.
- Fichtner, H., Feb. 2001. Anomalous Cosmic Rays: Messengers from the Outer Heliosphere. *Space Science Reviews* 95, 639–754.
- Fichtner, H., Potgieter, M., Ferreira, S., Burger, A., Jun. 2000. On the propagation of Jovian electrons in the heliosphere: transport modelling in 4-D phase space. *Geophys. Res. Lett.* 27, 1611–1614.
- Fichtner, H., Scherer, K., 2000. The heliosphere: a brief overview. In: Scherer, K., Fichtner, H., Marsch, E. (Eds.), *The Outer Heliosphere: Beyond the Planets*. pp. 1–11.
- Fisk, L. A., Sep. 1976. Solar modulation of galactic cosmic rays. IV - Latitude-dependent modulation. *J. Geophys. Res.* 81, 4646–4650.
- Fisk, L. A., 1996. Motion of the footpoints of heliospheric magnetic field lines at the Sun: Implications for recurrent energetic particle events at high heliographic latitudes. *J. Geophys. Res.* 101, 15547–15553.
- Fisk, L. A., 2005. Journey into the unknown beyond. *Science* 309, 2016–2017.
- Fisk, L. A., Schwadron, N. A., Zurbuchen, T. H., Sep. 1999a. Acceleration of the fast Solar Wind by the Emergence of new Magnetic Flux. *J. Geophys. Res.* 104, 19765–19772.
- Fisk, L. A., Zurbuchen, T. H., Schwadron, N. A., Aug. 1999b. On the Coronal Magnetic Field: Consequences of Large-Scale Motions. *Astrophys. J.* 521, 868–877.

- Forsyth, R. J., 2001. Solar Magnetic Field Reversal. <http://www.sp-ph.ic.ac.uk/~forsyth/reversal> (visited on April 20, 2010).
- Forsyth, R. J., Balogh, A., Smith, E. J., Nov. 2002. The underlying direction of the heliospheric magnetic field through the ulysses first orbit. *Journal of Geophysical Research (Space Physics)* 107, 1405.
- Forsyth, R. J., Balogh, A., Smith, E. J., Erdös, G., McComas, D. J., Jan. 1996. The underlying parker spiral structure in the ulysses magnetic field observations, 1990-1994. *J. Geophys. Res.* 101, 395–404.
- Forsyth, R. J., Balogh, A., Smith, E. J., Murphy, N., McComas, D. J., 1995. The underlying magnetic field direction in ulysses observations of the southern polar heliosphere. *Geophys. Res. Lett.* 22, 3321–3324.
- Galilei, G., Welser, M., de Filiis, A., 1613. *Istoria E dimostrazioni intorno alle macchie solari E loro accidenti comprese in tre lettere scritte all'illvstrissimo signor Marco Velseri.* Roma, G. Mascadi, 1613.
- Giacalone, J., Jan. 1998. Cosmic-Ray Transport Coefficients. *Space Science Reviews* 83, 351–363.
- Giacalone, J., Jokipii, J. R., July 1999. The transport of cosmic rays across a turbulent magnetic field. *Astrophys. J.* 520 (1), 204–214.
- Gleeson, L. J., Axford, W. I., Dec. 1968. Solar Modulation of Galactic Cosmic Rays. *Astrophys. J.* 154, 1011–1026.
- Goddard Space Flight Center, 2009. NASA OMNIWeb Data Explorer. <http://omniweb.gsfc.nasa.gov/form/dx1.html> (visited on January 15, 2009).
- Gosling, J. T., Hundhausen, A. J., Bame, S. J., May 1976. Solar wind stream evolution at large heliocentric distances - Experimental demonstration and the test of a model. *J. Geophys. Res.* 81, 2111–2122.
- Gosling, J. T., Pizzo, V. J., Jul. 1999. Formation and Evolution of Corotating Interaction Regions and their Three Dimensional Structure. *Space Science Reviews* 89, 21–52.
- Hale, G. E., Nov. 1908. On the probable existence of a magnetic field in sun-spots. *Astrophys. J.* 28, 315–343.
- Hale, G. E., Ellerman, F., Nicholson, S. B., Joy, A. H., Apr. 1919. The magnetic polarity of sun-spots. *Astrophys. J.* 49, 153–178.
- Hamilton, D. C., Simpson, J. A., Mar. 1979. Jovian electron propagation out of the solar equatorial plane - Pioneer 11 observations. *Astrophys. J. Lett.* 228, L123–L127.

- Harvey, K. L., Recely, F., dec 2002. Polar Coronal Holes During Cycles 22 and 23. *Solar Physics* 211, 31–52.
- Hattingh, M., 1998. The Modulation of Galactic Cosmic Rays in a Three-Dimensional Heliosphere. Ph.D. thesis, Potchefstroomse Universiteit vir Christelike Hoër Onderwys, R.S.A.
- Hattingh, M., Burger, R. A., 1995. A new simulated wavy neutral sheet drift model. *Adv. Space Res.* 16 (9), 213–216.
- Heber, B., Bothmer, V., Dröge, W., Kunow, H., Müller-Mellin, R., Posner, A., Ferrando, P., Raviart, A., Raviart, A., Paizis, C., McComas, D., Forsyth, R. J., Szabo, A., Lazarus, A. J., Dec. 1997. Spatial Evolution of 26-day Recurrent Galactic Cosmic Ray Decreases: Correlated Ulysses COSPIN/KET and SOHO COSTEP Observations. In: A. Wilson (Ed.), *Correlated Phenomena at the Sun, in the Heliosphere and in Geospace*. Vol. 415 of ESA Special Publication. pp. 331–336.
- Heber, B., Dröge, W., Ferrando, P., Haasbroek, L. J., Kunow, R., Müller-Mellin, R., Paizis, C., Potgieter, M. S., Raviart, A., Wibberenz, G., 1996. Spatial variation of  $> 40$  MeV/n nuclei fluxes observed during the Ulysses rapid latitude scan. *Astron. Astrophys.* 316, 538–546.
- Heber, B., Kopp, A., Gieseler, J., Müller-Mellin, R., Fichtner, H., Scherer, K., Potgieter, M. S., Ferreira, S. E. S., Jul. 2009. Modulation of Galactic Cosmic Ray Protons and Electrons During an Unusual Solar Minimum. *Astrophys. J.* 699, 1956–1963.
- Heber, B., Potgieter, M. S., Ferreira, S. E. S., Dalla, S., Kunow, H., Müller-Mellin, R., Wibberenz, G., Paizis, C., Sarri, G., Marsden, R. G., McKibben, R. B., Zhang, M., Jan. 2007. An overview of Jovian electrons during the distant Ulysses Jupiter flyby. *Planetary and Space Science* 55, 1–11.
- Hess, V. F., Nov. 1911. Messungen der durchdringenden Strahlung bei zwei Freiballonfahrten. Mitteilungen aus dem Institut für Radiumforschung, Sitzungsberichte der mathematisch-naturw. Klasse der kaiserlichen Akademie der Wissenschaften, Band CXX, Abteilung IIa, Jahrgang 1911, Wien, 1–11.
- Hess, V. F., 1912. Beobachtungen der durchdringenden Strahlung bei sieben Freiballonfahrten. Mitteilungen aus dem Institut für Radiumforschung, Sitzungsberichte der mathematisch-naturw. Klasse der kaiserlichen Akademie der Wissenschaften, Band CXXI, Abteilung IIa, Jahrgang 1912, Wien. Heft VIII-X, zweiter Halbband, 2001–2032.
- Hitge, M., Burger, R. A., 2008. The Effect of a Latitudinal Dependent Solar Wind Speed on Cosmic-Ray Modulation in a Fisk-type Heliospheric Magnetic Field. In: *International Cosmic Ray Conference*. Vol. 1 of *International Cosmic Ray Conference*. pp. 449–450.



- Hitge, M., Burger, R. A., Jan. 2010. Cosmic ray modulation with a Fisk-type heliospheric magnetic field and a latitude-dependent solar wind speed. *Advances in Space Research* 45, 18–27.
- Hoeksema, J. T., Apr. 1995. The Large-Scale Structure of the Heliospheric Current Sheet During the ULYSSES Epoch. *Space Science Reviews* 72, 137–148.
- Jiang, J., Cameron, R., Schmitt, D., Schüssler, M., Jan. 2010. Modeling the Sun’s Open Magnetic Flux and the Heliospheric Current Sheet. *Astrophys. J.* 709, 301–307.
- Jiang, J., Chatterjee, P., Choudhuri, A. R., Nov. 2007. Solar activity forecast with a dynamo model. *Mon. Not. R. Astron. Soc.* 381, 1527–1542.
- Jokipii, J. R., Nov. 1966. Cosmic-Ray Propagation. I. Charged Particles in a Random Magnetic Field. *Astrophys. J.* 146, 480–487.
- Jokipii, J. R., Aug. 2001. Latitudinal heliospheric magnetic field: Stochastic and causal components. *J. Geophys. Res.* 106, 15841–15848.
- Jokipii, J. R., Jul. 2008. Solar System: A shock for Voyager 2. *Nature* 454, 38–39.
- Jokipii, J. R., Kopriva, D. A., Nov. 1979. Effects of particle drift on the transport of cosmic rays. III - Numerical models of galactic cosmic-ray modulation. *Astrophys. J.* 234, 384–392.
- Jokipii, J. R., Kóta, J., Jan. 1989. The polar heliospheric magnetic field. *Geophys. Res. Lett.* 16, 1–4.
- Jokipii, J. R., Kóta, J., Apr. 1995. Three-Dimensional Cosmic-Ray Simulations: Heliographic Latitude and Current-Sheet Tilt. *Space Science Reviews* 72, 379–384.
- Jokipii, J. R., Kóta, J., Giacalone, J., Horbury, T. S., Smith, E. J., 1995. Interpretation and consequences of large-scale magnetic variances observed at high heliographic latitude. *Geophys. Res. Lett.* 22, 3385–3388.
- Jokipii, J. R., Levy, E. H., Hubbard, W. B., 1977. Effects of particle drift on cosmic-ray transport. I. General properties, application to solar modulation. *Astrophys. J.* 213 (3), 861–868.
- Kallenrode, M.-B., 2004. *Space Physics*, 3rd Edition. Springer.
- Kissmann, R., 2002. Modellierung des zeitabhängigen Transports energetischer Elektronen in der Heliosphäre. Diplomarbeit, Ruhr-Universität Bochum.
- Kissmann, R., Fichtner, H., Ferreira, S. E. S., May 2004. The influence of CIRs on the energetic electron flux at 1 AU. *Astron. Astrophys.* 419, 357–363.

- Kissmann, R., Fichtner, H., Heber, B., Ferreira, S. E. S., Potgieter, M. S., Aug. 2003. First results of a new 3-D model of the time-dependent modulation of electrons in the heliosphere. *Advances in Space Research* 32, 681–686.
- Kobylinski, Z., 2001. Comparison of the Fisk Magnetic Field with the Standard Parker IMF: Consequences for Diffusion Coefficients. *Advances in Space Research* 27, 541–546.
- Kóta, J., Jokipii, J. R., Feb. 1983. Effects of drift on the transport of cosmic rays. VI - A three-dimensional model including diffusion. *Astrophys. J.* 265, 573–581.
- Kóta, J., Jokipii, J. R., May 1995a. Corotating Variations of Cosmic Rays near the South Heliographic Pole. *Science* 268, 1024–1025.
- Kóta, J., Jokipii, J. R., Jan. 1998. Modeling of 3-D Corotating Cosmic-Ray Structures in the Heliosphere. *Space Science Reviews* 83, 137–145.
- Kóta, J., Jokipii, R. J., 1995b. 3-D Distribution of Cosmic Rays in the Outer Heliosphere. In: *International Cosmic Ray Conference*. Vol. 4 of *International Cosmic Ray Conference*. pp. 680–683.
- Kóta, J., Jokipii, R. J., 1997. 3-D simulation of heliospheric transport: A comparison of models. In: *International Cosmic Ray Conference*. Vol. 2 of *International Cosmic Ray Conference*. p. 25ff.
- Krüger, T. P. J., 2005. The Effect of a Fisk-Parker Hybrid Magnetic Field on Cosmic Rays in the Heliosphere. Master's thesis, School of Physics, North-West University, 2520 Potchefstroom, South Africa.
- Krieger, A. S., Timothy, A. F., Roelof, E. C., Apr. 1973. A Coronal Hole and Its Identification as the Source of a High Velocity Solar Wind Stream. *Solar Physics* 29, 505–525.
- Krupp, N., Woch, J., Lagg, A., Espinosa, S. A., Livi, S., Krimigis, S. M., Mitchell, D. G., Williams, D. J., Cheng, A. F., Mauk, B. H., McEntire, R. W., Armstrong, T. P., Hamilton, D. C., Gloeckler, G., Dandouras, J., Lanzerotti, L. J., Aug. 2002. Leakage of energetic particles from Jupiter's dusk magnetosphere: Dual spacecraft observations. *Geophys. Res. Lett.* 29 (15), 1736.
- Krupp, N., Woch, J., Lagg, A., Livi, S., Mitchell, D. G., Krimigis, S. M., Dougherty, M. K., Hanlon, P. G., Armstrong, T. P., Espinosa, S. A., Aug. 2004. Energetic particle observations in the vicinity of Jupiter: Cassini MIMI/LEMMS results. *Journal of Geophysical Research (Space Physics)* 109, A09S10.
- Lange, D., 2004. Simulation der Modulation Kosmischer Strahlung über einen solaren Zyklus. Diplomarbeit, Ruhr-Universität Bochum.

- Lange, D., Fichtner, H., May 2008. Are there Kronian electrons in the inner heliosphere? *Astron. Astrophys.* 482, 973–979.
- Lange, D., Fichtner, H., Kissmann, R., Apr. 2006. Time-dependent 3D modulation of Jovian electrons. Comparison with Ulysses/KET observations. *Astron. Astrophys.* 449, 401–410.
- Langner, U. W., de Jager, O. C., Potgieter, M. S., 2001. On the local interstellar spectrum for cosmic ray electrons. *Advances in Space Research* 27, 517–522.
- Lomb, N. R., Feb. 1976. Least-squares frequency analysis of unequally spaced data. *Astrophys. and Space Sci.* 39, 447–462.
- Longair, M. S., 1992. High energy astrophysics. Vol.1: Particles, photons and their detection, 2nd Edition. Cambridge University Press.
- Lopate, C., 1991. Jovian and galactic electrons (2-30 GeV) in the heliosphere from 1 to 50 AU. In: *Proceedings of the 23rd International Cosmic Ray Conference*.
- Matthaeus, W. H., Qin, G., Bieber, J. W., Zank, G. P., 2003. Nonlinear collisionless perpendicular diffusion of charged particles. *Astrophys. J. Lett.* 590 (1), L53–L56.
- Maunder, E. W., May 1905. Magnetic disturbances and associated sun-spots. *Mon. Not. R. Astron. Soc.* 65, 666–682.
- McComas, D. J., Allegrini, F., Bochsler, P., Bzowski, M., Christian, E. R., Crew, G. B., DeMajistre, R., Fahr, H., Fichtner, H., Frisch, P. C., Funsten, H. O., Fuselier, S. A., Gloeckler, G., Gruntman, M., Heerikhuisen, J., Izmodenov, V., Janzen, P., Knappenberger, P., Krimigis, S., Kucharek, H., Lee, M., Livadiotis, G., Livi, S., MacDowall, R. J., Mitchell, D., Möbius, E., Moore, T., Pogorelov, N. V., Reisenfeld, D., Roelof, E., Saul, L., Schwadron, N. A., Valek, P. W., Vanderspek, R., Wurz, P., Zank, G. P., Nov. 2009. Global Observations of the Interstellar Interaction from the Interstellar Boundary Explorer (IBEX). *Science* 326, 959–.
- McComas, D. J., Elliott, H. A., Schwadron, N. A., Gosling, J. T., Skoug, R. M., Goldstein, B. E., May 2003. The three-dimensional solar wind around solar maximum. *Geophys. Res. Lett.* 30, 1517.
- McDonald, F. B., Cline, T. L., Simnett, G. M., 1972. Multivarious temporal variations of low-energy relativistic cosmic-ray electrons. *J. Geophys. Res.* 77, 2213–2231.
- McKibben, R. B., Connell, J. J., Lopate, C., Simpson, J. A., Zhang, M., Dec. 1996. Observations of galactic cosmic rays and the anomalous helium during ULYSSES passage from the south to the north solar pole. *Astron. Astrophys.* 316, 547–554.
- Morioka, A., Tsuchiya, F., Misawa, H., Jan. 1997. Modulation of Jovian electrons by the solar wind. *Advances in Space Research* 20, 205ff.

- Moses, D., Feb. 1987. Jovian electrons at 1 AU - 1978-1984. *Astrophys. J.* 313, 471–486.
- Müller-Mellin, R., Kunow, H., Fleißner, V., Pehlke, E., Rode, E., Röschmann, N., Scharmberg, C., Sierks, H., Rusznyak, P., McKenna-Lawlor, S., Elenndt, I., Sequeiros, J., Meziat, D., Sanchez, S., Medina, J., Del Peral, L., Witte, M., Marsden, R., Henrion, J., Dec. 1995. COSTEP - Comprehensive Suprathermal and Energetic Particle Analyser. *Solar Physics* 162, 483–504.
- Munro, R. H., Jackson, B. V., May 1977. Physical properties of a polar coronal hole from 2 to 5 solar radii. *Astrophys. J.* 213, 874–886.
- NASA – HelioWeb, 2008. Heliocentric Trajectories for Selected Spacecraft, Planets and Comets. <http://cohoweb.gsfc.nasa.gov/helios/heli.html> (visited regularly between March 2006 and October 2008).
- National Geographic Data Center, 2008. Solar Data Services - International Sunspot Number. <http://www.ngdc.noaa.gov/stp/SOLAR/ftpsunspotnumber.html> (visited on November 7, 2008).
- Ness, N. F., Burlaga, L. F., Aug. 2001. Spacecraft studies of the interplanetary magnetic field. *J. Geophys. Res.* 106, 15803–15818.
- Neugebauer, M., Snyder, C. W., Dec. 1962. Solar Plasma Experiment. *Science* 138, 1095–1097.
- Neugebauer, M., Snyder, C. W., 1966. Mariner-2 Measurements of the Solar Wind. In: Mackin, Jr., R. J., Neugebauer, M. (Eds.), *The Solar Wind*. p. 3ff.
- Parker, E. N., Nov. 1958. Dynamics of the Interplanetary Gas and Magnetic Fields. *Astrophys. J.* 128, 664–676.
- Parker, E. N., 1965. The passage of energetic charged particles through interplanetary space. *Planet. Space Sci.* 13, 9–49.
- Potgieter, M. S., Nov. 1996. Heliospheric modulation of galactic electrons: Consequences of new calculations for the mean free path of electrons between 1 MeV and  $\sim 10$  GeV. *J. Geophys. Res.* 101, 24411–24422.
- Potgieter, M. S., Jan. 1998. The Modulation of Galactic Cosmic Rays in the Heliosphere: Theory and Models. *Space Science Reviews* 83, 147–158.
- Potgieter, M. S., Burger, R. A., Ferreira, S. E. S., 2001. Modulation of Cosmic Rays in the Heliosphere From Solar Minimum to Maximum: a Theoretical Perspective. *Space Science Reviews* 97, 295–307.
- Potgieter, M. S., Ferreira, S. E. S., Jul. 2002. Effects of the solar wind termination shock on the modulation of Jovian and galactic electrons in the heliosphere. *Journal of Geophysical Research (Space Physics)* 107 (A7), 1089.

- Potgieter, M. S., Haasbroek, L. J., 1993. The simulation of base-line cosmic ray modulation for the Ulysses trajectory. In: International Cosmic Ray Conference. Vol. 3 of International Cosmic Ray Conference. pp. 457–460.
- Potgieter, M. S., Moraal, H., Jul. 1985. A drift model for the modulation of galactic cosmic rays. *Astrophys. J.* 294, 425–440.
- Press, W. H., Flannery, B. P., Teukolsky, S. A., Vetterling, W. T., 9 1992. *Numerical Recipes in FORTRAN 77: The Art of Scientific Computing*, 2nd Edition. Cambridge University Press.
- Prölss, G. W., 9 2004. *Physik des erdnahen Weltraums. Eine Einführung*, 2nd Edition. Springer Berlin.
- Pyle, K. R., Simpson, J. A., Jul. 1977. The Jovian relativistic electron distribution in interplanetary space from 1 to 11 AU - Evidence for a continuously emitting 'point' source. *Astrophys. J. Lett.* 215, L89–L93.
- Roberts, D. A., Giacalone, J., Jokipii, J. R., Goldstein, M. L., Zepp, T. D., Aug. 2007. Spectra of polar heliospheric fields and implications for field structure. *Journal of Geophysical Research (Space Physics)* 112, A08103.
- Roelof, E. C., Simnett, G. M., Decker, R. B., Lanzerotti, L. J., MacLennan, C. G., Armstrong, T. P., Gold, R. E., Jun. 1997. Reappearance of recurrent low-energy particle events at Ulysses/HI-SCALE in the northern heliosphere. *J. Geophys. Res.* 102, 11251–11262.
- Scherer, K., Fichtner, H., Borrman, T., Beer, J., Desorgher, L., Flükiger, E., Fahr, H.-J., Ferreira, S. E. S., Langner, U. W., Potgieter, M. S., Heber, B., Masarik, J., Shaviv, N., Veizer, J., Jan. 2007. *Interstellar-Terrestrial Relations: Variable Cosmic Environments, The Dynamic Heliosphere, and Their Imprints on Terrestrial Archives and Climate*. *Space Science Reviews*, 327–465.
- Scherer, K., Fichtner, H., Marsch, E., 2000. *The Outer Heliosphere: Beyond the Planets*. Copernicus Gesellsch.
- Schlickeiser, R., 1989. Cosmic-ray transport and acceleration. I. Derivation of the kinetic equation and application to cosmic rays in static cold media. *Astrophys. J.* 336, 243–263.
- Schlickeiser, R., 2002. *Cosmic Ray Astrophysics*, 1st Edition. Springer.
- Schwabe, M., 1851. *Sonnen-Beobachtungen im Jahre 1850, von Herrn Hofrath Schwabe*. *Astronomische Nachrichten* 32, 109–112.

- Schwadron, N. A., Jul. 2002. An explanation for strongly underwound magnetic field in co-rotating rarefaction regions and its relationship to footpoint motion on the sun. *Geophys. Res. Lett.* 29 (14), 1663.
- Schwadron, N. A., McComas, D. J., Jun. 2003. Heliospheric “FALTS”: Favored Acceleration Locations at the Termination Shock. *Geophys. Res. Lett.* 30 (11), 1587.
- Shalchi, A., 2009. *Nonlinear Cosmic Ray Diffusion Theories*, 1st Edition. Springer.
- Shalchi, A., Bieber, J. W., Matthaeus, W. H., 2004. Analytic forms of the perpendicular diffusion coefficient in magnetostatic turbulence. *Astrophys. J.* 604 (2), 675–686.
- Simpson, J. A., Anglin, J. D., Balogh, A., Bercovitch, M., Bouman, J. M., Budzinski, E. E., Burrows, J. R., Carvell, R., Connell, J. J., Ducros, R., Ferrando, P., Firth, J., Garcia-Munoz, M., Henrion, J., Hynds, R. J., Iwers, B., Jacquet, R., Kunow, H., Lentz, G., Marsden, R. G., Mckibben, R. B., Müller-Mellin, R., Page, D. E., Perkins, M., Raviart, A., Sanderson, T. R., Sierks, H., Treguer, L., Tuzzolino, A. J., Wenzel, K. P., Wibberenz, G., Jan. 1992. The ULYSSES Cosmic Ray and Solar Particle Investigation. *Astron. and Astrophys. Suppl.* 92, 365–399.
- Simpson, J. A., Anglin, J. D., Bothmer, V., Connell, J. J., Ferrando, P., Heber, B., Kunow, H., Lopate, C., Marsden, R. G., McKibben, R. B., Müller-Mellin, R., Paizis, C., Rastoin, C., Raviart, A., Sanderson, T. R., Sierks, H., Trattner, K. J., Wenzel, K.-P., Wibberenz, G., Zhang, M., May 1995. Cosmic Ray and Solar Particle Investigations Over the South Polar Regions of the Sun. *Science* 268, 1019–1023.
- Simpson, J. A., Zhang, M., Bame, S., Jul. 1996. A Solar Polar North-South Asymmetry for Cosmic-Ray Propagation in the Heliosphere: The ULYSSES Pole-to-Pole Rapid Transit. *Astrophys. J. Lett.* 465, L69–L72.
- Smith, C. W., Bieber, J. W., March 1991. Solar cycle variation of the interplanetary magnetic field spiral. *Astrophys. J.* 370 (1), 435–441.
- Sternal, O., Burger, R. A., Heber, B., Fichtner, H., Dunzlaff, P., 2008. The Diffusion Tensor of Energetic Particles in Different Heliospheric Magnetic Field Configurations. In: *Proceedings of the 30th International Cosmic Ray Conference*. Vol. 1. pp. 451–454.
- Strong, A. W., Bennett, K., Bloemen, H., Diehl, R., Hermsen, W., Morris, D., Schoenfelder, V., Stacy, J. G., de Vries, C., Varendorff, M., Winkler, C., Youssefi, G., Dec. 1994. Diffuse continuum gamma rays from the Galaxy observed by COMPTEL. *Astron. Astrophys.* 292, 82–91.
- Strong, A. W., Moskalenko, I. V., Reimer, O., Jul. 2000. Diffuse Continuum Gamma Rays from the Galaxy. *Astrophys. J.* 537, 763–784.

- Suess, S. T., Poletto, G., Wang, A.-H., Wu, S. T., Cuseri, I., Jun. 1998. The Geometric Spreading of Coronal Plumes and Coronal Holes. *Solar Physics* 180, 231–246.
- Teegarden, B. J., McDonald, F. B., Trainor, J. H., Webber, W. R., Roelof, E. C., 1974. Interplanetary MeV electrons of Jovian origin. *J. Geophys. Res.* 79, 3615–3622.
- Teufel, A., Schlickeiser, R., 2002. Analytic calculation of the parallel mean free path of heliospheric cosmic rays. I. Dynamical magnetic slab turbulence and random sweeping slab turbulence. *Astron. Astrophys.* 393, 703–715.
- Teufel, A., Schlickeiser, R., 2003. Analytic calculation of the parallel mean free path of heliospheric cosmic rays. II. Dynamical magnetic slab turbulence and random sweeping slab turbulence with finite wave power at small wavenumbers. *Astron. Astrophys.* 397, 15–25.
- Trace Web Site, 2008. TRACE: Transition Region and Coronal Explorer. <http://trace.lmsal.com> (visited on September 17, 2008).
- Van Helden, A., 1995. The Galileo Project. <http://galileo.rice.edu> (visited on September 16, 2008).
- Waldmeier, M., Apr. 1981. Cyclic variations of the polar coronal hole. *Solar Physics* 70, 251–258.
- Webb, D. F., Davis, J. M., McIntosh, P. S., May 1984. Observations of the reappearance of polar coronal holes and the reversal of the polar magnetic field. *Solar Physics* 92, 109–132.
- Webb, G. M., Gleeson, L. J., Feb. 1979. On the equation of transport for cosmic-ray particles in the interplanetary region. *Astrophys. and Space Sci.* 60, 335–351.
- Webber, W. R., Higbie, P. R., Nov. 2008. Limits on the interstellar cosmic ray electron spectrum below  $\sim 1\text{--}2$  GeV derived from the galactic polar radio spectrum and constrained by new Voyager 1 measurements. *Journal of Geophysical Research (Space Physics)* 113, A11106.
- Wenzel, K. P., Marsden, R. G., Page, D. E., Smith, E. J., Jan. 1992. The ULYSSES Mission. *Astron. and Astrophys. Suppl.* 92, 207–219.
- Zank, G. P., 1999. Interaction of the solar wind with the local interstellar medium: a theoretical perspective. *Space Science Reviews* 89, 413–688.
- Zank, G. P., Gang, L., Florinski, V., Matthaeus, W. H., Webb, G. M., le Roux, J. A., 2004. Perpendicular diffusion coefficient for charged particles of arbitrary energy. *J. Geophys. Res.* 109, A04107.

Zurbuchen, T. H., Schwadron, N. A., Fisk, L. A., Oct. 1997. Direct observational evidence for a heliospheric magnetic field with large excursions in latitude. *J. Geophys. Res.* 102, 24175–24182.



# Some final Statements

I would like to thank all those people, who supported me in the process of my graduate studies and during the writing of this dissertation. My special thanks go to...

- ...Prof. Dr. Bernd Heber for the opportunity to work on an interesting problem in heliophysics, the possibility to attend interesting conferences and workshops, as well as support during my studies which were not always straight forward.
- ...Priv.-Doz. Dr. habil. Horst Fichtner for help and support via different ways of modern communication and during several visits to the Ruhr-Universität Bochum.
- ...Prof. Adri Burger, M.Sc. Eugene Engelbrecht, Prof. Stefan Ferreira and Prof. Marius Potgieter for fruitful discussions and answers to many questions.
- ...Dr. Klaus Scherer for discussions and support in debugging complicated formulae when I became blind.
- ...Dr. Andreas Kopp for critical comments regarding this work.
- ...Dipl.-Phys. Phillip Dunzlaff and Dr. Raul Gomez-Herrero for the supply of spacecraft data.
- ...the heliophysics group at the Christian-Albrechts-Universität zu Kiel for the nice atmosphere during my studies.

Oliver Sternal  
Institut für Experimentelle und Angewandte Physik  
– Heliosphärische Astroteilchenphysik –  
Christian-Albrechts-Universität zu Kiel



# Lebenslauf

## Persönliche Daten

Oliver Sternal

E-Mail: sternal@physik.uni-kiel.de  
Geboren am: 27. Oktober 1979 in Castrop-Rauxel  
Nationalität: Deutsch

## Berufserfahrung

seit 03/2006 Wissenschaftlicher Mitarbeiter in der Abteilung Extraterrestrische Physik am Institut für Experimentelle und Angewandte Physik der Christian-Albrechts-Universität zu Kiel  
01/2006 – 02/2006 Wissenschaftlicher Mitarbeiter am Lehrstuhl für theoretische Weltraum- und Astrophysik an der Ruhr-Universität Bochum  
10/2001 – 12/2005 Studentische Hilfskraft

## Promotion

seit 03/2006 Promotion in der Abteilung Extraterrestrische Physik am Institut für Experimentelle und Angewandte Physik der Christian-Albrechts-Universität zu Kiel  
Thema der Promotion: *Transport of Galactic Cosmic Rays in Different Heliospheric Magnetic Field Configurations*

## Studium

10/1999 – 12/2005 Studium der Physik an der Ruhr-Universität Bochum  
Erlangung des Vordiploms am 10. Oktober 2001  
Abschluss mit dem Diplom am 20. Dezember 2005 mit der Note sehr gut  
Thema der Diplomarbeit: *Berechnung der Flüsse energetischer Neutralatome aus der heliosphärischen Grenzschicht*



# Eidesstattliche Erklärung

Hiermit erkläre ich an Eides statt, dass ich die vorliegende Arbeit abgesehen vom Rat meiner akademischen Lehrer ohne fremde Hilfe und lediglich unter Verwendung der angegebenen Literatur angefertigt habe. Diese Arbeit ist unter Einhaltung der Regeln guter wissenschaftlicher Praxis entstanden und nach Inhalt und Form meine eigene Arbeit.

Ich versichere, dass diese Arbeit weder ganz noch teilweise an anderer Stelle zur Prüfung vorlag. Frühere Promotionsversuche wurden von mir nicht unternommen.

Teile dieser Arbeit wurden im Rahmen von verschiedenen Konferenzen vorgestellt bzw. sind als Beiträge für zukünftige Tagungen angemeldet:

- 07/2007 *The Diffusion Tensor of Energetic Particles in Different Heliospheric Magnetic Field Configurations*, Poster und Paper bei der International Cosmic Ray Conference in Mérida, Mexiko
- 07/2009 *Time-dependent Propagation of  $\gamma$  MeV Electrons in a Fisk-Parker Hybrid HMF*, Poster und Paper bei der International Cosmic Ray Conference in Łódź, Polen
- 07/2010 *26-Day Variations of  $\gamma$  MeV Electrons at high Latitudes and their Implications on the Heliospheric Magnetic Field*, Vortrag und Paper bei der Tagung des Committee on Space Research in Bremen

Kiel, den .....

.....

(Oliver Sternal)